DEVELOPMENT AND APPLICATION OF CEST MRI CONTRAST AGENTS THAT EVALUATE TUMOR ACIDOSIS AND ENZYME ACTIVITY

by

Chathuri Jeewanthi Kombala Nanayakkara Thambiliyagodage

A Dissertation Submitted to the Faculty of the

DEPARTMENT OF CHEMISTRY AND BIOCHEMISTRY

In Partial Fulfillment of the Requirements

For the Degree of

DOCTOR OF PHILOSOPHY
WITH A MAJOR IN CHEMISTRY

In the Graduate College

THE UNIVERSITY OF ARIZONA

2020

THE UNIVERSITY OF ARIZONA
GRADUATE COLLEGE

As members of the Dissertation Committee, we certify that we have read the dissertation prepared by: Chathuri Jeewanthi Kombala Nanayakkara Thambiliyagodage, titled: Development and Application of CEST MRI Contrast Agents that Evaluate Tumor Acidosis and Enzyme Activity and recommend that it be accepted as fulfilling the dissertation requirement for the Degree of Doctor of Philosophy.

Eugene A. Mash — Date: 4/9/20

Mark D. Pagel — Date: 4/9/2020

Pascale G. Charest — Date: April 20, 2020

Philip H. Kuo — Date: 4/20/2020

Final approval and acceptance of this dissertation is contingent upon the candidate's submission of the final copies of the dissertation to the Graduate College.

I hereby certify that I have read this dissertation prepared under my direction and recommend that it be accepted as fulfilling the dissertation requirement.

Eugene A. Mash — Date: 4/15/20
Dissertation Committee Chair
Department of Chemistry and Biochemistry

ACKNOWLEDGMENTS

My doctoral journey would not have been possible to accomplish without the support and guidance that I received from a wonderful group of people.

I want to thank my Ph.D. advisor, Dr. Marty Pagel, for his support and encouragement during these past five years. Without his guidance and constant feedback, this Ph.D. would not have been achievable. It was an honor to work under your mentorship throughout my doctoral journey. Thank you for providing such an exceptional environment to pursue my doctoral research. I am incredibly grateful to my committee members, Dr. Mash, Dr. Charest, and Dr. Kuo, for the constant assistance that they provided at all levels of my doctoral career.

My prior training and research experiences have helped me to begin my doctoral research more independently. I want to thank my previous advisors, Dr. Dustin E. Gross at Sam Houston State University and Dr. M.P. Deeyamulla at the University of Kelaniya for their excellent mentorship.

I am thankful for the Department of Chemistry and Biochemistry at the University of Arizona and the Department of Cancer Systems Imaging at the University of Texas MD Anderson Cancer Center for providing me such an exceptional environment to conduct my doctoral research. I greatly value the education and research experience that I obtained from these institutions.

I would also like to thank my colleagues in the CAMEL group. In particular, I would like to thank Dr. Aikaterini Kotrotsou and Dr. Shu Zhang for data analysis, and William Schuler and Jorge de la Cerda for their help with cell culture and *in vivo* experiments. Also, thank you, Alyssa Pollard, for being such a helpful lab mate.

My Ph.D. wouldn't be achievable without the support of my family. I want to say a heartfelt thank you to my mom, dad, and sister for always believing in me and encouraging me to follow my dreams. Finally, to my husband, Sanjaya, for his fantastic support and encouragement in academic and personal matters. Without him, I would not have had the courage to commence on this journey in the first place. And my loving son, Sehas, for relieving my stress with his beautiful smile during the last year of my Ph.D.

DEDICATION

I dedicate this thesis to

my parents, Hemasiri Kombala and Padmini Sooriyarachchi

my sister, Darshani Kombala

my husband, Sanjaya Lokugama

and my beloved son Sehas Lokugama

for their unconditional support and love.

TABLE OF CONTENTS

LIST OF FIGURES

LIST OF SCHEMES

LIST OF TABLES

LIST OF ABBREVIATIONS

CEST	Chemical Exchange Saturation Transfer
DiaCEST	Diamagnetic CEST
DMF	Dimethylformamide
DOTAM	1,4,7,10-tetraazacyclododecane-1,4,7,10-tetraacetic acid amide
DP	Degree of polymerization

DTT	Dithiothreitol
EDC.HCl	1-(3-dimethylaminopropyl)-3-ethylcarbodiimide hydrochloride
EPR	Enhanced permeability and retention
ESI	Electro Spray Ionization
FA	Flip angle
FISP	Fast Imaging with Steady State Precession
FOV	Field of View
GPC	Gel permeation chromatography
HRMS	High-resolution mass spectrometry
HW-QUESP	Hanes Woolf QUESP
I.V	Intravenous
k_{cat}	Catalytic turn over number
k_{ex}	Chemical exchange rate
K_M	Michaelis–Menten constant
LB-conc	Lineweaver-Burk concentration dependent analysis method
LC-MS	Liquid Chromatography-Mass Spectrometry
LRMS	Low-resolution mass spectrometry
MAA	Methacrylic acid
MALDI-TOF	Matrix-Assisted Laser Desorption/Ionization-Time Of Flight
NMM	N-methylmorpholine
NMR	Nuclear Magnetic Resonance
NSF	Nephrogenic Systemic Fibrosis
PAA	Polyallylamine

PAMAM	Poly(amidoamine)
ParaCEST	Paramagnetic CEST
PBS	Phosphate Buffered Saline
PDA detector	Photodiode array detector
PEG	Poly ethylene glycol
PEI	Polyethylenimine
pHe	Extracellular pH
PLE	Poly L glutamate
PLL,PLK	Poly L lysine
PLR	Poly L arginine
PLT	Poly L threonine
PSMA	Prostate specific membrane antigen
PTE	Proton transfer enhancement
QUESP	QUantifying Exchange rates using Saturation Power
QUEST	QUantifying Exchange rates using Saturation Time
RL-QUEST	Reciprocal Linear QUEST
ROI	Region of interest
SEM	Scanning electron microscopy
SL	Slice thickness
SPD	Starburst PAMAM dendrimer
TE	Echo time
TEM	Transmission electron microscopy
THF	Tetrahydrofuran

TQ detector	Tandem Quadrupole mass detector
TR	Repetition time
UPLC	Ultra Performance Liquid Chromatography
UV	Ultraviolet
Z-spectrum	Chemical Exchange Saturation Transfer Spectrum

ABSTRACT

The extracellular tumor microenvironments of many solid tumors have high acidosis and high protease activity. The detection of tumor acidosis and protease activity can potentially impact the cancer diagnosis. Noninvasive imaging methods have previously been developed that measure extracellular pH or can detect enzyme activity using Chemical Exchange Saturation Transfer Magnetic Resonance Imaging (CEST MRI). CEST MRI is an inherently insensitive MRI modality which requires a high concentration of small molecule agent to be delivered to the tumor. Therefore, nanosized molecules have received increased attention to be used in CEST imaging to improve the sensitivity.

Herein, we developed a nanoscale CEST agent that can measure pH using acidoCEST MRI, which may decrease the requirement for high delivery concentrations of agent. We also developed a monomer agent for comparison to the polymer. After optimizing CEST experimental conditions, we determined that the polymer agent could be used during acidoCEST MRI studies at 125-fold and 488-fold lower concentration than the monomer agent and iopamidol, respectively. *In vivo* acidoCEST MRI studies using the three agents were performed to study a xenograft MDA-MB-231 model of mammary carcinoma. The tumor pHe measurements were 6.33 ± 0.12, 6.70 ± 0.15, and 6.85 ± 0.15 units with iopamidol, the monomer agent and polymer agent, respectively. The higher pHe measurements with the new agents was attributed to the concentration dependence of these agents. This study demonstrated that nanoscale agents have merit for CEST MRI studies, but consideration should be given to the dependence of CEST contrast on the concentration of these agents.

We also investigated the development and application of a single hybrid CEST agent that can simultaneously measure pH and evaluate protease activity using a combination of dual-power acidoCEST MRI and catalyCEST MRI. Simultaneously assessing both characteristics may improve diagnostic evaluations of aggressive tumors and the effects of anti-cancer treatments. Our agent showed CEST signals at 9.2 ppm from a salicylic acid moiety and at 5.0 ppm from an aryl amide. The CEST signal at 9.2 ppm could be measured after selective saturation was applied at 1 and 4 μT, and these measurements could be used with a ratiometric analysis to determine pH. The CEST signal at 5.0 ppm from the aryl amide disappeared after the agent was treated with cathepsin-B, while the CEST signal at 9.2 ppm remained, indicating that the agent could detect protease activity through amide bond clevage. Michaelis-Menton kinetics studies with catalyCEST MRI demonstrated that the binding affinity (as shown with the Michaelis constant K_M), the catalytic turnover rate (k_{cat}), and catalytic efficiency (k_{cat}/k_M), were each higher for cathepsin B at lower pH. The k_{cat} rates measured with catalyCEST MRI were lower than the comparable rates measured with LC-MS, which reflected a limitation of inherently noisy and relatively insensitive CEST MRI analyses. Although this level of precision limited catalyCEST MRI to semi-quantitative evaluations, these semi-quantitative assessments of high and low protease activity still had value by demonstrating that high acidosis and high protease activity can be used as synergistic, multi-parametric biomarkers.

CHAPTER 1

RECENT ADVANCES IN NANOSIZED POLYMERIC CEST MRI CONTRAST AGENTS

CEST is an emerging MRI contrast mechanism that is well suited for molecular imaging [1]. Noninvasive measurements of the extracellular pH of the tumor microenvironment can enhance diagnoses and treatment decisions [2]. However, one of the current limitations of exogenous CEST agents is their relatively low sensitivity, typically requiring 1–10 mM of agent for detection [1]. CEST agents can be made more sensitive by simply increasing the number of exchangeable groups on the agent. The nanoscale agents may deliver a greater payload of exchangeable protons to tumor tissue. Thus, it is important to explore the biological rationale and the synthetic strategies behind designing the polymeric contrast agents.

1.1 BIOLOGICAL RATIONALE FOR THE DESIGN OF TUMOR-TARGETED POLYMERIC CONTRAST AGENTS

Small molecule contrast agents exhibit poor pharmacokinetic properties and eliminate from the body very quickly [3]. There are numerous polymeric contrast agents that have been reported to date [4,5]. Due to their high molecular weight, polymeric agents can have favorable pharmacokinetic properties such as prolonged retention in the body. Thus, problems associated with small molecule agents could be eliminated by conjugating small molecules to a polymeric carrier or making a polymeric agent. It is now well known that long-circulating polymeric agents accumulate passively in solid cancerous tissue by the enhanced permeability and retention (EPR) effect [6].

1.1.1 EPR EFFECT

Tumor tissues must have an increased level of vasculature for their rapid growth, which depends on an elevated blood supply for nutrition and oxygen supply. However, these blood

vessels are defective in their architecture and create an enhanced vascular permeability, which allows particles to enter the tumor interstitial space. This phenomenon is called the EPR effect that facilitates the transport of macromolecules into tumor tissues [6]. When macromolecules enter into the tumor interstitium [7], they will either be internalized into cells or remain present in the extracellular microenvironment. The contrast agents can be designed to act on either the extracellular matrix (tumor microenvironment) or inside the tumor cell.

1.1.2 INTRACELLULAR DELIVERY

It is well known that endocytosis is the major route of macromolecular uptake, whether the macromolecules are soluble cargo or membrane proteins [8]. These agents are designed to accumulate imaging probes inside the cell [9]. There are two types of intracellular delivery mechanisms, known as lysosomotropic and endosomotropic delivery. During the lysosomotropic delivery, macromolecular agents are internalized by endocytosis, followed by intracellular trafficking via endosomal compartments to lysosomes. Then, the imaging agents diffuse from the lysosome compartment as a result of pH-dependent discharge from the lysozyme [10,11].

Endosomotropic delivery starts with the internalization of a macromolecular agent by endocytosis. The lower pH in the endosomal compartment causes the polymer to change its conformation. The change in polymer conformation causes an increase in endosomal membrane permeability, and contrast agents escape into the cytosol. There is minimal lysosomal trafficking associated with this mechanism [11,12]. However, slow endocytosis limits the usage of intracellular delivery of contrast agents; thus, there is a focus on designing contrast agents for extracellular delivery.

1.1.3 EXTRACELLULAR DELIVERY

Even though the tumor microenvironment is not as acidic as endosomal or lysosomal compartments (pH ~5), the pH of the extracellular environment ranges from 6.2 to 6.8 [13]. Also, there are extracellular enzymes present in the tumor microenvironment [2]. The responsive or non-responsive contrast agents could be designed for extracellular delivery by targeting tumor extracellular biomarkers. If macromolecular agents are designed to act in the extracellular space, then the agents need to be designed with minimum binding to tumor cells to lower the internalization. Considering the concept of a pro-drug, macromolecular contrast agents could be constructed to release the imaging agent in the tumor interstitium as a response to an extracellular tumor biomarker. The released agent could accumulate in the tumor microenvironment at high concentrations [14]. Responsive macromolecular agents have been reported as a response to the acidic tumor microenvironment [10,11]. A reported pH-responsive micelle protonates in the tumor acidic environment, resulting in the disruption of the micellar structure. Then, the MRI signal intensity increases as the micelles are broken. Due to the protonation of the molecule, the accumulation in the tumor microenvironment is facilitated by ionic interactions between positively charged agents and negatively charged cellular membranes.

1.2 INCORPORATION OF CONTRAST AGENTS INTO THE POLYMER

1.2.1 INCORPORATION INTO THE MAIN CHAIN

There are several methods that incorporate a contrast agent into a polymer. The synthesis of macromolecular contrast agents depends on the way that the imaging probe is attached in the polymer chain. The polymeric agent can be designed by incorporating the probe into the polymer main chain (Figure 1.1a). In this approach, the probe participates in the polymerization reaction, and must, therefore, be bifunctional. For instance, biphenols or diamines can undergo condensation

reactions with dicarboxylic acid groups resulting in condensation polymers. The polymers with probes incorporated into the main chain have been reported for fluorescence imaging [15,16]. However, when the probe is directly attached to the main chain, the probe suffers steric hindrance by other surrounding groups, which can affect the function of the imaging probe. Therefore, imaging probes can be connected to the polymer backbone as a pendant group.

1.2.2 ATTACHED AS A PENDENT GROUP

Macromolecular contrast agents have been synthesized by attaching the probe as a pendent group (Figure 1.1b), which gives space between the polymer backbone and the probe [17]. This approach can be achieved either by synthesizing the monomer with a pendant imaging probe or by conjugating the probe to the pendant functional group in the polymer. If the probe is conjugated to the pendant functional group, it is difficult to achieve 100% loading efficiency [18]. Therefore, the final agent will have unreacted functional groups without a conjugated probe. The efficiency of this agent depends on how many probe molecules are attached to the polymer backbone. Unconjugated functional groups in the polymer backbone may interfere with the final agent's function. If the monomer is synthesized with the pendant groups, no additional functional group will be present in the final agent. We can also control the size of the final agent by optimizing the polymerization conditions.

1.2.3 ATTACHED VIA A SPACER

An imaging probe can be attached to the polymer by adding an extra spacer between the backbone and the probe, which gives lower steric hindrance from the backbone. Most of the bulky probes used in polymers have been attached to the backbone via a spacer [19,20]. Similarly, the spacer could either be added to a polymeric backbone followed by conjugation of the monomer

agent to the spacer, or a monomer with a spacer can be first synthesized, followed by polymerization. Biologically applicable polymer backbones such as dextran [21,22], dendrimer [23], and hyaluronic acid [24-26] are usually selected with a spacer or without a spacer. These polymeric backbones consist of functional groups that are labile for conjugation.

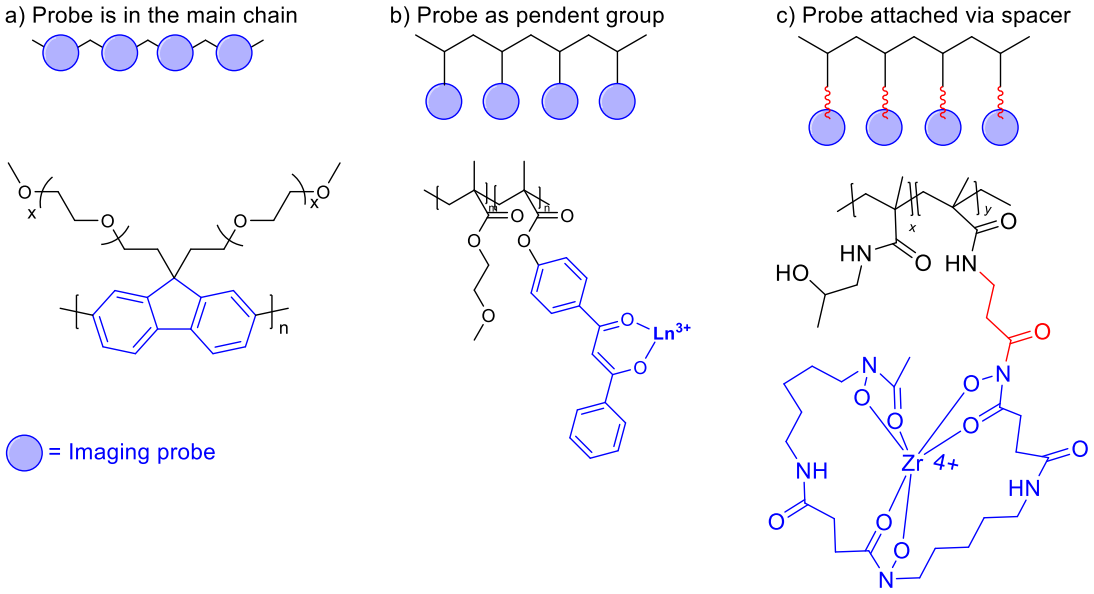

Figure 1.1. Different polymeric imaging agent synthesis methods and examples. The schematics and examples show the polymer backbone in black, the agent in blue, and the spacer in red.

Polymeric contrast agents with a spacer have been synthesized either as a homo-polymer [20] or co-polymer [27]. Co-polymers show additional advantages due to the possibility of introducing different types of functional groups. Thus, properties of the agent can be altered by introducing solubilizing groups, groups with hydrophilic and hydrophobic characters, and/or anchoring groups.

Conjugation and polymerization reactions need to be performed with mild conditions because the imaging probe may be sensitive to harsh reaction conditions. Also, conjugation reactions that are not performed under mild conditions may result in unnecessary side reactions

and errors that are retained in the final polymeric agents, resulting in changes in physicochemical parameters of the polymer.

Some functional groups such as acid and alcohol groups are needed to generate imaging signals or image contrast [18]. These functional groups for the purpose of imaging may interfere with polymerization and conjugation reactions, resulting in very low yield of the desired agent. To overcome this issue, functional groups of the imaging probe need to be protected before the conjugation/polymerization reaction followed by the deprotection of the groups after the reaction. Then we can obtain the polymeric agent with high purity and high yield.

1.3 CEST MRI CONTRAST AGENTS

MRI has become a crucial diagnostic tool in clinical medicine [28]. Recent developments with MRI contrast agents have provided novel capabilities for biomarker detection via molecular imaging [2]. A variety of MRI contrast agents have been advanced to improve the molecular imaging of many disease types, including cancer. The extracellular tumor environment is typically different than that of normal healthy tissues. The enzyme activity and extracellular acidity are well-established biomarkers for tumor detection by MRI [2,29,30]. Due to inherent limitations in detection sensitivity (~10 μM to ~10 mM), MRI requires a higher concentration of contrast agent, relative to most other imaging modalities.

1.3.1 THE CEST MECHANISM

Chemical exchange saturation transfer (CEST) is an MRI contrast mechanism that is well suited for molecular imaging (Figure 1.2) [2]. In this imaging modality, endogenous or exogenous compounds having exchangeable protons are selectively saturated with a particular radio frequency (RF). The applied RF matches with the resonance frequency of solute protons and

causes the saturation of solute protons. When the solute protons exchange with water protons, the saturation is transferred to the bulk water. Consequently, the detected water signal decreases. In the presence of a low concentration of the agent (mM range for a monomeric CEST agent), a single transfer of saturation would not be enough to exhibit any noticeable effect on water signal. Since the water pool is relatively greater than the saturated solute proton pool, all of the saturated solute protons are replaced by water protons through chemical exchange, which is then again saturated. With the solute protons having a sufficiently fast exchange rate, the saturation time becomes adequately short. Prolonged irradiation causes considerable enhancement of the saturation effect and ultimately becomes visual on the water signal. This allows the low concentration of solutes to be imaged indirectly via water signal [31,32].

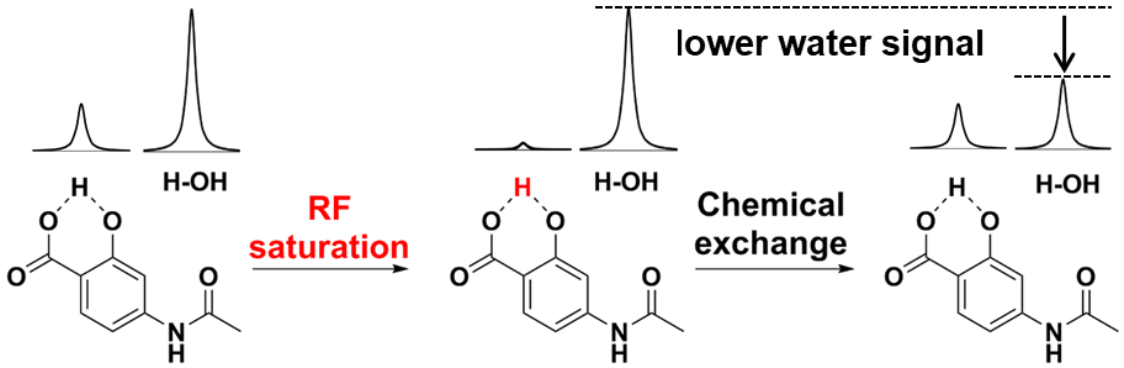

Figure 1.2. CEST MRI process. 1: Radio frequency saturation causes a proton to lose its coherent magnetic resonance signal. 2: A proton undergoes chemical exchange from the agent to water. 3: The water signal is acquired. A lower water signal indicates that the agent is present [31].

1.3.2 ADVANTAGES AND DISADVANTAGES OF CEST MRI

CEST agents can be sub-divided into two main classes: diamagnetic CEST (diaCEST) and paramagnetic CEST (paraCEST) depending on the magnetism of the agent [33]. Most of the paraCEST agents have lanthanide ions that can cause Nephrogenic Systemic Fibrosis (NSF) [34].

NSF is a primarily cutaneous pathology that causes insidious skin rashes and thickening, and can also cause joint stiffening. Circulating fibrocytes are activated by lanthanide ions, which then cause the skin to deposit mucin, collagen, and elastin in a parody of normal wound healing [35]. Clinical involvement can include other tissues such as lung, skeletal muscle, heart, diaphragm, and esophagus, which may lead to death [34]. DiaCEST agents do not contain toxic f-block metals and have a greater potential for use with *in vivo* MRI [31].

CEST MRI has several advantages over other imaging modalities [32]. CEST can generate two signals at the same time using chemically or conformationally inequivalent protons [29]. Most of the responsive CEST agents mainly target the extracellular tumor pH and enzyme activity [2].

However, CEST MRI possesses some limitations as well. CEST is an inherently insensitive technique, typically requiring 1–10 mM of agent for detection [32]. Thus, the use of a high concentration of exogenous CEST agents for imaging may cause toxic effects. CEST agents can be made more sensitive by merely increasing the number of exchangeable groups on the agent. Therefore, CEST MRI for the detection of targets requires the use of a single agent with a higher number of exchangeable groups. An efficient way to increase the exchangeable protons in a single molecule is to synthesize a polymeric agent.

1.4 NANOSIZED CEST AGENTS

Macromolecular contrast agents exhibit several different benefits over monomeric agents, including enhanced contrast sensitivity per molecule, prolonged blood circulation times, and availability of different functional groups to attach the imaging probe [36]. These materials can be obtained from various sources, such as biopolymers [26], liposomes [37], synthetic polymers [20], and dendrimers [23]. Nanosized macromolecules have shown suitability for different imaging

applications. Considering the advantages of macromolecular agents, nanosized CEST contrast agents may exhibit a significant impact on molecular imaging. There are several different types of macromolecules that have been investigated to enhance the CEST contrast.

1.4.1 LINEAR POLYMERS

1.4.1.1 PARACEST LINEAR AGENTS

To date, there are paraCEST and diaCEST linear polymers that have been reported. Sherry and co-workers reported a Eu^{3+} based paraCEST linear polymer by connecting the imaging probe to the polymer backbone as a pendent group [20,38]. The paraCEST imaging probes are usually bulky compounds. They used a spacer between the imaging probe and the polymer backbone to avoid hindrance that can affect the function of the imaging probe. They optimized the size of the polymer by using different initiator concentrations. The observed a 55 ppm CEST peak at 11.75 T magnetic field strength, 14.1 μT saturation power, and 4 s saturation time for the monomer, which does not alter with polymer formation. Table 1.1, entry one, shows the difference between expected sensitivity and the observed sensitivity of this polymer agent. They reported that the contrast sensitivity increases approximately by a factor of 10.5, which is lower than the expected sensitivity factor of 17.4 based on the average number of monomer units per polymer. However, they were able to achieve increased sensitivity by 60% from the predicted sensitivity.

Sherry and co-workers extended their previous paraCEST study by synthesizing heteropolymers consisting of variable co-polymer side chains to optimize the sensitivity [39]. They introduced non-CEST acrylamide units into the polymer backbone as co-polymer side chains, which gives more space between imaging probe units and aids in changing the physical properties as well as CEST properties of the polymer. It has been shown that the degree of polymerization increases by introducing co-polymer units between contrast agent units and thus increases the

CEST contrast. Having a co-polymer unit between functional probe units can lower the steric hindrance among the imaging probes in the polymer. Therefore, putting a spacer between pendant groups on the polymer backbone is not sufficient to avoid the steric interactions between bulky paraCEST agents. Table 1.1, entry two, shows the sensitivity enhancement of the new co-polymer based agents. Some of the reported polymers (Eu-DMMA 3.0 and 3.1) showed enhanced CEST sensitivity by a factor of 20. As a percentage, some of the polymeric agents reached the enhanced CEST sensitivity by 80% from the expected sensitivity (Eu-DMMA 1.1 and 2.0).

1.4.1.2 DIACEST LINEAR AGENTS

Several diaCEST linear polymers have been reported to date. Most of them are peptide-based agents. Zijl and co-workers reported cationic polymer-based gene delivery systems as CEST agents [40]. They investigated CEST properties of poly L lysine (PLL), poly L glutamate (PLE), polyallylamine (PAA), and polyethylenimine (PEI) linear polymers. PLL and PLE exhibited significant CEST contrast, whereas no CEST contrast was observed for PAA and PEI. They reported sensitivity as a proton transfer enhancement (PTE) factor (Table 1.2), which is independent of concentration.

Van Zijl and co-workers further extended the idea of polypeptide based CEST agents using an array of 33 prototype polypeptides under three different categories, including poly-L-arginine (PLR) based, poly-L-lysine (PLK) based and, poly-L-threonine (PLT) based peptides. These polypeptides showed a very high proton transfer enhancement effect, which can effectively be used for *in vivo* applications [41].

Table 1.1. Correlation between expected sensitivity and observed sensitivity of paraCEST linear polymers

Agent		DP	Observed % CEST of the monomer	Observed % CEST of the polymer	Observed Sensitivity improvement of the polymer [column4/column3]	Percentage of monomeric sensitivity improvement caused by polymerization [column5/column2]	Ref.
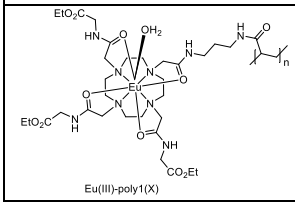 Eu(III)-poly1(X)	0.2 mM	17.4	2.4	25.3	10.5 fold	60.3	[20,38]
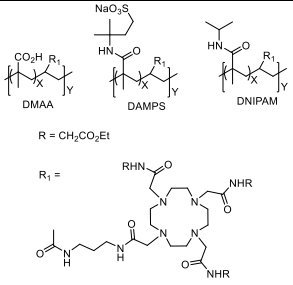 DMAA DAMPS DNIPAM $R = CH_2CO_2Et$ $R_1 =$	Eu-DMMA 1.1 (pH 6.0)[a]	22.6	2.5	45	18 fold	79.6	[39]
	Eu-DMMA 2.0 (pH 4.5)[a]	14.8	2.5	30	12 fold	81.0	
	Eu-DMMA 2.1 (pH 6.0)[a]	33.1	2.5	48	19.2 fold	58.0	
	Eu-DMMA 3.0 (pH 4)[a]	36.6	2.5	55	22 fold	60.1	
	Eu-DMMA 3.1 (pH 6.0)[a]	58.9	2.5	>60	>24.5 fold	>41.5	
	Eu-DMMA 4.1 (pH 6.0)[a]	12.7	2.5	25	10 fold	78.7	

[a]Different DMMA polymers are numbered depending on the pH and the MAA feed composition, NR=Not reported, DP-Degree of polymerization, MAA- Methacrylic acid

Polyuridylic acid (poly[rU]) is a single-stranded RNA consisting of uridine repeat units connected by phosphodiesters and showed CEST signals at 6.4 ppm and 10.8 ppm for hydroxyl

protons and imino protons respectively. Van Zijl and co-workers further improved the sensitivity enhancement factor obtained from PLL by mixing the positively charged PLL with poly[rU] [42].The sensitivity enhancement factor of over 5000 per imino proton permitted the detection of the micromolar concentration of the polymer (MW-644 kD and 2000 uridine units) with a 50% CEST contrast.

Table 1.2. Correlation between expected sensitivity and observed sensitivity of diaCEST linear polymers

Agent		DP	Observed % CEST	Expected % CEST	Observed Sensitivity (PTE)[b]	Expected Sensitivity (PTE)[b]	Ref.
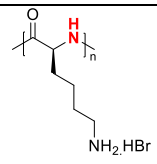 PLL 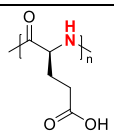 PLE 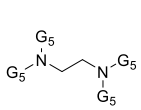 SDP-5 Where, G_5= 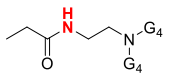 G_1= 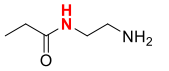	PLL (100 µM)	3338	43	53	586,431	583,000	[40]
	PLE (500 µM)	475	7	7	15,568	15,400	
	SD5 (1000 µM)	NR	51	40	44,080	44,000	
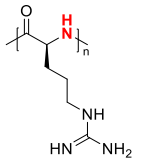 PLR 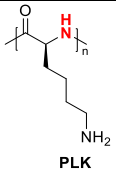 PLK 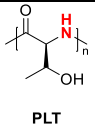 PLT	PLR	201	~15	NR	17,500	22,000	[41]
	PLK	205	~5	NR	12,500	16,900	
	PLT	63	~2.5	NR	6500	NR	

NR=Not reported, [b]Sensitivities were recorded as proton transfer enhancement (PTE)=({2[H_2O]/[peptide]}.MTR_{assym})/1000, poly L lysine (PLL), poly L glutamate (PLE), polyallylamine (PAA), polyethylenimine (PEI), poly-L-arginine (PLR), poly-L-lysine (PLK), poly-L-threonine (PLT)

Biopolymers have been used to enhance the CEST contrast. Liu and co-workers investigated CEST properties of different sizes of dextran, including 10 kDa, 70 kDa, 150 kDa, and 2000 kDa [43]. The CEST signal that corresponds to an -OH group in dextran has been observed at 0.9 ppm. There was no significant difference between the CEST contrast of different size dextran agents and the same concentration of glucose. However, there is a slight decrease in

CEST contrast in high molecular weight dextrans due to the reduced water accessibility of hydroxyl protons that are covered within larger molecules.

A dextran-based probe was successfully utilized for targeted CEST MRI of tumors that express prostate-specific membrane antigen (PSMA) by Van Zijl and co-workers (Figure 1.3a) [21]. A PSMA targeting moiety was conjugated to the dextran backbone via a spacer. A large number of -OH groups present in the dextran enhances the CEST contrast allowing it to be used in targeted imaging. The inherent low sensitivity of CEST MRI evades the problems with other agents used in targeted CEST imaging. However, the polymeric agent was able to achieve the exchangeable proton enhancement for good CEST contrast.

However, dextran hydroxyl protons resonate close to the water peak and make the CEST imaging problematic. Therefore, Pomper and co-workers conjugated salicylic acid probes to poly-isobutylene-maleic anhydride, comprised of 40 units of maleic acid (Figure 1.3b) for imaging of tumors bearing PSMA [18]. They were able to conjugate salicylic acid groups to the polymer backbone with 90% loading efficiency. However, contrast enhancement by 40 exchangeable protons is not sufficient for successful targeted CEST imaging and results in low CEST contrast.

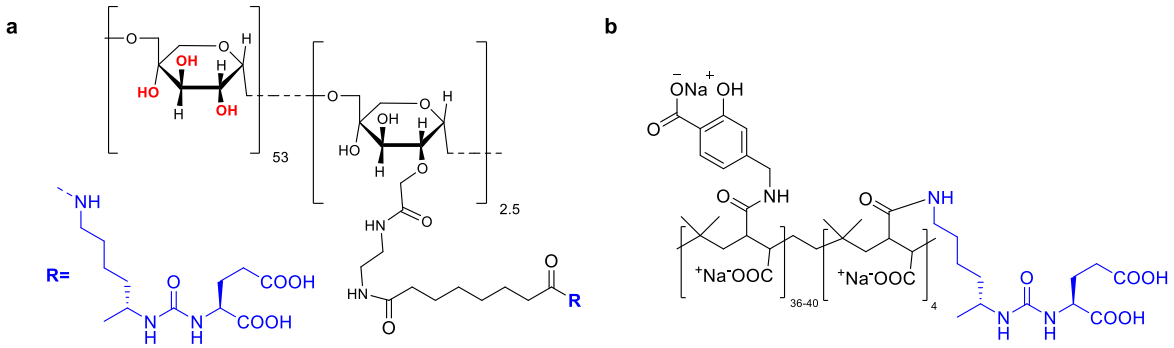

Figure 1.3. PSMA targeted diaCEST MRI probes that derived from polymers, a) dextran based and b) maleic anhydride-based polymers [21,18]

1.4.2 BRANCHED POLYMERS

Dendrimers are highly branched macromolecules that have multivalent characteristics and are extensively used in biomedical applications. Several factors make these dendritic architectures as an exciting platform to conjugate CEST MRI probes. The multivalent characteristics, well-controlled size, and purities inspire researchers to utilize them to enhance the CEST contrast.

1.4.2.1 PARACEST DENDRITIC AGENTS

There are several paraCEST dendritic agents reported to date. Grüll and co-workers reported the synthesis and application of Yb(III)DOTAM-functionalized poly(propylene imine) dendrimers [44]. They conjugated Yb-DOTAM complexes to generation one (G1) and generation 3 (G3) poly(propylene imine) dendrimers with four and sixteen agents per dendrimer, respectively (Figure 1.4). The paraCEST probe was attached to the dendrimer through an amide bond. Free Yb-DOTAM has two different exchangeable amide protons (-13.1 ppm and -16.1 ppm) before the conjugation, whereas a dendritic complex showed seven exchangeable amide protons between -12 ppm and -16 ppm. These amide signals are pH-dependent and used for pH mapping. They were able to lower the detection limit by a factor of 4 and 16 for G1 and G3 complexes, respectively.

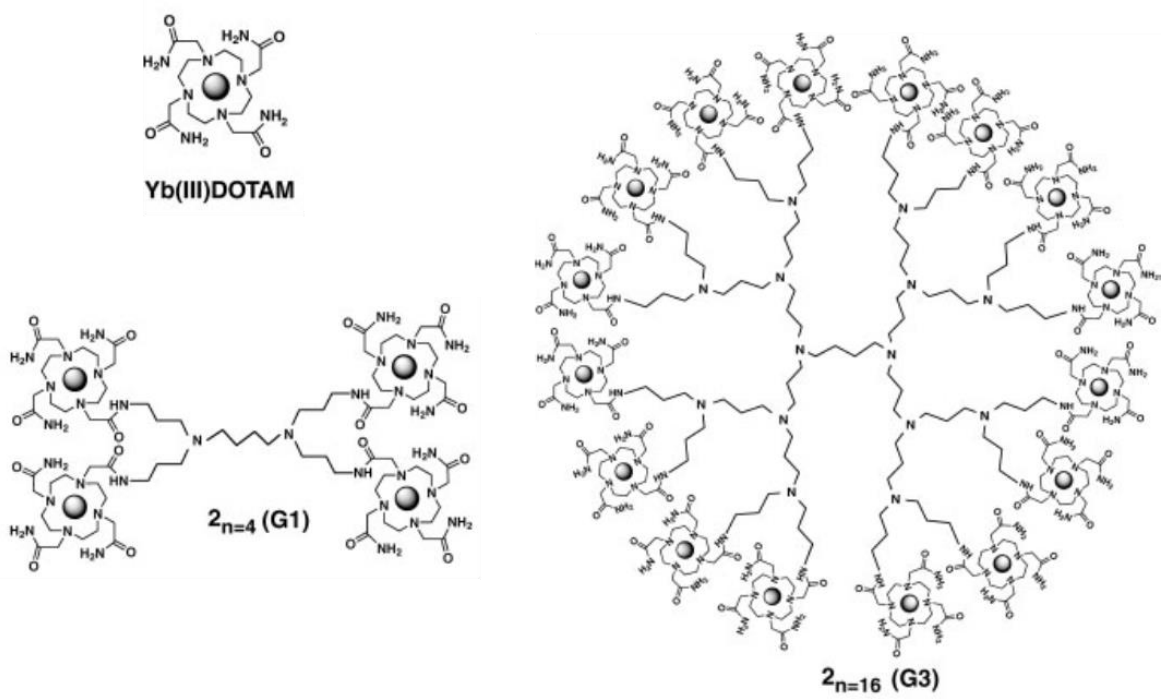

Figure 1.4. Yb(III)DOTAM-functionalized poly(propylene imine) dendrimers with different generation (G1 and G3). (Reproduced with permission from reference 44)

Our group previously reported PAMAM based G2 and G5 dendritic complexes with Yb and Eu metals respectively [45–47]. PAMAM G5 dendrimer theoretically consists of 128 surface groups. However, it is difficult to obtain the G5 PAMAM dendrimers with 128 surface groups due to defects in dendrimer branching. Therefore, when imaging probes are conjugated to the dendrimers, it is not possible to achieve more than 60% loading efficiency. Forty-one probes of Eu-DOTA-Gly-pBnNSC were able to attach to a G5-PAMAM dendrimer, which results in 32% loading efficiency. Six probes of Yb-DOTA-Gly-pBnNCS were able to conjugate to a G2 PAMAM dendrimer, which gives 37.5% loading efficiency (Figure 1.5). The detection limits of 79.8 μM and 335.5 μM were achieved for G5 and G2 complexes, respectively to give 5% CEST contrast.

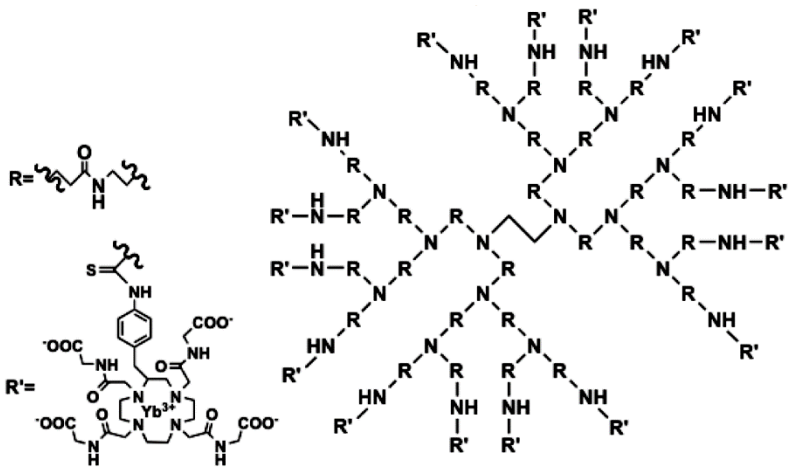

Figure 1.5. Yb-DOTA-Gly-pBnNCS functionalized G2 PAMAM dendritic paraCEST agent. (Reproduced with permission from reference 47)

1.4.2.2 DIACEST DENDRITIC AGENTS

McMahon and co-workers recently reported a salicylic acid-based dendrimer. They have conjugated salicylic acid to PAMAM G5 dendrimer to increase the salicylic acid protons [23]. A spacer molecule (succinic acid) was incorporated between the salicylic acid moiety and the dendrimer to lower the steric interactions. They synthesized a salicylic acid conjugated dendrimer with 40 salicylic acid probes per dendrimer, which increases the number of exchangeable protons in one molecule of the dendrimer. Their data indicates that the sensitivity of the salicylic acid dendrimer is increased for CEST imaging after conjugation of imaging probe to the dendrimer. The detection limit was lowered to 360 μM, which has approximately 15 mM in salicylic acid units.

To date, there are several other macromolecular CEST agents such as liposomes [29], biomolecules –albumin [37], viral particles [49], and hydrogels [10] that have been reported.

CHAPTER 2

DEVELOPMENT OF A POLYMER CEST MRI CONTRAST AGENT THAT MEASURES EXTRACELLULAR pH IN THE TUMOR MICROENVIRONMENT

2.1 INTRODUCTION

2.1.1 TUMOR ACIDOSIS

Tumor acidosis is a common characteristic of many solid tumors. The dysregulated metabolism of tumor cells relies on enhanced glycolysis, known as the Warburg effect, which produces excess lactic acid that is secreted from tumor cells [1-3]. This metabolic process causes the extracellular tumor microenvironment to become acidic, typically with an extracellular pH (pHe) of 6.4-7.0, and possibly even lower in pHe [4]. Therefore, measurements of tumor pHe may be used to improve tumor diagnoses, and monitor the effect of anti-cancer treatments that directly or indirectly change tumor glycolysis [5,6].

2.1.2 ACIDOCEST MRI

We have developed a noninvasive magnetic resonance imaging (MRI) method that measures tumor pHe, based on Chemical Exchange Saturation Transfer (CEST) [7,8]. This method selectively saturates the MR signal of a proton on an agent with a radiofrequency pulse, causing the MR signal to disappear (Figure 2.1a, left). Subsequent chemical exchange of this proton with a proton on water causes the water signal to decrease (Figure 2.1a, right). We refer to this decrease in water MR signal as a 'CEST signal', which can be detected using conventional MR image acquisition methods. The chemical exchange of many types of exchangeable protons are base-catalyzed, and therefore the CEST signal is dependent on pH. More specifically, we have shown that the ratio of two CEST signals generated by selective saturation of two types of exchangeable protons can be used to measure pH in a concentration-independent manner, a process known as acidoCEST MRI [9]. We have used acidoCEST MRI to perform many pre-clinical imaging studies with paramagnetic agents [10-12] and diamagnetic agents [13-27], and we have translated acidoCEST MRI for clinical imaging evaluations [28]. Other research programs have

developed and used similar acidoCEST MRI methods with paramagnetic agents [29-34] and diamagnetic agents [35-45] that have two selectively detectable CEST signals, or agents that generate two CEST signals by using two saturation powers [46-51].

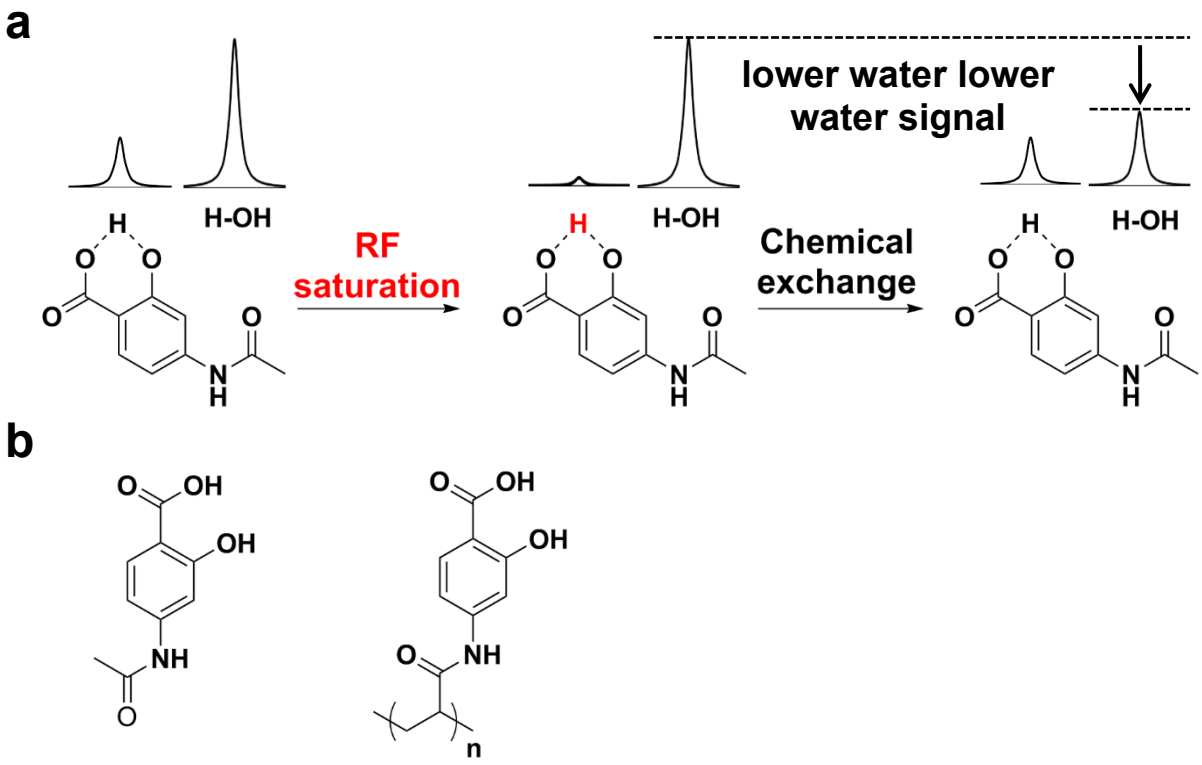

Figure 2.1. CEST MRI of the monomer and polymer CEST agents. (a) A schematic of the CEST MRI process. RF saturation is applied that causes a proton to lose its coherent magnetic signal. Then the saturated proton undergoes chemical exchange from the agent to water, which effectively transfers the saturation to water and lowers the water signal. Finally, the lower water signal is acquired using standard MRI methods. (b) Chemical structures of studied monomer agent (left) and polymer agent (right; n = ~125) with amide and salicylic acid protons that resonate at 5.0 ppm and 9.2 ppm respectively.

CEST MRI is an insensitive imaging technique [7,8]. As an advantage, one agent molecule can affect the MR signal of approximately 100 to 1000 water molecules due to the multiplication

effect of the chemical exchange rate that is on the order of 100-1000 Hz. However, CEST must suppress the MR signal of ~1 M of water protons to suppress 1.3% of the ~78 M of water protons in biological tissues (assuming that 1.3% is a minimally detectable CEST signal, pure water is 55.5 M and water protons are 111 M, and the water concentration in most tissues is ~70%). Therefore, the CEST agent with a 100-1000 Hz exchange rate must have a minimum concentration of approximately 1-10 mM to affect ~1 M of water protons during CEST MRI studies. Our acidoCEST MRI method uses iopamidol, a clinically approved contrast agent that can be administered at 972 mM concentration to pre-clinical tumor models and patients who have cancer [9]. However, even this high concentration of a well-tolerated agent can fail to deliver enough agent throughout the tumor tissue, causing pHe measurements with acidoCEST MRI to be spatially incomplete.

2.1.3 A NANOSIZED AGENT TO DETECT TUMOR ACIDOSIS

To address the low sensitivity problem, we proposed that a nanoscale agent may deliver a greater payload of exchangeable protons to tumor tissue. A variety of nanoscale CEST agents have been developed that use polymers, dendrimers, proteins, and viral particles to generate a strong CEST signal [52-73]. Paramagnetic nanoscale agents have the advantage of very large MR frequencies (also known as chemical shifts) that are well separated from the MR frequency of water (defined as 0 ppm for MRI studies) [52-63]. This frequency separation allows the selective saturation of the agent's MR resonance to be performed with high radiofrequency power, which further improves CEST detection. However, paramagnetic agents often use potentially toxic lanthanide metals, or use other metals that have unstable oxidation states especially under *in vivo* conditions [74]. Therefore, diamagnetic nanoscale agents that are nonmetallic have advantages for biomedical studies [64-73]. Notably, the first research studies with paramagnetic and

diamagnetic nanoscale agents were first reported in 2003 [52], but reports of paramagnetic nanoscale agents have not appeared since 2008 [56] while studies with diamagnetic nanoscale agents have continued.

Surprisingly, diamagnetic nanoscale CEST agents have not yet been developed for acidoCEST MRI applications that measure tumor pHe. Therefore, we sought to develop such an agent that can potentially improve the comprehensive spatial interrogation of tumor tissues. We used 4-amidosalicylate as a monomeric unit to develop a nanoscale polymer, because this monomer has two types of exchangeable protons that are known to have high MR frequencies, which facilitates selective saturation and potentially allows for the use of higher saturation powers that can improve detection sensitivity (Figure 2.1b). We designed this polymer to have >100 exchangeable protons, to investigate if the higher payload of exchangeable protons can improve CEST sensitivity on a per-molecule basis. We also investigated acidoCEST MRI of the monomer agent, 4-acetamido-2-hydroxybenzoic acid that has a similar electronic structure as the polymer agent. We first performed detailed acidoCEST MRI studies with chemical samples to evaluate if the new agents can measure pH with an acidoCEST MRI protocol. We then performed a preliminary *in vivo* study with a tumor model of mammary carcinoma using acidoCEST MRI with the polymer agent, monomer agent, and iopamidol, to evaluate the utility of a nanoscale agent for this biomedical imaging application.

2.2 MATERIALS AND METHODS

2.2.1 MATERIALS

Dry solvents were purchased and used without further purification or drying treatment. ACS grade solvents for chromatography, Na_2SO_4, PBS buffer (pH 7), and dialysis cassettes (10K MWCO) were purchased from Fisher Scientific (part of Thermo Fisher Scientific, Waltham, MA, USA). Sodium 4-aminosalicylate and acryloyl chloride were purchased from Alfa Aesar (Tewksbury, MA, USA). 4,4′-azobis(4-cyanovaleric acid) and acetic anhydride were purchased from Sigma-Aldrich (St. Louis, MO, USA). NMR spectroscopy was performed with a 600 MHz NMR spectrometer (Bruker Biospin, Corp., Billerica, MA, USA). LC-MS studies were conducted using a Waters Acquity^{TM} UPLC-MS system with an Acquity UPLC$^{®}$ BEH C-18 1.7 µm, 2.1 mm×50 mm column, UV detection between 200 and 400 nm (2996 PDA detector) and a TQ detector mass spectrometer with electrospray ionization (ESI).

2.2.2 CHEMICAL SYNTHESIS

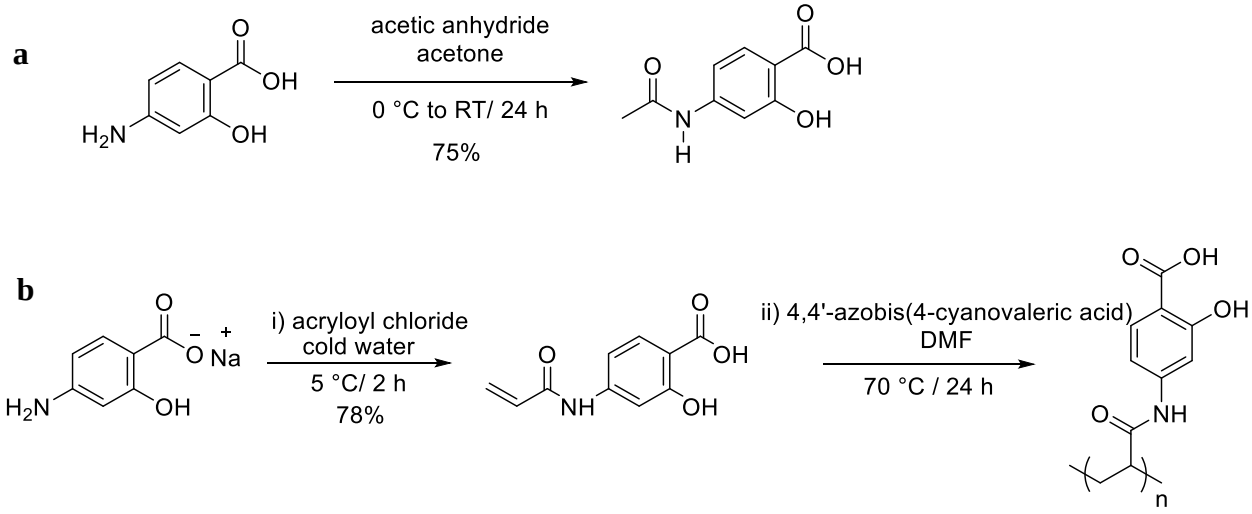

Scheme 2.1 Chemical Synthesis of (a) the monomeric agent and (b) the polymeric agent, where n is approximately 125 monomeric units.

2.2.2.1 CHEMICAL SYNTHESIS OF 4-ACETAMIDO-2-HYDROXYBENZOIC ACID [75]

4-aminosalicylic acid (1.53 g, 10.01 mmol) was dissolved in anhydrous acetone (30 mL) under Ar. Then the solution was cooled using an ice bath. While stirring, acetic anhydride (1 mL, 10.58 mmol) was added, and the reaction mixture was allowed to stir for 24 hrs. Organic solvent was evaporated under vacuum, and the solid residue was washed with water and filtered. The resulting compound was resuspended in a small amount of water and lyophilized to yield a dry final compound (white powder, 1.46 g, 75%). ^{1}H NMR (600 MHz, DMSO- d_6) δ (ppm): ^{1}H NMR (600 MHz, DMSO-d_6) δ 11.39 (s, 1H, OH), 10.19 (s, 1H), 7.71 (d, J = 8.7 Hz, 1H), 7.35 (d, J = 2.0 Hz, 1H), 7.04 (dd, J = 8.6, 2.1 Hz, 1H), 2.07 (s, 3H). LRMS-ESI (m/z): $[M+H]^+$ calc'd for [$C_9H_9NO_4$], 196.05; found, 196.01

2.2.2.2 CHEMICAL SYNTHESIS OF 4-ACRYLAMIDOSALICYLIC ACID [76]

Sodium 4-aminosalicylate (4 g, 0.018 mol) was dissolved in ice-cold distilled water (50 ml) and stirred for 1 h at 5 °C. Then acryloyl chloride (2.35 mL; 0.029 mol) was added as two separate additions (1.5 mL and 0.85 mL) and the solution was stirred for 1 h after each addition at 5 °C. A white precipitate formed. The precipitate was filtered off and extensively washed with distilled water (200 mL). Then the product was lyophilized to obtain dry 4-acrylamidosalicylic acid (white powder, 3.12 g, 78%). ^{1}H NMR (600 MHz, DMSO-d_6) δ 13.70 (s, 1H), 11.35 (s, 1H), 10.38 (s, 1H), 7.73 (d, J = 8.7 Hz, 1H), 7.50 – 7.39 (m, 1H), 7.12 (dd, J = 8.7, 2.1 Hz, 1H), 6.44 (dd, J = 17.0, 10.2 Hz, 1H), 6.29 (dd, J = 17.0, 2.0 Hz, 1H), 5.81 (dd, J = 9.9, 1.7 Hz, 1H). LRMS-ESI (m/z): $[M+H]^+$ calc'd for [$C_{10}H_9NO_4$], 208.05; found, 208.06

2.2.2.3 CHEMICAL SYNTHESIS OF THE POLYMER AGENT

4-acrylamidosalicylic acid (1.0 g, 0.0048 mol) and 4,4′-azobis(4-cyanovaleric acid) (0.05 g, 0.18 mmol, 5% w/w) were dissolved in DMF (25 mL) under Ar and stirred at 70 °C for 24 hrs. Then the reaction mixture was diluted with water and a white precipitate formed. Then the reaction mixture was dialyzed with a 10,000 MWCO filter against water and lyophilized to obtain the final polymer. This final polymer agent was analyzed by ^{1}H-NMR, gel permeation chromatography (GPC) and mass spectrometry (MALDI-TOF).

2.2.3 CHEMICAL CHARACTERIZATION

2.2.3.1 GEL PERMEATION CHROMATOGRAPHY

The molecular weight of the polymer agent was determined using an Agilent HPLC system with a UV detector and a Phenomenex SEC-S-3000 column (300×7.8 mm). A 1x PBS buffer was used as an eluent with 0.5 mL/min flow rate. Sodium polystyrene sulfonate standards were employed for instrument calibration.

2.2.3.2 MALDI-TOF

The MALDI-TOF spectrum of the polymer agent was recorded with a Bruker Autoflex Speed MALDI-TOF spectrophotometer, using 2,5-dihydroxybenzoic acid (DHB) as a matrix. The matrix and polymer were dissolved in a solvent system of 50:50 water: acetonitrile with 0.1% TFA. Samples were loaded onto a target plate and mixed on the target with 1 μL of supernatant of saturated matrix solution. All the MALDI spectra were acquired in linear mode, which was operated over a mass range from 500 to 75,000 Da. The number of shots and laser power was adjusted to improve spectrum quality.

2.2.3.3 UV-VIS SPECTROSCOPY

Monomer and polymer agents were dissolved in 0.01 mM PBS buffer and UV spectral scans was taken between 230 nm and 400 nm using the Synergy H4 microplate reader (BioTek instruments, Inc., Winooski, VT, USA)

2.2.3.4 SCANNING ELECTRON MICROSCOPY (SEM)

The polymer agent was dissolved in 0.1 M PBS buffer and a drop was placed onto a 12 mm diameter glass coverslip and allowed to dry overnight. The dissolved polymer agent and the dried polymer agent were both mounted on to double-stick carbon tabs (Ted Pella. Inc., Redding, CA), which have been previously mounted on to a glass microscope slide. The samples were then coated under vacuum using a Balzer MED 010 evaporator (Technotrade International, Manchester, NH) with platinum alloy for a thickness of 25 nm, then immediately flash carbon coated under vacuum. The samples were transferred to a desiccator for examination at a later date. Samples were examined/imaged in a JSM-5910 scanning electron microscope (JEOL, USA, Inc., Peabody, MA) at an accelerating voltage of 15 kV.

2.2.3.5 TRANSMISSION ELECTRON MICROSCOPY (TEM)

The polymer agent was dissolved in 0.1 M PBS buffer and a drop was placed onto 100 mesh formvar/carbon coated copper grids treated with poly-l-lysine for approximately 1 hour. The sample was blotted from the grid with filter paper and was allowed to dry. The sample was then examined in a JEM 1010 transmission electron microscope (JEOL, USA, Inc., Peabody, MA) at an accelerating voltage of 80 Kv. Digital images were obtained using the AMT Imaging System (Advanced Microscopy Techniques Corp., Danvers, MA).

2.2.4 *IN VITRO* CYTOTOXICITY ASSAY

The cytotoxicity evaluations of the monomer and polymer agents were performed using an MTT cell growth assay kit (EMD Millipore Chemicon®). Approximately 1×10^5 cells mL^{-1} of MDA-MB-231 mammary carcinoma cells in their exponential growth phase were seeded in a flat-bottomed 96-well polystyrene coated plate and were incubated for 24 hours at 37 °C in a 5% CO_2 incubator. Then media was removed and 100 μL of media was added to the plate that included a range of concentrations (0.125 mM, 0.625 mM, 1.25 mM, 6.25 mM, 12.5 mM and 62.5 mM) of the monomer or the "monomeric unit concentration" of the included polymer. After 24 hours of incubation at 37 °C, the media was removed and 10 μL of MTT reagent was added to each well containing new media and incubated at 37 °C for 4 hrs. Afterwards, formazan crystals that formed in each well were dissolved in isopropanol with 100 μL of 0.04 N HCl and plates were read at 570 nm in a microplate reader (SYNERGY H4 reader, Bio Tek Instruments, Inc, VT, USA). Wells with complete medium, MTT reagent, or without cells were used as control samples.

2.2.5 ACIDOCEST MRI OF CHEMICAL SAMPLES

The monomer and polymer agents were prepared at 1.25 - 40 mM and 95 - 300 μM concentrations in 10 mM PBS, respectively. The pH was adjusted using a benchtop pH meter and very small volumes of HCl and NaOH that did not significantly affect agent concentrations (Mettler Toledo Seven compact S220 pH meter, Columbus, OH). Samples were placed in a customized holder (Figure 2.3a,b) that maintained the samples at 37.0 ± 0.2 °C, or at 25.0, 29.0, 34.0, 42.0, 45.0, or 49.0 °C during temperature-dependent studies. Our customized sample holder was filled with 2% agarose to reduce B_1 and B_0 inhomogeneities. We incubated our samples and holder at the desired temperature for 4-18 hours prior to each MRI study. We used warm air and an automated temperature feedback system to maintain temperature in the MRI magnet (SA

Instruments, Stony Brook, NY). We validated our sample temperatures by using the same holder to analyze samples of ethylene glycol, and using localized MR spectroscopy to validate temperature, which is an ideal method for measuring the temperature of chemical solutions without disturbing the solutions in the MRI magnet [85].

MRI studies were performed with a Bruker Biospec MRI scanner operating at 7 Tesla (T; 300 MHz) magnetic field strength with a 72 mm volume transceiver coil (Bruker Biospin, Inc., Billerica, MA). To identify the location of the samples in the magnet, an initial set of images were acquired using a multislice spin echo MRI protocol with the following parameters: 750 ms repetition time (TR); 10 ms echo time (TE); 180° excitation flip angle (FA); coronal image orientation; 64 × 64 matrix; 5.12 × 5.12 cm field-of-view (FOV); 0.8 × 0.8 mm in-plane spatial resolution; 1 mm slice thickness (SL); 40 slices; 1 average; 48 s total scan time. We used a CEST-FISP (fast imaging with steady-state free precession) MRI acquisition protocol with the following parameters: 4.9832 ms TR; 2.2916 ms TE; 30° FA; centric encoding; coronal image orientation; 256 × 256 matrix; 5.12 × 5.12 cm FOV; 0.2 × 0.2 mm in-plane spatial resolution; 1 mm SL; 1 slice; and 1 average [86]. We acquired CEST images with selective saturation applied at 4 μT for 6 s at saturation frequencies in 0.1 ppm increments from -13 ppm to 13 ppm, for a total scan time of 28.0 minutes. We also collected images at 0.5 to 6.0 μT saturation powers (at 6 s saturation time), and at 1 – 8 s saturation times (at 4 μT saturation power).

Images were processed using ParaVision v5.1, and CEST MR image analyses were performed with Matlab 2018b (The MathWorks, Inc., Natick, MA). To measure CEST signal amplitudes, each CEST spectrum from a region of interest (ROI) was analyzed by fitting the spectrum to a sum of three Lorentzian line shapes to account for two CEST signals (5.0 ppm and

9.2 ppm) and direct saturation of water [87]. The center, width, and amplitude of each Lorentzian line were allowed to change in order to obtain optimal fit.

2.2.6 *IN VIVO* ACIDOCEST MRI STUDIES

All *in vivo* mouse studies were conducted with the approval of the Institutional Animal Care and Use Committee of the MD Anderson Cancer Center in accordance with applicable guidelines and regulations. A subcutaneous model of MDA-MB-231 mammary carcinoma was developed by injecting 10^6 tumor cells in the right rear flank of 8 female mice that were 6-8 weeks old. Tumors were allowed to grow for 5-6 weeks to a diameter of 3-6 mm before imaging studies. Two mice were analyzed with acidoCEST MRI three times during sequential scans performed on Day 0, 2, and 4 (where Day 0 indicates the first scan for the mouse). These sequential scans used iopamidol on Day 0, the monomer agent on Day 2, and the polymer agent on Day 4. Six additional mice were analyzed with acidoCEST MRI only one time, using only iopamidol for two mice, the monomer agent for two mice, and the polymer agent for two mice.

To prepare for each imaging scan, a mouse was anesthetized with 1.5-2.0% isoflurane in 100% oxygen carrier gas. A tail vein was catheterized with a 27g needle. The mouse was then placed in a customized cradle, and respiratory and rectal temperature leads were positioned to monitor respiration and core body temperature throughout the imaging scan (SA Instruments Inc., Stony Brook, NY). Body temperature was maintained at 37.0±0.2 °C using warm air. To localize the tumor within an image, we performed anatomical MRI scans with each mouse using the multislice spin echo MRI protocol with following parameters: 1000 ms TR; 5.42 ms TE; 90º FA; axial image orientation; 128×128 matrix; 3.84×3.84 cm FOV; 0.3×0.3 mm in-plane spatial resolution; 1 mm SL; 30 slices; 1 average; 2:08 min total scan time.

In vivo acidoCEST MRI was performed using CEST FISP protocol with following parameters: 3.310 ms TR; 1.655 ms TE; 15° FA; centric encoding; axial image orientation; 128 × 128 matrix; 3.84 × 3.84 cm FOV; 0.3 × 0.3 mm in-plane spatial resolution; 1 mm SL; 1 slice; 1 average. Four image sets were first acquired to produce CEST spectra for each image pixel prior to intravenous administration of the contrast agent. Then, 200 μL of 976 mM iopamidol, 250 mM monomer agent, or 2 mM polymer agent (equivalent to 250 mM in monomer units) were injected intravenously. These injection concentrations equate to 7.8, 2.0, and 0.016 mmol/Kg of mouse body weight, respectively. The injection line was connected to an infusion pump that infused 400 μL/hour of agent during the next 30 minutes. Six sets of CEST MR images were acquired immediately after injection to produce six post-injection CEST spectra for each imaging pixel. We acquired CEST images with selective saturation applied at 3 μT for 6 s at saturation frequencies of 14.0 ppm (which was subsequently discarded during analysis because this initial image was not acquired with steady-state saturation conditions); 13.0 to 3.0 ppm in increments of 0.4 ppm; 2.5 to -2.0 ppm in increments of 0.5 ppm; and -3.0 to -12.0 ppm in increments of 3 ppm for a total of 40 saturation frequencies that required a total scan time of 4:23 minutes.

CEST MR images were analyzed using our previously reported methods [15,17]. Images were averaged that were acquired before injection of agent and at the same saturation frequency. Post-injection images at each saturation frequency were also averaged. Each averaged image was processed by Gaussian spatial smoothing to improve signal-to-noise. These processed pre-injection images were subtracted from the processed post-injection images to remove endogenous CEST signals that are the same before and after injection. The resulting CEST spectra for each pixel were fit with the sum of three Lorentzian line shapes to measure the amplitude of CEST signals at 5.0 and 9.2 ppm, and to account for the direct saturation of water at 0 ppm. The pH was

estimated based on a $\log_{10}$ ratio of the two CEST signals (Figure 2.6 for the monomer and polymer agents, and reference 17 for iopamidol).

2.3 RESULTS AND DISCUSSION

2.3.1 SYNTHESIS AND CHARACTERIZATION OF MONOMER AND POLYMER AGENTS

The monomer, 4-acrylamidosalicylic acid, was synthesized by following a previously reported method with minor modifications (Scheme 2.1.b) [75]. 4-acrylamidosalicylic acid was then polymerized using 4,4'-azobis(4-cyanovaleric acid) as initiator in DMF at 70 °C to afford the linear polymer. The polymer was purified by dialysis using a 10 kD MW cutoff membrane. We also synthesized a monomer agent (Scheme 2.1.a). The polymer agent was purified using dialysis with a 10,000 MWCO, and the monomer agent was purified using HPLC.

UV-VIS spectra (Figure 2.2a) further confirmed the presence of the salicylic acid repeating groups in the polymer, based on the characteristic maximum absorption wavelength for salicylic acid at approximately 310 nm. The resolved repeat units shown in a MALDI-TOF spectrum (Figure 2.2b) were separated by 207.04 g/mol, which confirmed that the analyte was a polymer that exclusively contained the salicylic acid-based monomer. Gel permeation chromatography (GPC) results showed that the weight average molecular weight (Mw) of the polymer agent was 26,000 g/mol with a 1.8 polydispersity index, (Figure 2.2c). SEM and TEM of the polymer agent showed a variable morphology and particle size of the polymer with an average particle size of 361 nm, and a range from 45 to 710 nm, as expected based on high polydispersity index from GPC (Figure 2.2d).

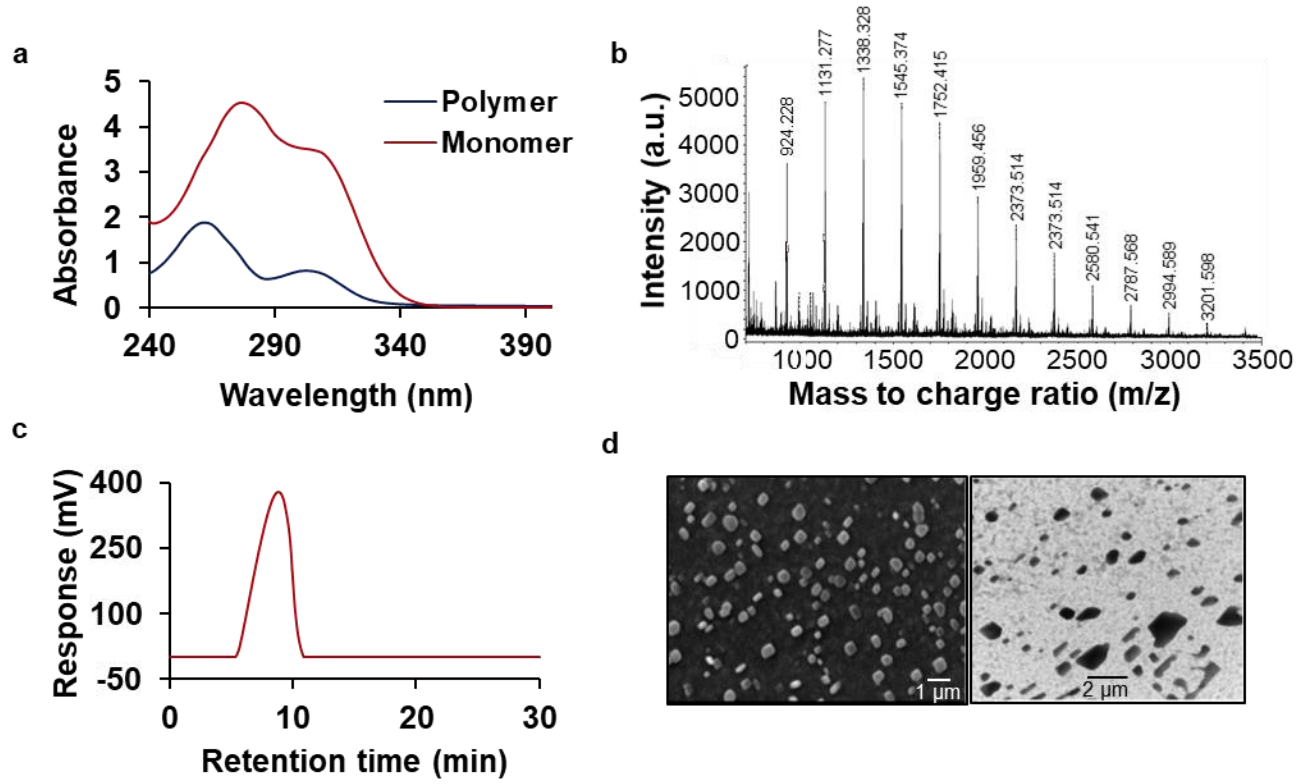

Figure 2.2. Chemical characterization of the monomer and polymer agents. (a) UV-Vis spectra of the monomer and polymer agents at pH 7.0. (b) A MALDI-TOF spectrum of the polymer. (c) A gel permeation chromatography trace of the polymer. (d) An SEM image (left) and a TEM image (right) of the polymer

2.3.2 ACIDOCEST MRI OF CHEMICAL SAMPLES

The CEST properties of the monomer and polymer agents were assessed over a range of pH values at 37.0 ºC and 7T magnetic field strength. The Z spectra (which show the Z-axis magnetization after steady state CEST saturation; Figure 2.3c,d) were analyzed by fitting a sum of three Lorentzian line shapes to the experimental results (Figure 2.3e,f). The samples were placed in our customized holder with agarose gel (Figure 2.3a) that reduced B_0 and B_1 magnetic field inhomogeneities and greatly improved the quality of our CEST results, as evidenced by the low residuals of the Lorentzian line fitting analysis (Figure 2.3e,f).

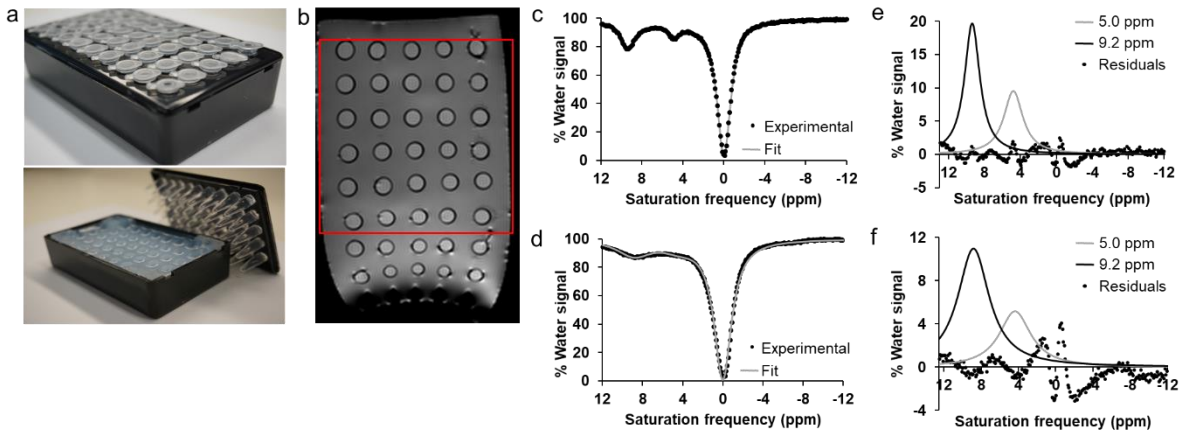

Figure 2.3. CEST MRI of chemical samples. (a) A 2.5 x 6 x 10 cm plastic box was filled with 2% agarose to create a sample holder, and samples were placed into holes in the top of the holder. (b) A spin echo MR image of the samples in the holder was used to localize a 6 x 6 cm coronal field of view for subsequent imaging, as shown by the red rectangle. A Z-spectrum of (c) the monomer agent and (d) the polymer agent was acquired with 6 s of 4 μT saturation. The experimental spectrum was fit with Lorentzian line shapes to produce a Lorentzian CEST spectrum of (e) the monomer agent and (f) the polymer agent. The low residuals around the Lorentzian shaped peaks at 5.0 and 9.2 ppm indicate that the line fitting method was reliable.

CEST MRI measurements revealed that both agents show CEST signals at 5.0 ppm and 9.2 ppm, which is consistent with CEST signals of similar agents (Figure 2.4a,d) [76-81]. The CEST signal at 5.0 ppm in the polymer agent is not as strong as in the monomer agent. This lower contrast may be due to steric blocking between water molecules and the amide in the polymer due to the proximity of the amide to the polymer backbone, relative to the water-amide interactions of the monomer agent and the water-salicylic acid interactions in the polymer and monomer. Steric blocking can reduce the chemical exchange rate (k_{ex}), resulting in a lower CEST signal. A similar result has been previously observed with other polymeric CEST agents [67].

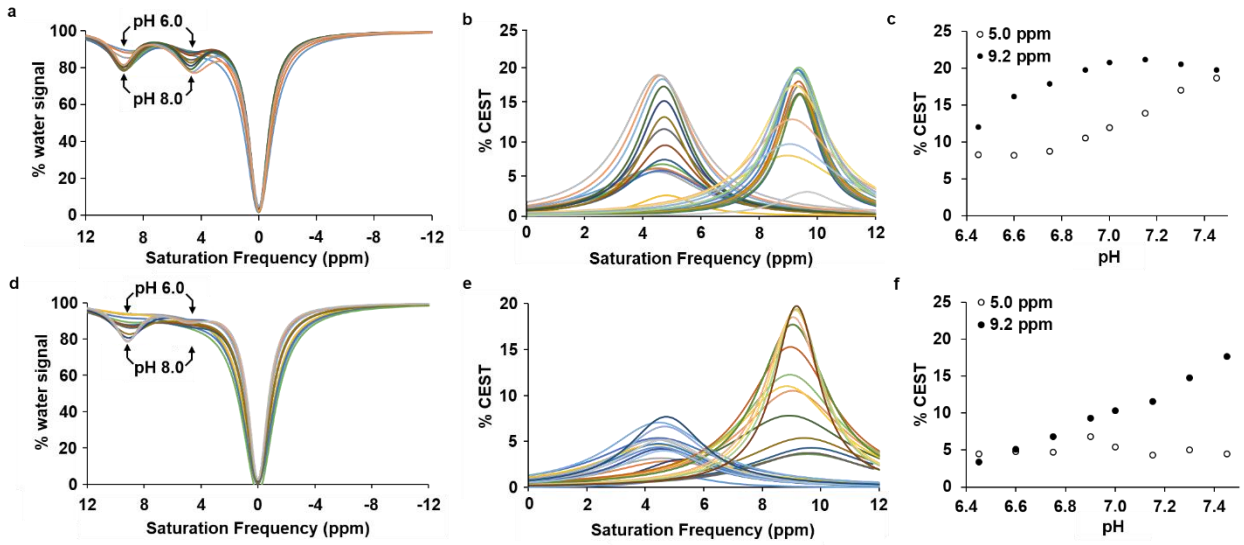

Figure 2.4. CEST properties of the monomer and polymer agents. Samples consisted of 20 mM and 0.16 mM of each agent, respectively, and were analyzed at 37 °C, 4 μT saturation power and 6 sec saturation time. (a) The Z-spectrum, (b) the CEST Lorentzian spectrum, and the (c) CEST-pH graph of the monomer agent, and (d-f) similar spectra and graph for the polymer agent show the pH dependence of the CEST effects for these agents. The pH values ranged from 6.0 to 8.0 in 0.1 - 0.15 unit increments.

The Z-spectra (Figure 2.4a,d) and the CEST Lorentzian spectra (Figure 2.4b,e) show the pH-dependence of the CEST effects for both agents. Interestingly, the monomer and polymer agents exhibited different pH dependencies (Figure 2.4c,f). In general, the chemical exchange process of the salicylic acid and amide are known to be base-catalyzed. A faster k_{ex} causes greater CEST signal, until k_{ex} becomes too fast for the CEST process (Figure 2.1b) and less CEST can be generated. The CEST signal for the salicylic acid of the monomer agent (Figure 2.4c, filled circles) follows this classic description, because k_{ex} of salicylic acid is moderate at low pH, reaches a faster rate that is ideal for generating CEST at pH ~7.1 (at 37.0 ºC and 7T magnetic field strength), and even faster k_{ex} at higher pH > 7.1 generates less CEST signal. For comparison, k_{ex} for the amide of the monomer agent is low at low pH, and increases with increasing pH, but does not reach an

ideal k_{ex} value for the greatest CEST signal until a pH value > 7.5, causing the CEST-pH relationship to be monotonic for the amide at pH < 7.5 (Figure 2.4c, open circles). The salicylic acid of the polymer agent has a similar CEST-pH relationship as the amide of the monomer agent (Figure 2.4f, filled circles), indicating that the k_{ex} for the polymeric salicylic acid is low at low pH (relative to the monomeric salicylic acid), and increases with increasing pH, but does not reach an ideal k_{ex} value for the greatest CEST signal until a pH value > 7.5. Finally, the amide of the polymer agent has a low CEST signal at all pH values, indicating a low k_{ex} (especially relative to the monomeric amide) that does not appreciably increase with increasing k_{ex} values (Figure 2.4f, open circles). The slower k_{ex} of the polymer agent relative to the monomer agent may be due to intramolecular hydrogen bonding within the polymer. Indeed, hydrogen bonding within a salicylic acid moiety is known to reduce k_{ex} from this group relative to k_{ex} of hydroxyl and carboxylic acid groups, showing that hydrogen bonding affects CEST [76].

2.3.3 OPTIMIZATION OF CEST SATURATION CONDITIONS

We optimized the saturation power for acidoCEST MRI with the monomer and polymer agent to find the best saturation power (Figure 2.5a,b). The HW-QUESP method was used to determine that % CEST at 5.0 and 9.2 ppm reached >80% and >65% of maximum CEST signal at 4.0 μT saturation power for the monomer and polymer agents, respectively [82]. A saturation power of 4 μT has been used as a safe power level for *in vivo* imaging [8], so this power was selected as a power level for subsequent experiments. The RL-QUEST method was used to evaluate the effect of saturation time, which exhibited that % CEST at 5.0 and 9.2 ppm reached >98% of maximum CEST signal at 6 s saturation time for both monomer and polymer agents (Figure 2.5c,d) [83]. Therefore, we used a 6 s saturation time for our subsequent studies. Importantly, these analyses were performed with monomer and polymer agent concentrations of

20 mM and 160 μM, respectively, showing that the polymer can generate detectable CEST signals with a 125-fold reduction in agent concentration relative to the monomer.

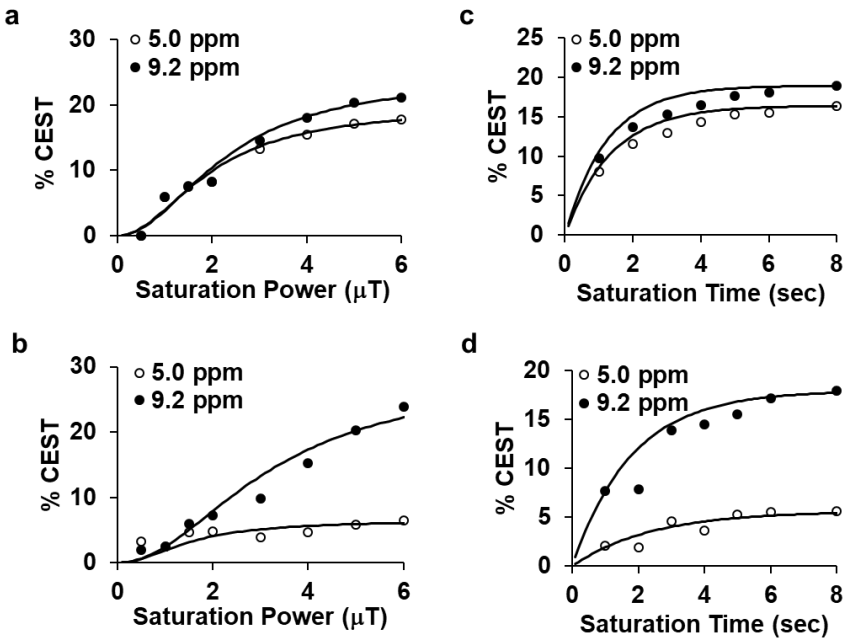

Figure 2.5. The dependence of CEST on saturation conditions. The CEST measurements of (a) 20 mM monomer agent and (b) 0.16 mM polymer at 6 s saturation time, pH 7.4, 37 °C and varying saturation power were fitted using the HW-QUESP method. The CEST measurements of (c) monomer agent and (d) polymer agent were obtained at 4 μT saturation power, pH 7.4 and varying saturation time, and were fit using the RL-QUEST method.

2.3.4 MEASURING pH WITH ACIDOCEST MRI

We investigated the ability of the monomer and polymer agents to measure pH via CEST MRI, using our variation of this imaging method known as acidoCEST MRI [9]. Samples ranging from pH 6.4 to 7.5 were imaged with optimized saturation conditions, and the results were used to calibrate a $\log_{10}$ ratio of agent's CEST effects with pH. Both calibrations were linearly correlated with pH within this physiological pH range with a R^2 value of 0.97 and 0.98 for monomer and polymer agents, respectively (Figure 2.6a,b). The calibrations showed opposite trends due to the

different regimes of k_{ex} for the faster-exchanging monomer agent vs. the slower-exchanging polymer agent, as described above, and shown in Figure 2.4c,f. These calibrations were used to calculate the pH for each pixel within acidoCEST MR images of samples that consisted of each agent over a range of pH values (Figure 2.6c,d). Therefore, we can use these calibration curves to determine the pH from MR images.

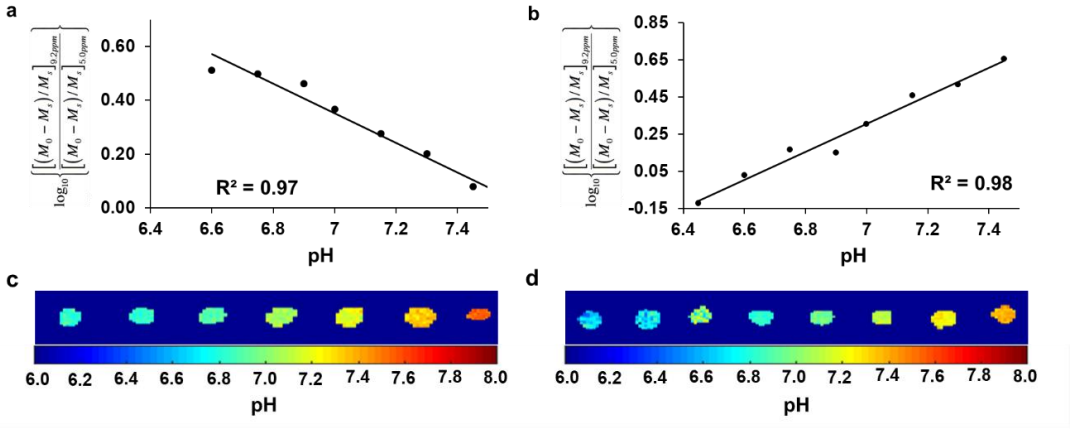

Figure 2.6. CEST MRI of the monomer and polymer agents can measure pH. CEST properties of 20 mM monomer agent and 0.16 mM polymer agent were measured at 37 °C, 4 μT saturation power and 6 sec saturation time. A ratio based on CEST at 9.2 and 5.0 ppm is linearly correlated with pH within the physiological pH range (6.4 and 7.5 units), for the (a) monomer agent and (b) the polymer agent. These calibrations were used to convert % CEST signal to pH values for each pixel within the MR images of samples that contained (c) monomer agent at pH values of 6.6, 6.75, 6.9, 7.0, 7.15, 7.3, and 7.45 units, and (d) polymer agent at pH values of 6.45, 6.6, 6.75, 6.9, 7.0, 7.15, 7.3, and 7.45 units.

2.3.5 EVALUATION OF ENVIRONMENTAL CONDITIONS ON ACIDOCEST MRI

To examine how temperature affects pH measurements with acidoCEST MRI, CEST spectra were collected for the monomer and polymer agents between 25 and 49 °C and analyzed to measure % CEST values (Figure 2.7). For the monomer agent, the CEST signal increased with increasing temperature for CEST generated from the amide and salicylic acid, as expected.

However, the pH measurement had a negligible dependence on temperature (ΔpH = 0.0089 units per ºC; R^2 = 0.89), because our ratiometric analysis method largely negates the effect of temperature. For the polymer agent, there was no significant change in CEST signal with increasing temperature for CEST generated from the amide and salicylic acid, and therefore the pH measurement had a negligible dependence on temperature (ΔpH = 0.0097 units per ºC; R^2 = 0.84). This result was an improvement relative to the minor yet non-negligible temperature dependence of acidoCEST MRI measurements performed with a paramagnetic CEST agent [12,84].

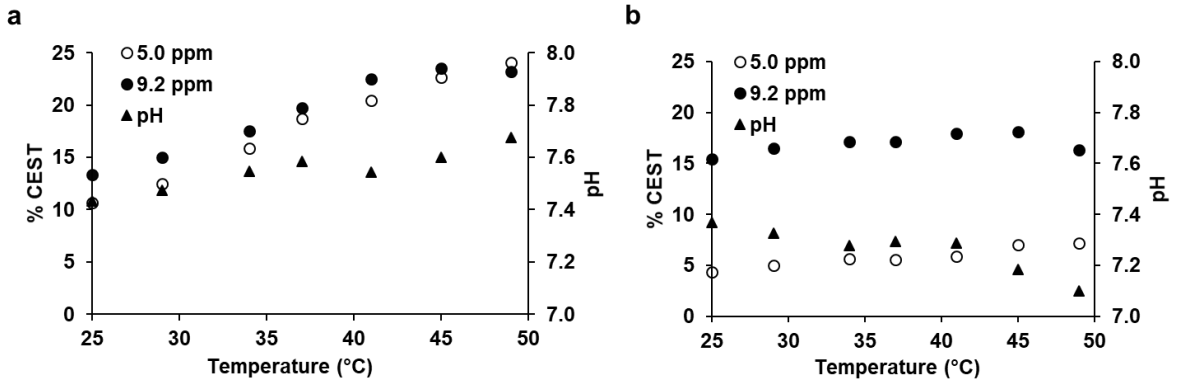

Figure 2.7. An evaluation of the temperature dependence of CEST effects. (a) A 20 mM monomer sample and (b) a 0.16 mM polymer sample were evaluated at 4 μT saturation power and 6 s saturation time. The open and filled circles pertain to the left-side y-axis that measures % CEST at 5.0 and 9.2 ppm, respectively. The filled triangles pertain to the right-side y-axis that represents pH that was determined from a ratio of the CEST signals.

We investigated how the concentration of each agent may affect pH measurements. CEST spectra were collected for the monomer agent between 1.25 and 40 mM, and for the polymer agent between 9.5 and 300 μM (Figure 2.8,2.9). The results indicate that each of the CEST signals were dependent on concentration, as expected. Unfortunately, the pH measurements with the monomer agent were dependent on the concentration of the agent, despite using a ratiometric approach that

should negate a concentration dependence. The monomer only measured pH values with some accuracy at high pH and at high concentration > 10 mM (Figure 2.8g,h). The monomer overestimated pH at high pH values when low concentrations ≤ 10 mM were used, and at all concentrations for low pH values (Figure 2.8e,f). Similarly, the pH measurements with the polymer agent also showed a dependence on the concentration of the agent. The polymer measured pH with some accuracy at high concentrations ≥ 20 μM (Figure 2.9). However, low concentrations of polymer overestimated low pH values and underestimated high pH values. The extracellular tumor microenvironment is expected to have low pH, and intravenous injections of highly concentrated solutions often deliver only low concentrations of agent to tumors (especially for polymer agents), indicating that the monomer and polymer agents may overestimate *in vivo* tumor pHe. This dependency of the pH measurement on the concentration of each agent suggests that the level of intermolecular hydrogen bonding between agents may be concentration-dependent, again showing that hydrogen bonding affects CEST.

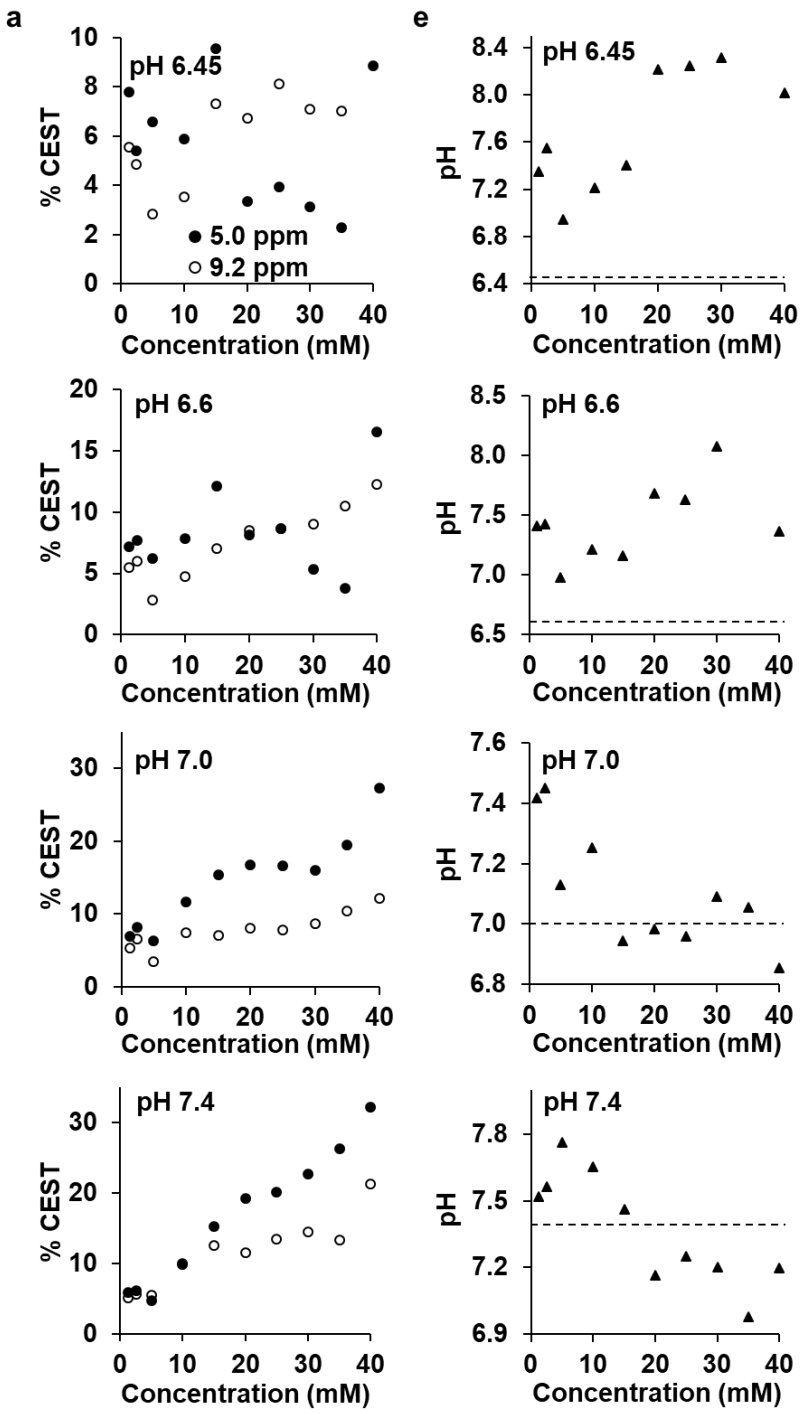

Figure 2.8. An evaluation of concentration dependence of the CEST effects of the monomer agent. Each graph is labeled with the pH of the sample. (a-d) % CEST was measured at 4 μT saturation power, 6 sec saturation time, and 37 °C. (e-h) The monomer agent showed a dependence on concentration. Horizontal dashed lines indicate the pH values measured with the benchtop pH meter.

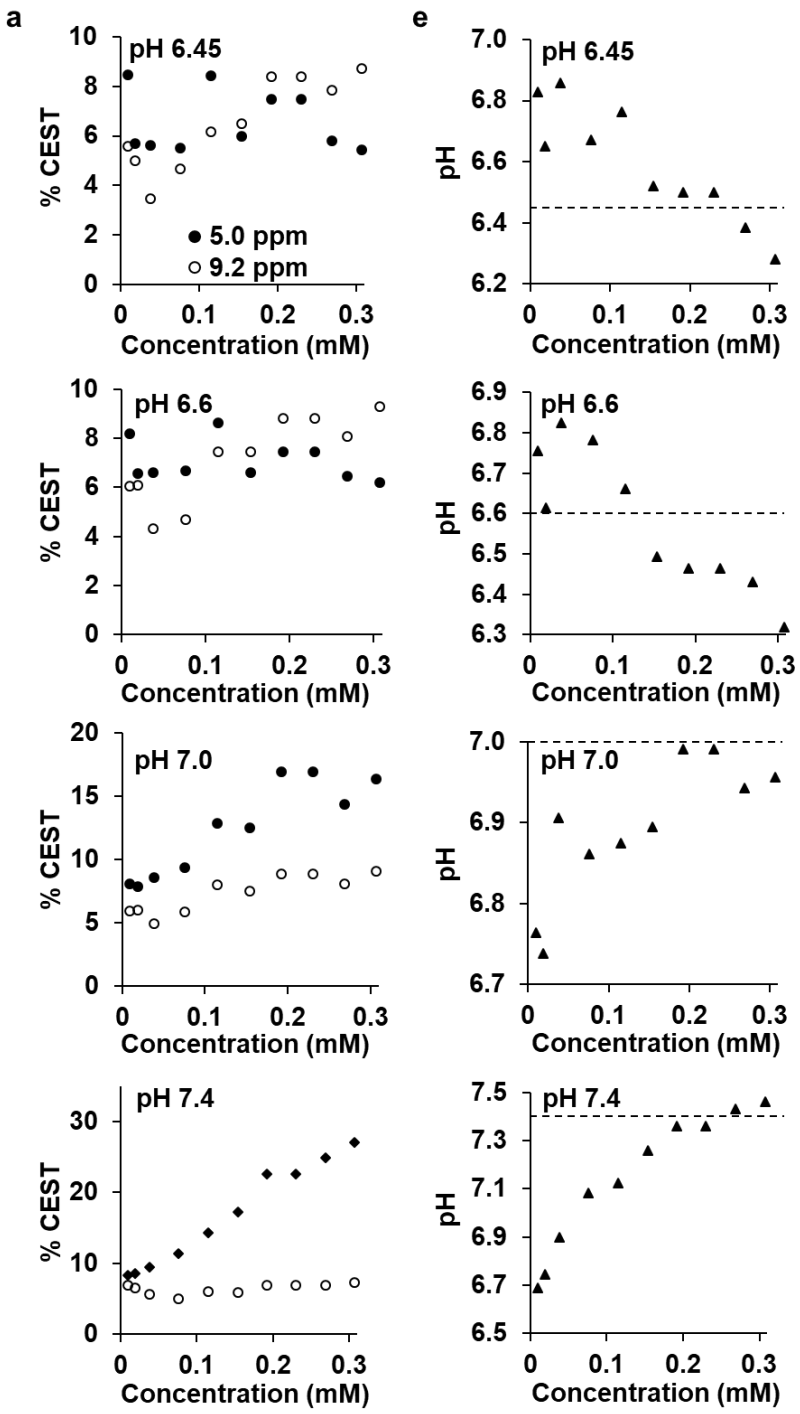

Figure 2.9. An evaluation of concentration dependence of the CEST effects of the polymer agent. Each graph is labeled with the pH of the sample. (a-d) % CEST was measured at 4 μT saturation power, 6 sec saturation time, and 37 °C. (e-h) The polymer agent showed a dependence on concentration. Horizontal dashed lines indicate the pH measured with the benchtop pH meter

2.3.6 *IN VITRO* CYTOTOXICITY OF THE CEST AGENTS

We used a standard MTT assay to analyze the cytotoxicity of each agent against MDA-MB-231 cells after 24 hours of exposure to concentrations ranging from 0.125 to 62.5 mM for the monomer agent and 1-500 μM for the polymer agent (which equates to 0.125 - 62.5 mM of monomeric units in the polymer, based on an average of 125 units per polymer). The results indicate that cell viability was >95% at concentrations as high as 1.25 mM and 10 μM for the monomer and polymer, respectively. The cell viability was >77% and >71% for the highest concentrations that were tested (Figure 2.10). These results demonstrate that the agents should be biocompatible for *in vivo* applications. Although more thorough safety studies will eventually need to be performed to evaluate the safety of each agent, this initial evaluation was sufficient to justify our subsequent *in vivo* acidoCEST MRI studies with each agent.

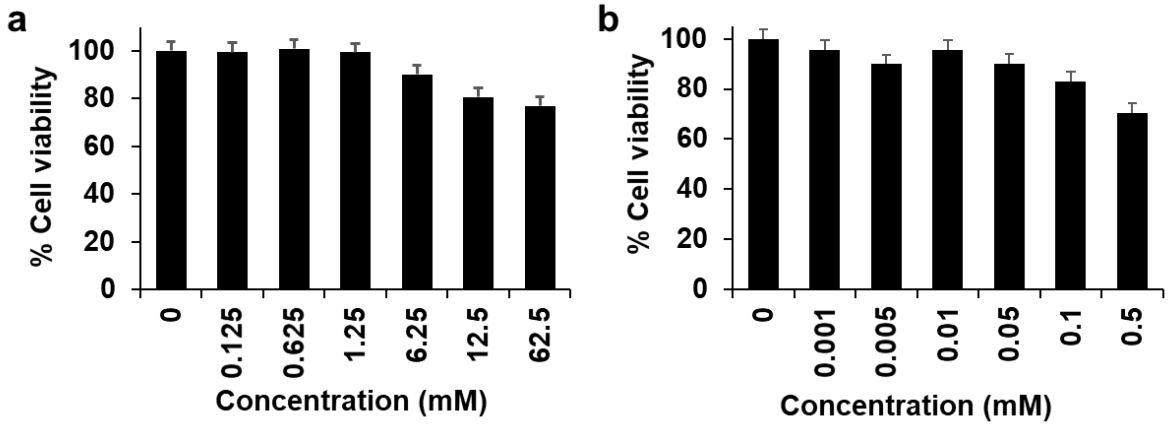

Figure 2.10. *In vitro* cytotoxicity of the monomer and polymer agents. Viabilities of MDA-MB-231 cells were evaluated after incubation with (a) the monomer agent and (b) the polymer agent.

2.3.7 *IN VIVO* ACIDOCEST MRI

The pHe of eight mice with a xenograft tumor of MDA-MB-231 breast cancer were scanned with acidoCEST MRI using iopamidol, monomer agent and polymer agent (Figure 2.11). Anatomical images of each mouse were used to localize the tumor (first column of Figure 2.11 and Figure A4-A6). Then we acquired CEST images before and after injection of each agent. We injected 7.8 mmol/kg of iopamidol, which we have used in our previous acidoCEST MRI studies [9,13-27]. We injected 2.0 and 0.016 mmol/kg of the monomer agent and the polymer agent, respectively. The polymer agent was injected at 125-fold and 488-fold lower concentrations than the monomer agent and iopamidol, respectively, which tested our objective of measuring tumor pHe with the delivery of a lower concentration of agent. Using a rudimentary assumption that the agent is equally distributed throughout the body, and assuming an average tissue density of 1 g/mL, these injections equate to 2.0 and 0.016 mM of the monomer and polymer agents, respectively. These roughly estimated concentrations are comparable to the concentrations that resulted in > 95% cell viability in our cytotoxicity tests (Figure 2.10), which justified injections at these concentrations. Furthermore, the solubility of the monomer agent was estimated to be approximately 300 mM. We injected in 200 μL of 250 mM monomer agent, which is below this solubility limit. The parametric maps of % CEST signal amplitude at 5.0 ppm (second column of Figure 2.11 and Figure A4-A6) and 9.2 ppm (third column of Figure 2.11 and Figure A4-A6) indicate good detection of both CEST effects throughout most of the tumor that was imaged. The pHe maps (fourth column of Figure 2.11 and Figure A4-A6) show colorful pixels where two significant CEST signals were measured and converted to pHe values.

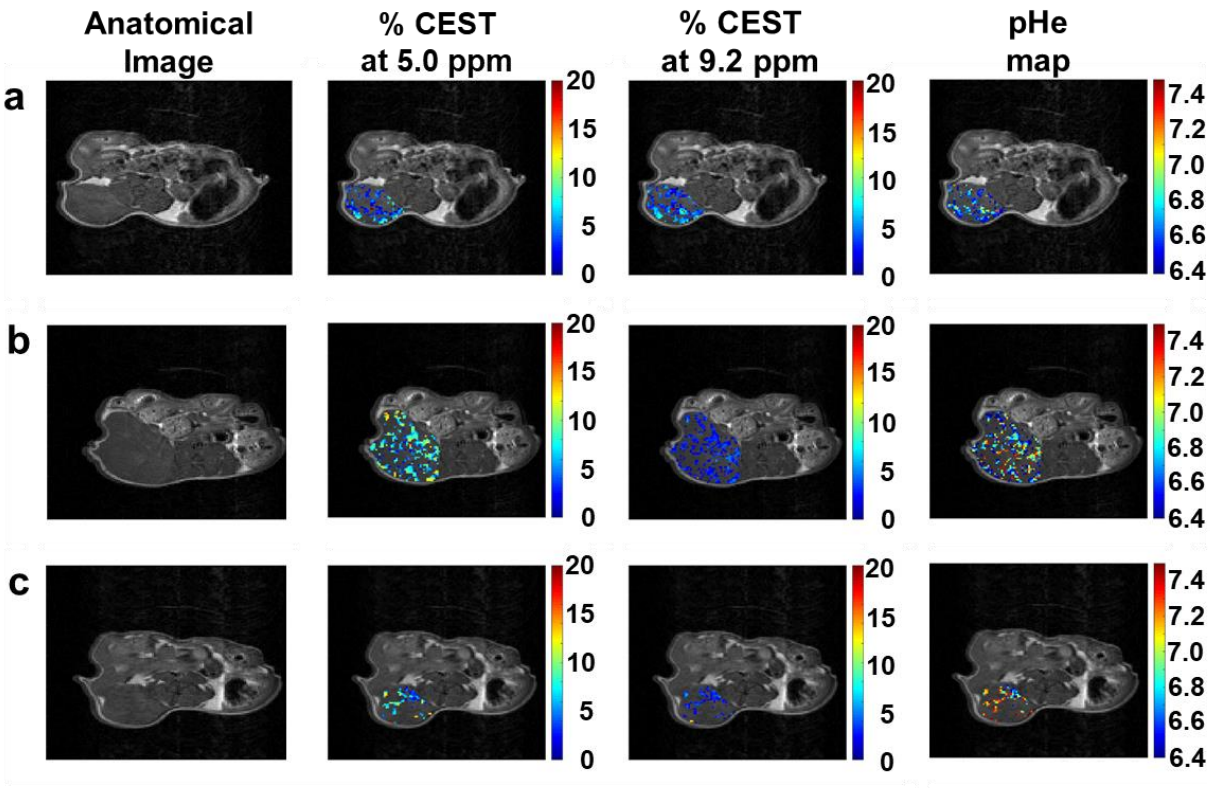

Figure 2.11. *In vivo* acidoCEST MRI. Images of a MDA-MB-231 tumor model following intravenous injection of 200 μL (a) 976 mM of iopamidol, (b) 250 mM of monomer agent, and (c) 2.0 mM of polymer agent (equivalent to 250 mM in monomer units). Anatomical images show the location of the tumor (first column). The parametric maps of % CEST signal amplitude at 5.0 ppm (second column) and 9.2 ppm (third column) demonstrate good detection of both CEST effects. The pHe maps (fourth column) show colorful pixels where two significant CEST contrast were measured and converted to pHe values.

The average tumor pHe of the tumor model measured with acidoCEST MRI using iopamidol was 6.33 ± 0.12 units (Figure 2.12). The consistent tumor pHe measured among the mice resulted in a low standard deviation, suggesting that acidoCEST MRI with iopamidol can perform precise evaluations of tumor acidosis. The average tumor pHe was measured to be 6.70 ± 0.15 and 6.85 ± 0.15 units with the monomer agent and polymer agent, respectively. Therefore, acidoCEST MRI overestimated tumor pHe with the monomer and polymer agents relative to

measurements made with iopamidol. This result is consistent with our studies of chemical solutions that evaluated the concentration dependence of pH measurements, which indicated that the monomer and polymer agents may overestimate tumor pHe if both the pHe and agent concentration in tumors were low.

The tumor pHe of two mice were analyzed with three sequential acidoCEST MRI scans that used each agent, while six mice were analyzed with only one acidoCEST MRI scan. The sequential scans produced similar average tumor pHe measurements for the mice that were sequentially scanned or scanned only one time (Figure 2.12). This result was expected, because iopamidol and the monomer agent are small molecules that should clear from *in vivo* tissues within one day. Therefore, acidoCEST MRI may be performed with sequential scans to monitor changes in tumor acidosis during tumor progression and during tumor response to treatment.

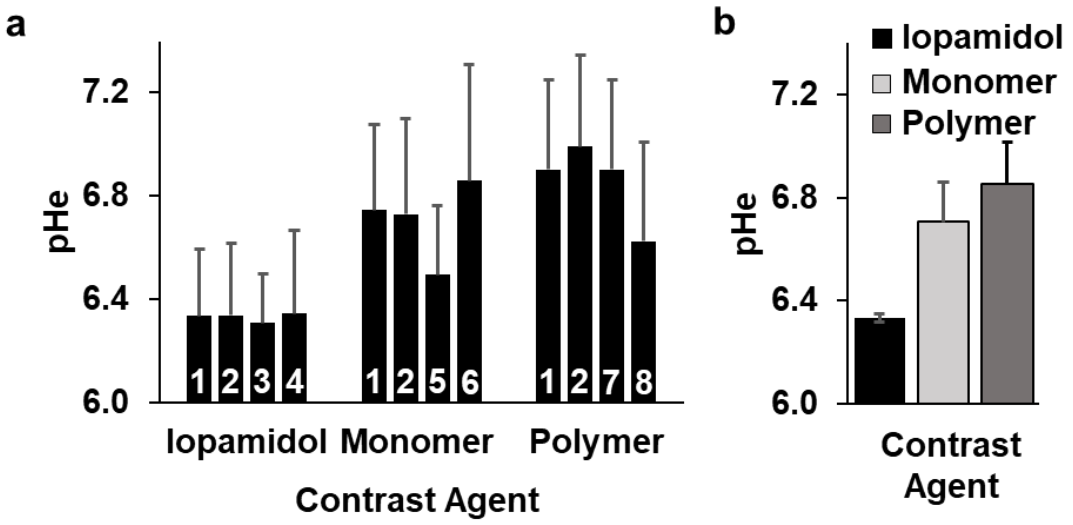

Figure 2.12. The results of the *In vivo* acidoCEST MRI studies. (a) AcidoCEST MRI was performed with iopamidol, the monomer agent and the polymer agent. Each bar is labeled with the mouse number. (b) A comparison of average tumor pH using each agent (n=4 for each bar).

2.4 CONCLUSIONS

We have developed a small molecule monomer agent and a nanoscale polymer agent for pH measurements with acidoCEST MRI. Optimized MRI conditions could detect CEST signals with a polymer agent that was 125-fold and 488-fold less concentrated than the monomer agent and iopamidol respectively, demonstrating an advantage of the nanoscale CEST agent. A ratiometric approach for correlating CEST with pH showed excellent linear relationships, although these correlations had different trends for the monomer and polymer, presumably due to hydrogen bonding and/or steric hindrance within the polymer. AcidoCEST MRI with the monomer and polymer agents could measure pH with a negligible dependence on temperature, but showed a dependence on concentration that caused pH to be overestimated in tumors with low pHe and typically low agent uptake. Indeed, *in vivo* acidoCEST MRI with both agents overestimated tumor pHe relative to similar measurements made with iopamidol. Therefore, our polymer agent demonstrated many of the attributes needed for improved acidoCEST MRI with a lower concentration of agent, but future developments of nanoscale polymer agents for acidoCEST MRI should focus on CEST agents that potentially avoid hydrogen bonding and steric hindrance.

CHAPTER 3

SIMULTANEOUS EVALUATIONS OF pH AND ENZYME ACTIVITY WITH A CEST MRI CONTRAST AGENT

3.1 INTRODUCTION

Solid tumors often have an extracellular tumor microenvironment as a consequence of upregulated glycolytic metabolism that produces excess lactic acid in tumors, known as the Warburg effect [1-3]. Therefore, extracellular tumor acidosis may be used as a biomarker to identify highly active metabolism in aggressive tumors, or a decrease in tumor metabolism in response to treatment [4-6]. In addition, solid tumors often have high protease activity in the extracellular tumor microenvironment, which causes degradation of the extracellular matrix surrounding tumor cells [7-9]. As a consequence, tumor cells can more easily invade into adjacent normal tissues and escape the primary tumor to cause metastasis in distant organs. For example, cathepsin B is a protease that is often upregulated in tumor cells and excreted into the extracellular microenvironment, which can cleave collagen and also cleave inactive pro-proteases to initiate a cascade of active proteases [10-13]. For this reason, the detection of the protease activity of cathepsin B or other proteases in tumors can also potentially impact cancer diagnoses.

3.1.1 SIMULTANEOUS DETECTION OF TUMOR pH AND ENZYME ACTIVITY

Although a single biomarker parameter can have merit for improving cancer diagnoses, different tumors often have diverse characteristics, and each individual tumor can often be heterogeneous, so that a single biomarker may have limited sensitivity or specificity during cancer diagnoses. A multi-biomarker, multi-parametric approach may have greater potential to improve evaluations of cancer or anti-cancer treatments. Simultaneous evaluations of tumor pHe and protease activity can provide a multi-parametric approach to characterizing the tumor microenvironment. Furthermore, tumor acidosis promotes secretion of proteases such as cathepsin B into the extracellular microenvironment [14], and some proteases including cathepsin B have a

greater catalytic efficiency in acidic conditions [15], so that the detection of high protease activity while also detecting an acidic microenvironment is synergistic [16].

3.1.2 A CEST AGENT THAT CAN DETECT pH AND ENZYME ACTIVITY SIMULTANEOUSLY

We sought to develop a MRI contrast agent that can simultaneously measure pH and detect protease activity, using a contrast mechanism known as Chemical Exchange Saturation Transfer (CEST) [17]. A common CEST agent has an aryl amide group (Figure 3.1a, shown in red). Selective radiofrequency saturation of the MR frequency of this aryl amide hydrogen causes the MR signal of this hydrogen to disappear (Figure 3.1a, top center). Subsequent chemical exchange of this hydrogen atom with a hydrogen on water transfers the saturation to water, which lowers the MR signal from the water (Figure 3.1a, top right). Standard MRI methods can then detect the MRI signal of the water to generate a CEST MR image. CEST MRI has evolved from chemical tests to *in vitro* experiments, to pre-clinical *in vivo* imaging studies, and more recently to clinical translation and clinical imaging trials, demonstrating that CEST MRI has become robust research field [18].

We have previously developed CEST agents that detect the catalytic activity of enzymes using a methodology known as catalyCEST MRI [19-31]. This method exploits the cleavage of an amide bond by a protease such as cathepsin B, which converts the aryl amide group to an aryl amine (Figure 3.1a, left side). This aryl amine cannot generate a detectable CEST effect, because the hydrogen atoms on the aryl amine exchange with water too quickly to allow for selective radiofrequency saturation. This loss of the CEST effect from the aryl amide can be used to detect cathepsin B activity, especially if the agent has a second exchangeable proton that can be detected as a control signal.

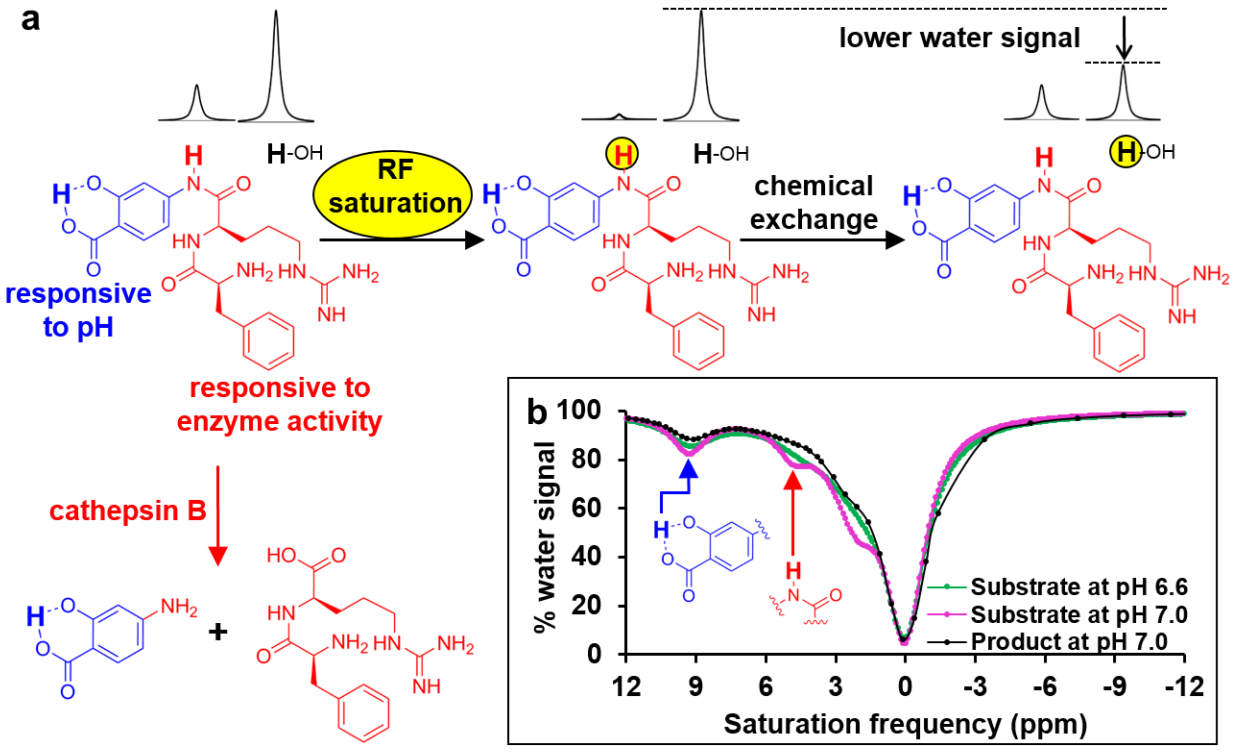

Figure 3.1. Chemical Exchange Saturation Transfer (CEST) MRI. a) The CEST mechanism relies on the different MR signals (shown as Lorentzian line shapes) for an amide proton and water proton (shown as large **H** letters). RF saturation applied at the MR frequency of the amide proton causes the MR signal from that proton to disappear. Subsequent chemical exchange of the amide and water protons transfers the saturation to water, reducing the water MR signal. The portion of the CEST agent in red is responsive to enzyme activity, because cleavage of the aryl amide bond causes the formation of an aryl amine (shown in red in the lower left), which does not generate a CEST effect. For comparison, the portion of the agent in blue has a salicylic acid moiety with a proton that can exchange with water, and can therefore generate a CEST effect, which is unresponsive to enzyme activity and is responsive to pH. b) Experimental CEST MRI at pH 6.6 and 7.0 before cleavage of the agent shows that the CEST signal at 9.2 ppm from the salicylic acid can generate a lower % water signal at higher pH. In addition, the experimental CEST spectra at pH 7.0 before after cleavage with cathepsin B shows the loss of CEST signal at 5.0 pm from the amide, while the CEST signal at 9.2 ppm from the salicylic acid remains.

We designed our hybrid CEST agent to include a salicylic acid moiety (Figure 3.1a, shown in blue), which remains after cathepsin B-catalyzed cleavage of the aryl amide, and therefore can serve as a control signal. For comparison, we and other investigators have developed enzyme-responsive CEST agents that have only one enzyme-responsive CEST signal [32-42]. These other agents have not included a second, enzyme-unresponsive control signal, which has complicated translation to *in vivo* studies.

We and other investigators have also previously developed CEST agents that measure pH using a methodology known as acidoCEST MRI [43-47]. For example, we have previously shown that the chemical exchange rate of a salicylic acid moiety is base-catalyzed and is therefore dependent on pH [29]. The amplitude of the CEST effect is dependent on the chemical exchange rate as well as the saturation power. This dependence on saturation power can be taken into consideration by measuring the CEST signal at two saturation powers, and using a ratio involving these two CEST signals to determine pH [48-52]. Therefore, a salicylic acid moiety can potentially measure pH with a dual-power acidoCEST MRI method. Our report describes the development of a hybrid CEST agent, and the evaluation of this agent during acidoCEST and catalyCEST MRI studies.

3.2 MATERIALS AND METHOD

3.2.1 MATERIALS

Dry solvents were purchased and used without further purification or drying treatment. Protected L-amino acids were used for this synthesis. ACS grade solvents for chromatography, $NaHCO_3$, Na_2SO_4, and PBS buffer (pH 7) were purchased from Fisher Scientific (part of Thermo Fisher Scientific, Waltham, MA, USA). Dithiothreitol (DTT), 4-amino-2-hydroxybenzoic acid,

KOtBu, conc. HCl, Pd/C, $Pd(OH)_2/C$, EDC.HCl, benzyl bromide, di-tert-butyl dicarbonate, and 4M HCl in dioxane were purchased from Sigma-Aldrich (St. Louis, MO, USA). Anhydrous THF and DMF were purchased from Acros Organics (part of Thermo Fisher Scientific, Waltham, MA, USA). Z-Phe-OH, $HOBt.H_2O$, and NMM were purchased from Advanced Chem Tech (Louisville, KY, USA). Hydroxybenzotriazole (HOBt) was purchased from Anaspec, Inc. (Fremont, CA, USA). HPLC grade acetonitrile was purchased from EMD Millipore, Inc. (Billerica, MA, USA). Boc-Arg$(Z)_2$-OH was purchased from Chem Impex Intl., Inc. (Wood Dale, IL, USA). Cathepsin B enzyme was purchased from Bon-Opus Biosciences (Millburn, NJ, USA)

NMR spectroscopy was performed with a 600 MHz NMR spectrometer (Bruker Biospin, Corp., Billerica, MA, USA). A Luna C18 5 µm preparative column (Phenomenex, Torrance, CA, USA) with 21.2 × 250 mm dimensions was used for preparatory scale HPLC. LC-MS studies were conducted using a Waters Acquity™ UPLC-MS system with an Acquity UPLC® BEH C-18 1.7 µm, column with dimensions of 2.1 mm × 50 mm, using UV detection between 200 and 400 nm with a 2996 PDA detector, and a TQ detector mass spectrometer with electrospray ionization (ESI).

3.2.2 CHEMICAL SYNTHESIS

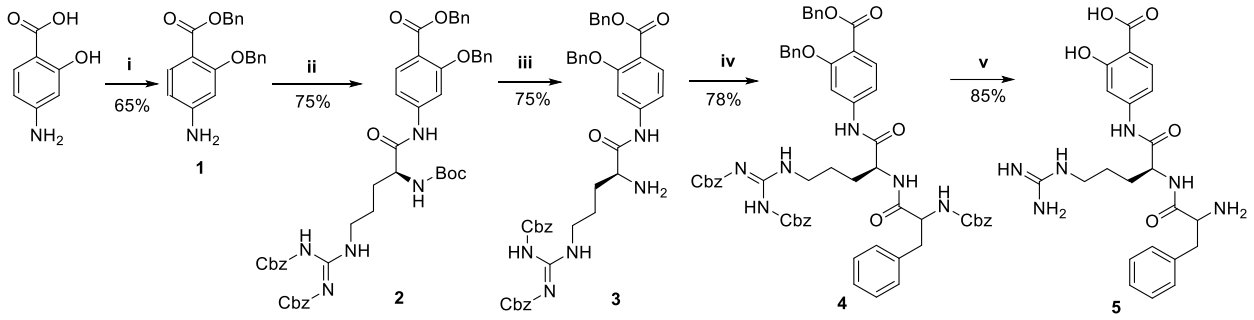

Scheme 3.1. Chemical synthesis of the hybrid CEST agent. (i)BnBr, KOtBu, DMF, 0° C to RT, overnight; (ii) Boc-Arg(Z)$_2$OH, anhy. pyridine, Boc$_2$O,dry THF, RT, overnight; (iii) 4 M HCl in dioxane, 0° C to RT, 15 min; (iv) Z-Phe-OH, HOBt.H$_2$O, NMM, EDC.HCl, 0° C to RT; (v) Pd/C, Pd(OH$_2$), MeOH:ethyl acetate (1:1), conc. HCl, H$_2$, 10 h.

3.2.2.1 SYNTHESIS OF COMPOUND 1 [53]

4-aminosalicylic acid (4.5 g, 29.3 mmol) and potassium tert-butoxide (3.62 g, 32.3 mmol) were dissolved in anhydrous DMF (20 mL) under argon at room temperature. The reaction mixture was cooled to 0 ºC with vigorous stirring. Then, benzyl bromide (3.8 mL, 32.3 mmol) in DMF (35 mL) was added to the reaction mixture dropwise over 30 min. After stirring for 4 hours, a second portion of potassium tert-butoxide (3.62 g, 32.3 mmol) and benzyl bromide (3.8 mL, 32.3 mmol) in DMF (35 mL) were added at 0 ºC as described above. The reaction was allowed to stir for 16 h and was then quenched with an equal amount of water, extracted with ethyl acetate for three times. The organic layer was washed with water three times, then washed with brine three times and dried with anhydrous sodium sulfate. The solvent was removed with a rotary evaporator and purified by column chromatography using ethyl acetate: hexanes (10% to 40%) to obtain a white solid (yield: 6.35 g, 65%). ^{1}H NMR (600 MHz, chloroform-*d*) δ 7.86 – 7.76 (m, 1H), 7.50 – 7.42 (m, 2H), 7.42

– 7.36 (m, 2H), 7.36 – 7.26 (m, 6H), 6.25 (dd, *J* = 6.5, 2.4 Hz, 2H), 5.30 (s, 2H), 5.12 (s, 2H), 4.00 (s, 2H).

3.2.2.2 SYNTHESIS OF COMPOUND 2

Boc-L-dibenzyloxycarbonyl arginine (6.6 g, 12.4 mmol) was dissolved in anhydrous THF (40 mL) under argon at room temperature. Anhydrous pyridine (1 mL, 12.4 mmol) was added, followed by addition of Boc-anhydride (2.7 g, 12.4 mmol). After stirring at room temperature for 1 h, compound **1** (2.0 g, 6.2 mmol) was added to the reaction flask and then allowed to stir for another 16 h. The reaction mixture was diluted with ethyl acetate (100 mL) and washed with saturated sodium bicarbonate (15 mL) followed by 1 M hydrochloric acid (15 mL), water (15 mL), and brine (15 mL). The organic layer was dried over anhydrous sodium sulfate, and the solvent was removed and purified by column chromatography using ethyl acetate and hexanes (2% to 45%). Compound **2** was obtained as a pale yellow solid (3.99 g, 75% yield). ^{1}H NMR (600 MHz, Chloroform-*d*) δ 9.40 (d, *J* = 81.3 Hz, 2H), 8.71 (s, 1H), 7.73 (d, *J* = 8.5 Hz, 1H), 7.57 (s, 1H), 7.48 – 7.18 (m, 20H), 6.51 (d, *J* = 8.7 Hz, 1H), 5.85 (s, 1H), 5.58 – 4.74 (m, 8H), 4.42 (s, 1H), 4.10 – 3.81 (m, 2H), 1.83 (ddt, *J* = 22.5, 11.2, 6.7 Hz, 4H), 1.44 (s, 9H). The final compound was analyzed by LC-MS (RP C-18, 10-90% water: acetonitrile 0.1% formic acid, 0.5 mL/min), in 3 min, Rt = 2.7 min) HRMS-ESI (m/z): $[M+H]^+$ calc'd for $[C_{48}H_{51}N_5O_{10}]$, 858.3714; found, 858.7674.

3.2.2.3 SYNTHESIS OF COMPOUND 3

4 M HCl in dioxane (7 mL, 28 mmol) was cooled to 0 ºC using an ice bath under argon. Compound **2** (1 g, 1.16 mmol) was added to the cooled reaction flask while stirring. Then the ice bath was removed and stirred at room temperature for 15 min. The solvent was removed with

rotary evaporation at 15 ºC. The residue was re-dissolved in ethyl acetate (40 mL). The organic layer was washed with water (50 mL) and then washed with brine (50 mL), and dried over anhydrous sodium sulfate. The solvent was then removed under reduced pressure, the product was purified by column chromatography (0-7% methanol:dichloromethane), and the final residue was lyophilized to yield the dry compound **3** as a colorless solid (yield: 0.66 g, 75%). ^{1}H NMR (600 MHz, DMSO-d_6) δ 10.68 (s, 1H), 9.15 (s, 2H), 8.31 (s, 2H), 7.79 (d, J = 8.3 Hz, 1H), 7.55 (s, 1H), 7.49 – 7.21 (m, 20H), 5.36 – 4.96 (m, 8H), 3.99 – 3.77 (m, 3H), 1.74 (d, J = 81.7 Hz, 4H). The final compound was analyzed by LC-MS (RP C-18, 10-90% water: acetonitrile 0.1% formic acid, 0.5 mL/min), in 3 min, Rt = 1.9 min) HRMS-ESI (m/z): $[M+H]^+$ calc'd for [$C_{43}H_{44}N_5O_8$], 758.3190; found, 758.5768.

3.2.2.4 SYNTHESIS OF COMPOUND 4

Compound **3** (0.15 g, 0.198 mmol) was dissolved in DMF (4 mL). Z-Phe-OH (0.062 g, 0.208 mmol) was added followed by the addition of HOBt.H_2O (3 mg, 0.0198 mmol) and NMM (23 μL, 0.208 mmol). The reaction mixture was cooled to 0 ºC, EDC.HCl was added, and the ice bath was removed. The reaction was stirred at room temperature until all the starting material are gone (1 hr). Cold water (10 mL) was added to the reaction mixture, and a white suspension formed. The solution was diluted with ethyl acetate, the organic layer was intensively washed with water to remove the DMF, and then washed with brine. The organic layer was dried with anhydrous sodium sulfate, the solvent was removed under reduced pressure, and the product was purified column chromatography (20-40% ethyl acetate:hexanes) to obtain the final compound as a white powder (yield: 0.161 g, 78%). The final compound was analyzed by LC-MS (RP C-18, 10-90% water: acetonitrile 0.1% formic acid, 0.5 mL/min), in 3 min, Rt = 2.9 min) HRMS-ESI (m/z): $[M+H]^+$ calc'd for [$C_{60}H_{59}N_6O_{11}$], 1039.4242; found, 1039.9100.

3.2.2.5 SYNTHESIS OF COMPOUND 5

Methanol and ethyl acetate (1:1) (10 mL) were added to the mixture of compound **4** (0.10 g, 0.096 mmol), with catalytic amounts of Pd/C (10% w/w) and $Pd(OH)_2$ (10% w/w), and then one drop of concentrated HCl was added. The reaction flask was equipped with a balloon filled with H_2. The reaction mixture was allowed to stir overnight under H_2. Then the reaction mixture was passed through a celite pad and then the solvent was removed under reduced pressure. The final product was purified by preparative HPLC (0-30% acetonitrile:water (with 0.1% trifluoroacetic acid) and compound **5** was obtained as a white solid after lyophilization (0.037 g, 85%). The final compound was analyzed by LC-MS (RP C-18, 5-95% water: acetonitrile 0.1% formic acid, 0.5 mL/min), in 5 min, Rt = 1 min). HRMS-ESI (m/z): $[M+H]^+$ calc'd for $[C_{22}H_{29}N_6O_5]$, 457.2199; found, 456.9262.

3.2.3 ACIDOCEST MRI OF CHEMICAL SAMPLES

The substrate (compound 5) and product (4-aminosalicylic acid) were prepared at 20 mM concentration in 10 mM PBS. The pH was adjusted using a benchtop pH meter and very small volumes of HCl and NaOH that did not significantly affect agent concentrations (Mettler Toledo Seven compact S220 pH meter, Columbus, OH). Samples were placed in a customized holder (Figure 3.2a) that maintained the samples at 37.0 ± 0.2 °C. Our customized sample holder was filled with 2% agarose to reduce B_1 and B_0 inhomogeneities. We incubated our samples and holder at the desired temperature for 4-18 hours prior to each MRI study. We used warm air and an automated temperature feedback system to maintain temperature in the MRI magnet (SA Instruments, Stony Brook, NY). We validated our sample temperatures by using the same holder to analyze samples of ethylene glycol, and using localized MR spectroscopy to validate

temperature, which is an ideal method for measuring the temperature of chemical solutions without disturbing the solutions in the MRI magnet [54].

MRI studies were performed with a Bruker Biospec MRI scanner operating at 7 Tesla (T; 300 MHz) magnetic field strength with a 72 mm volume transceiver coil (Bruker Biospin, Inc.,Billerica, MA). To identify the location of the samples in the magnet, an initial set of images were acquired using a multislice spin echo MRI protocol with the following parameters: 600 ms repetition time (TR); 8 ms echo time (TE); 180° excitation flip angle (FA); coronal image orientation; 64×64 matrix; 8×8 cm field-of-view (FOV); 1.25 $\times$ 1.25 mm in-plane spatial resolution; 1 mm slice thickness (SL); 40 slices; 1 average; 38 s total scan time.

To perform CEST MRI studies, we used a fast imaging with steady-state free precession (FISP) MRI protocol that was modified to perform CEST-FISP MR image acquisitions [55], with the following parameters: 4.59 ms TR; 2.295 ms TE; 30° FA; centric encoding; coronal image orientation; 256×256 matrix; 8×8 cm FOV; 0.3125×0.3125 mm in-plane spatial resolution; 1 mm SL; 1 slice; and 1 average. We acquired CEST images with selective saturation applied at 4 μT power for 5 s at saturation frequencies in 0.1 ppm increments from -13 ppm to 13 ppm, for a total scan time of 28.0 minutes. We also acquired CEST MR images at 1 μT power to evaluate the dual-power acidoCEST MRI method with our hybrid agent.

3.2.4 CATALYCEST MRI OF CHEMICAL SAMPLES

CatalyCEST MRI was performed with substrate concentrations ranging from 10 mM to 40 mM at pH 6.6, 6.8, 7.0 and 7.4. These samples were prepared in 10 mM PBS with a 200 μL volume, and the pH was measured using a benchtop pH meter (Mettler Toledo, Inc., Columbus, OH). The samples were then placed in our customized holder with agarose for high-throughput MRI studies

with good B1 and B0 homogeneities across the samples. We maintained our samples at 37 ºC as described above.

To identify the location of the samples in the magnet, an initial set of images were acquired using a multislice spin echo MRI protocol with the following parameters: 600 ms repetition time (TR); 8 ms echo time (TE); 180° excitation flip angle (FA); coronal image orientation; 64 × 64 matrix; 8 × 8 cm field-of-view (FOV); 1.25 × 1.25 mm in-plane spatial resolution; 1 mm slice thickness (SL); 40 slices; 1 average; 38 s total scan time. The kinetics of the substrate cleavage by cathepsin B enzyme was studied using catalyCEST MRI [20] with the CEST-FISP MRI protocol that used the following parameters: 3.31 ms TR; 1.655 ms TE; 30° FA; centric encoding; coronal image orientation; 128 × 128 matrix; 8 × 8 cm FOV; 0.625 × 0.625 mm in-plane spatial resolution; 2 mm slice thickness; 1 slice; and 1 average, using a saturation pulse of 4 μT and 5 s saturation time. Selective saturation was applied using a continuous wave pulse at 4 μT power for 5 s with 58 frequencies ranging from 15 to -15 ppm. The time to acquire a CEST image at one saturation frequency was 5.454 s. The time to acquire one set of 58 CEST images was 5:16 min.

One CEST spectrum was acquired before adding the enzyme. We then added DTT (0.85 μL, 4 mM) and cathepsin B enzyme (2.5 μL, 131 nM) to the samples. We acquired a series of 60 CEST MR image sets for 5.26 hours to monitor the enzyme kinetics. The initial rate of each reaction, also known as the initial velocity or v_i, was determined from data acquired within the first hour of the reaction. A Lineweaver-Burk plot was used to determine the Michaelis constant, K_M, and the reaction velocity, V_{max}. The catalytic turnover rate, k_{cat}, was determined from V_{max} and the initial enzyme concentration. The catalytic efficiency, k_{cat}/K_M was also determined. In addition, a LB-concentration analysis method (also known as the Omega Plot method) was used to generate a calibration curve that relates CEST signal with concentration, which was required for

converting % CEST signals to substrate concentrations for Michaelis-Menten enzyme kinetics studies [56,57].

3.2.5 ANALYSIS OF CEST SPECTRA

Images were processed using ParaVision v5.1 (Bruker Biospin, Inc., Billerica, MA), and CEST MR image analyses were performed with Matlab 2018b (The MathWorks, Inc., Natick, MA). To measure CEST signal amplitudes from the substrate agent, each CEST spectrum from a region of interest (ROI) was analyzed by fitting the spectrum to a sum of four Lorentzian line shapes to account for three CEST signals (2.5, 5.0 and 9.2 ppm) and direct saturation of water [58]. CEST signal amplitudes from the product were measured by fitting CEST spectra with a sum of two Lorentzian line shapes to account for one CEST signal (9.2 ppm) and direct saturation of water. The center, width, and amplitude of each Lorentzian line were allowed to change in order to obtain an optimal fit.

3.2.6 LC-MS ENZYME KINETICS ASSAY

Michalis-Menton kinetics studies were performed using LC-MS in an attempt to validate catalyCEST results. The substrate was prepared at pH 6.6, 6.8, 7.0 and 7.4 in 200 μL, with substrate concentrations of 10, 15, 20, 30, and 40 mM for each pH value. DTT (0.85 μL, 4 mM) and cathepsin B enzyme (2.5 μL, 131 nM) were added to each solution, and the solution was incubated at 37 °C. Then 1 μL aliquots were withdrawn every 6 minutes for LC-MS analysis (Solvent gradient: 0-15% acetonitrile: water with 0.1% formic acid, Waters Acquity™ UPLC-MS system with Acquity UPLC® BEH C-18 1.7 μm, 2.1 mm × 50 mm column). We used an electrospray ionization (ESI) method to detect a dimer of the 4-amino salicylic acid product (m/z: 156 for the monomer, 312 for the dimer), and also to detect the substrate (m/z: 456). Michaelis-Menten

kinetics were then analyzed using the same procedure described above, using the LC chromatogram to estimate concentrations of the substrate.

3.3 RESULTS

3.3.1 SYNTHESIS AND INITIAL CEST MRI CHARACTERIZATION

The hybrid CEST agent was synthesized in five steps with a 24% overall yield (Scheme 3.1). The final purified product was validated with mass spectrometry (Figure A12). We performed CEST MRI studies that recorded the decrease in % water signal as a function of saturation frequency, known as a Z-spectrum (Figures 3.1, 3.2c-f). The Z-spectrum showed that the agent had two CEST signals at 5.0 and 9.2 ppm, which were assigned to the aryl amide and salicylic acid moieties, respectively, based on results from similar CEST MRI agents [24-30]. The Z-spectrum also showed a CEST signal at 2.5 ppm that was assigned to the guanidinium group of the agent, which also matched results from similar CEST agents. The CEST signal at 9.2 ppm was stronger in the spectrum recorded at higher pH 7.0 relative to lower pH 6.6, indicating that the CEST of salicylic acid is pH-dependent as expected. After incubating the agent with cathepsin B, the CEST signal at 5.0 ppm disappeared, indicating that the protease had cleaved the amide bond to form an aryl amine in the product. This product, 4-aminosalicylic acid, was further confirmed with mass spectrometry. Therefore, the agent was also responsive to enzyme activity as well as pH, demonstrating that the design of our hybrid CEST agent was successful.

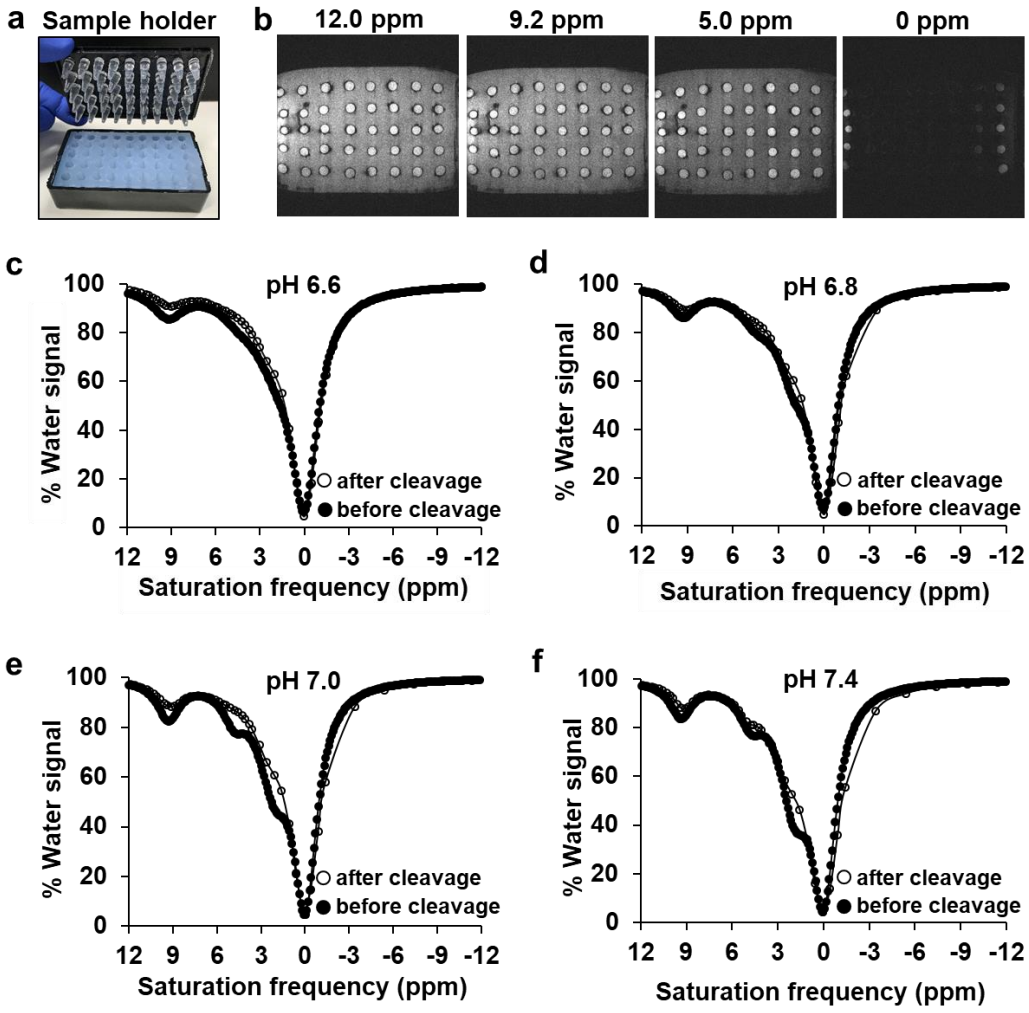

Figure 3.2. CatalyCEST MRI. (a) The samples were placed in a MRI-compatible sample holder filled with agarose to reduce B1 and B0 inhomogeneities. (b) CEST MR images of the samples and holder showed excellent image homogeneity. Samples were only placed in the central six columns of the holder, and tubes in the columns along the left and right edges contained only water. Images were acquired with 4 μT of saturation applied for 5 s with samples maintained at 37 °C. Selective saturation at 12.0, 9.2, 5.0, and 0 ppm produced images that showed relative differences in % water signal. These % water signals were plotted relative to saturation frequency to generate Z-spectra that were acquired at (c) pH 6.6, (d) pH 6.8, (e) pH 7.0 and (f) pH 7.4, and before and after cleavage of the substrate agent with cathepsin B. Z-spectra acquired before protease-catalyzed cleavage showed three signals at 2.5 pm, 5.0 ppm and 9.2 ppm. Z-spectra spectra acquired after cleavage showed a decrease in CEST signal at 5.0 ppm, while the CEST signal at 9.2 ppm remained.

3.3.2 DUAL-POWER ACIDOCEST MRI STUDIES

We used a dual-power acidoCEST MRI approach to correlate pH with the CEST signal of the agent's salicylic acid moiety at 9.2 ppm. This approach records two Z-spectra at different saturation powers, then measures the CEST signal at each power, and calculates a ratio of the two CEST signals over a range of pH values (Figure 3.3a). When measured with 4 μT saturation power, this CEST signal at 9.2 ppm monotonically increased with increasing pH from approximately pH 6.4 to 7.2. For comparison, using 1 μT saturation power caused this measured CEST signal to be relatively constant. The ratiometric evaluation of the CEST signals at each saturation power for this agent was linearly correlated with pH between 6.4 and 7.3 pH units (Figure 3.3c). We measured similar CEST signals from the post-cleavage product at 1 and 4 μT saturation powers (Figure 3.3b), which resulted in a ratio that was also linearly correlated with pH (Figure 3.3d).

The slopes and y-intercepts of these linear correlations with pH were different for the pre-cleaved substrate agent and the post-cleaved product, indicating that the amide bond cleavage affected the chemical exchange rate of the salicylic acid. Therefore, the ratio of substrate agent and product must be known to use a weighted average of Figures 3.3c and 3.3d to measure pH. Fortunately, the initial enzyme-catalyzed cleavage of the substrate agent can be negligible, because enzyme concentration is very low relative to the high concentration of substrate agent that is used during CEST MRI studies. Therefore, the CEST-pH calibration in Figure 3.3 can be used to initially measure pH with the substrate agent.

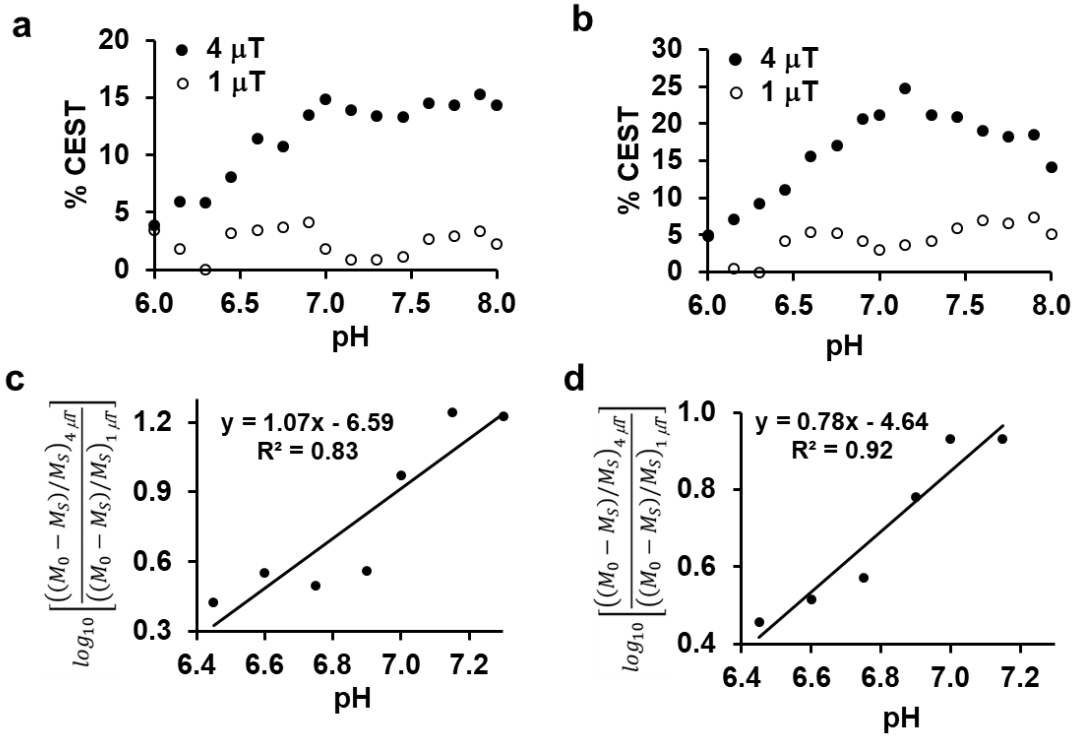

Figure 3.3. Dual power acidoCEST MRI. Selective saturation of the salicylic acid proton of the agent can generate % CEST signal for (a) the substrate and (b) the product with 1 μT and 4 μT saturation powers. A $\log_{10}$ ratio using these CEST signals is linearly correlated with pH between pH 6.4-7.3 for (c) the substrate and (d) the product. Samples were evaluated at 37 °C, with CEST performed with a 5 s saturation time using a 7T MRI instrument.

3.3.3 ENZYME KINETICS STUDIES

We then performed Michaelis-Menten enzyme kinetics studies using a catalyCEST MRI approach. Z-spectra were continuously acquired after adding cathepsin B to samples of substrate agent that ranged from 10 to 40 mM, and which ranged from pH 6.6 to 7.4 (Figure 3.4). In a separate experiment, we correlated the concentration of the substrate agent with the agent's CEST signal at 5.0 ppm using a LB-concentration analysis method (Figure 3.5). This CEST-concentration correlation was then used to convert the temporally disappearing CEST signal to a temporally decreasing concentration of substrate agent (Figure 3.6).

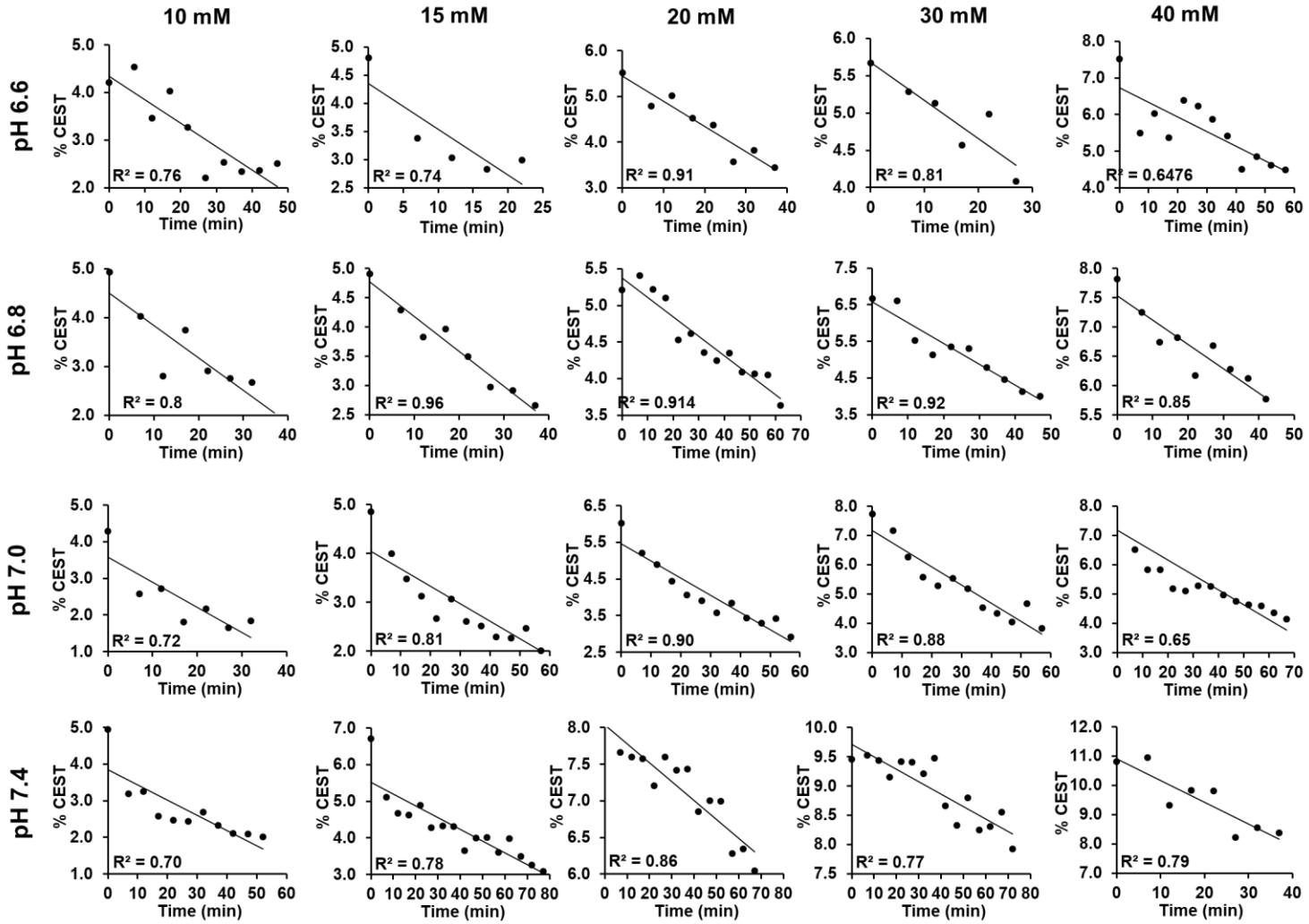

Figure 3.4. Monitoring enzyme cleavage with catalyCEST MRI. The % CEST signal at 5.0 ppm was monitored during cleavage of the substrate agent with cathepsin B at pH 6.6, 6.8, 7.0 and 7.4 using initial substrate concentrations of 10, 15, 20, 30, and 40 mM. CEST spectra were continuously acquired with 4 μT of saturation applied for 5 s at 37 °C.

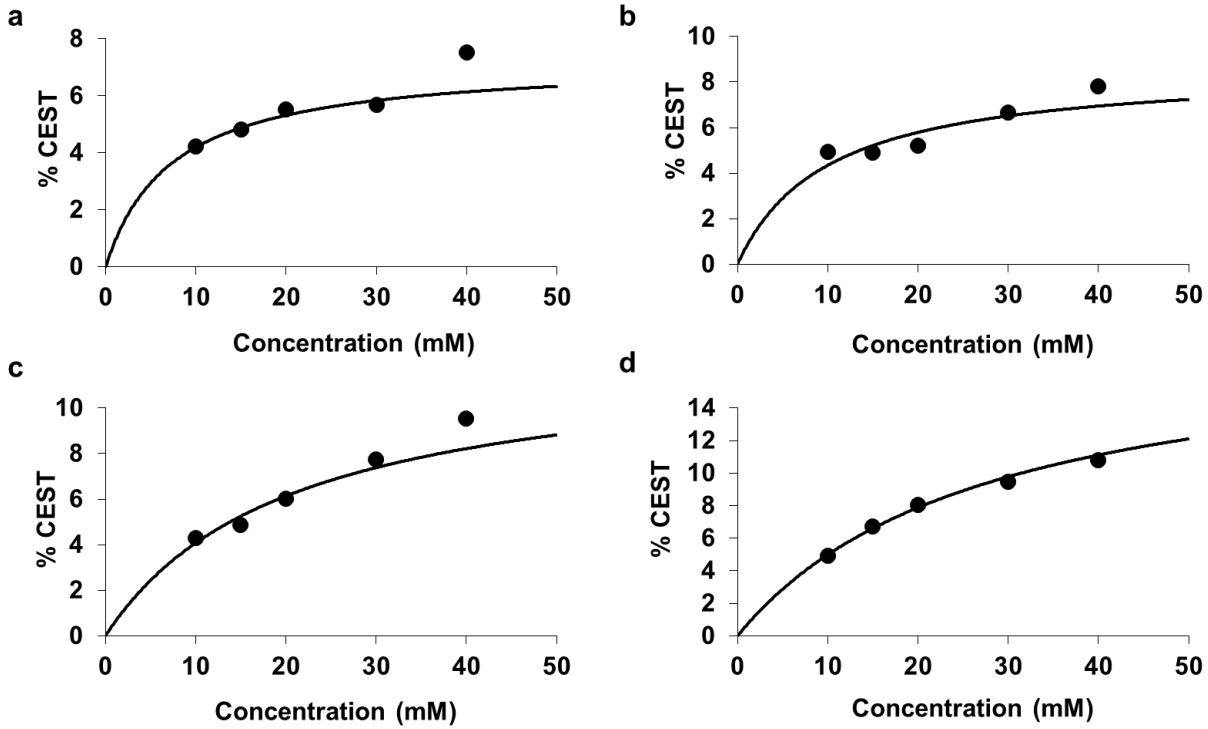

Figure 3.5. The dependence of % CEST on concentration of the agent. The % CEST signal at 5.0 ppm of the substrate was analyzed at (a) pH 6.6, (b) pH 6.8, (c) pH 7.0, and (d) pH 7.4. The solid curved lines show the analysis of the CEST-concentration relationship with the LB-conc analysis method.

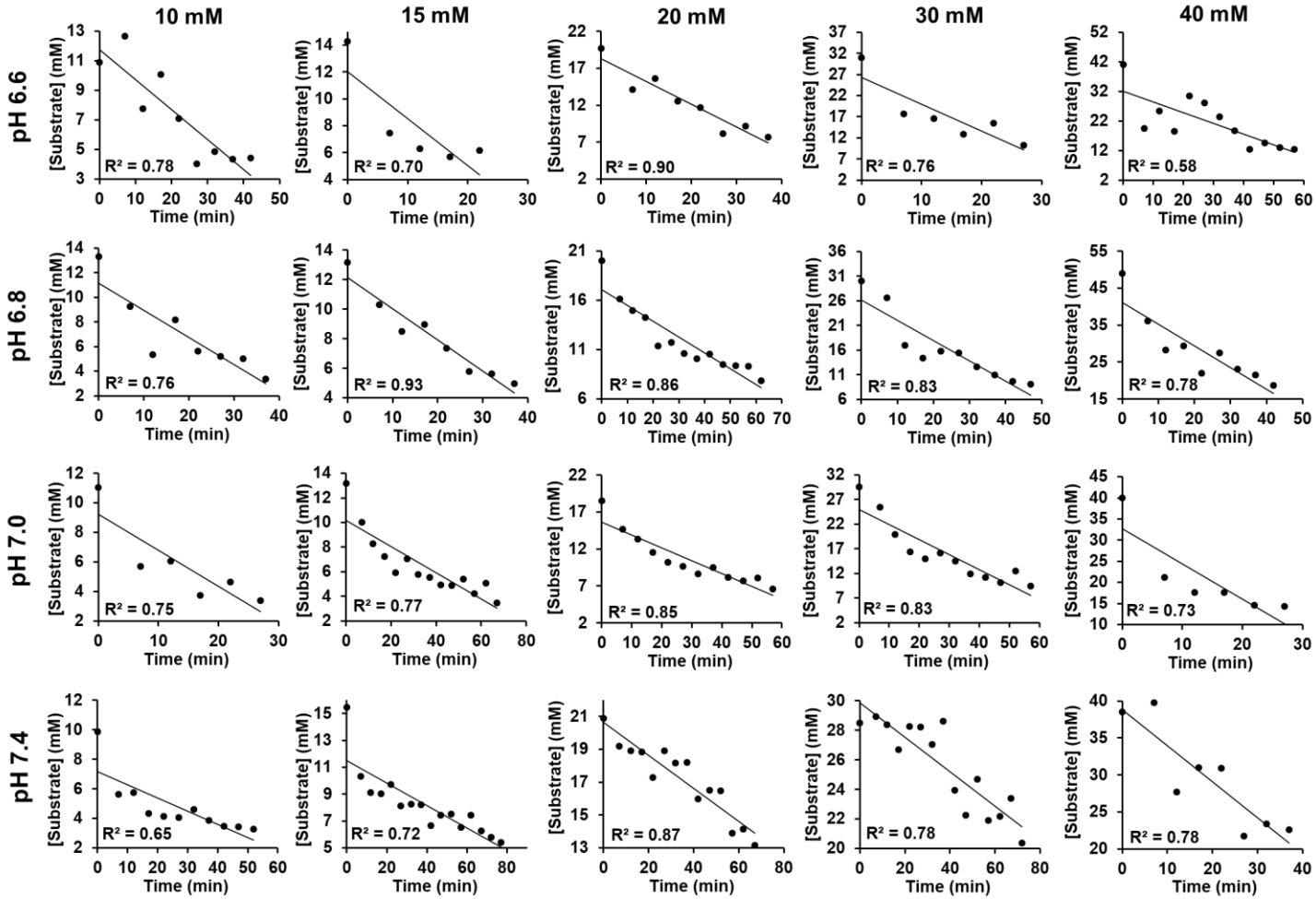

Figure 3.6. Initial velocities of enzyme cleavage as measured with catalyCEST MRI. The results in Figure 3.4 were converted from % CEST signal at 5.0 ppm to substrate concentrations using the calibrations shown in Figure 3.5. As with Figure 3.4, the substrate agent was treated with cathepsin B at pH 6.6, 6.8, 7.0 and 7.4 using initial substrate concentrations of 10, 15, 20, 30, and 40 mM. CEST spectra were continuously acquired with 4 μT of saturation applied for 5 s at 37 °C.

The slope of this temporal decrease in substrate concentration was used to determine the initial rate (also known as initial velocity) of each reaction at different initial substrate concentrations and different pH values. These initial rates were then used to construct Lineweaver-Burke plots (Figure 3.7) that were used to measure Michaelis-Menten kinetics parameters at each pH condition (Table 3.1).

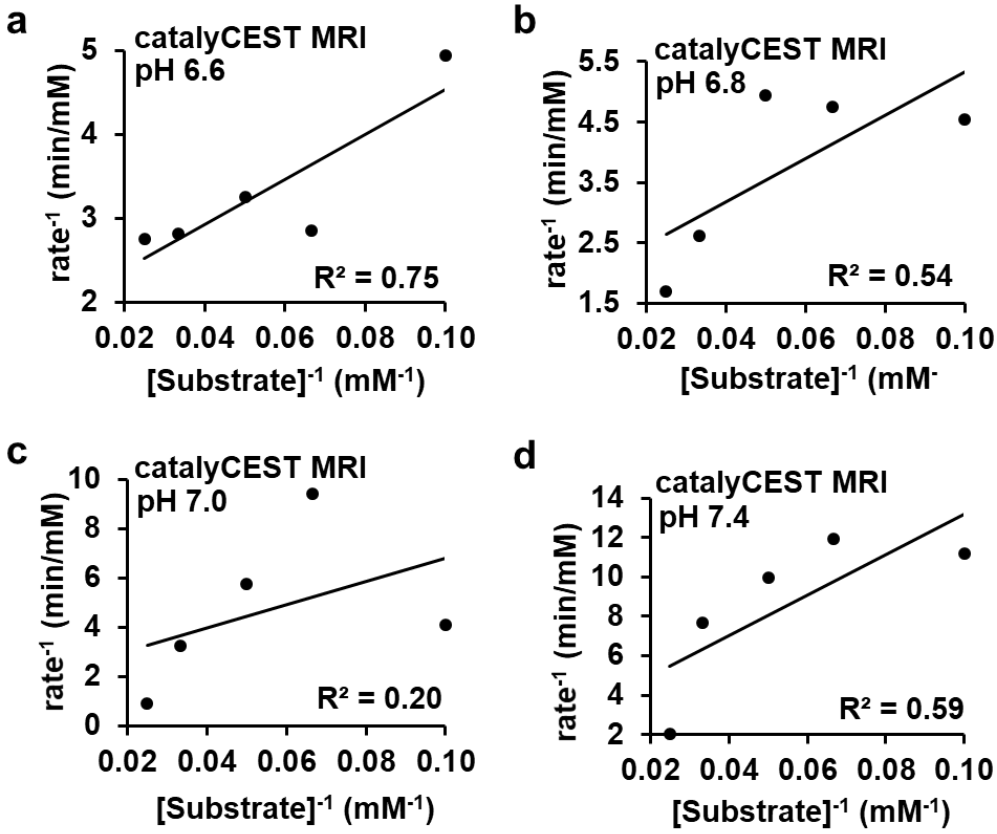

Figure 3.7. Michaelis-Menten kinetics of cathepsin B for cleavage of the substrate agent with catalyCEST MRI. Lineweaver–Burke plots were used to determine Michaelis–Menten kinetics parameters (a-d), at (a) pH 6.6, (b) pH 6.8, (c) pH 7.0, and (d) pH 7.4.

We performed similar Michaelis-Menten enzyme kinetics studies using LC-MS to detect the conversion of the substrate agent to product (Figure 3.8). We incubated cathepsin B with the same substrate concentrations and pH values used in our catalyCEST MRI studies. The product was detected as a dimer during LC-MS evaluations. The temporal decrease in substrate concentration (Figure 3.9) was used to determine the initial rate of each reaction (Figure 3.10), which was then used to construct Lineweaver Burke plots (Figure 3.11) that measured Michaelis-Menten kinetics parameters at each pH condition (Table 3.1).

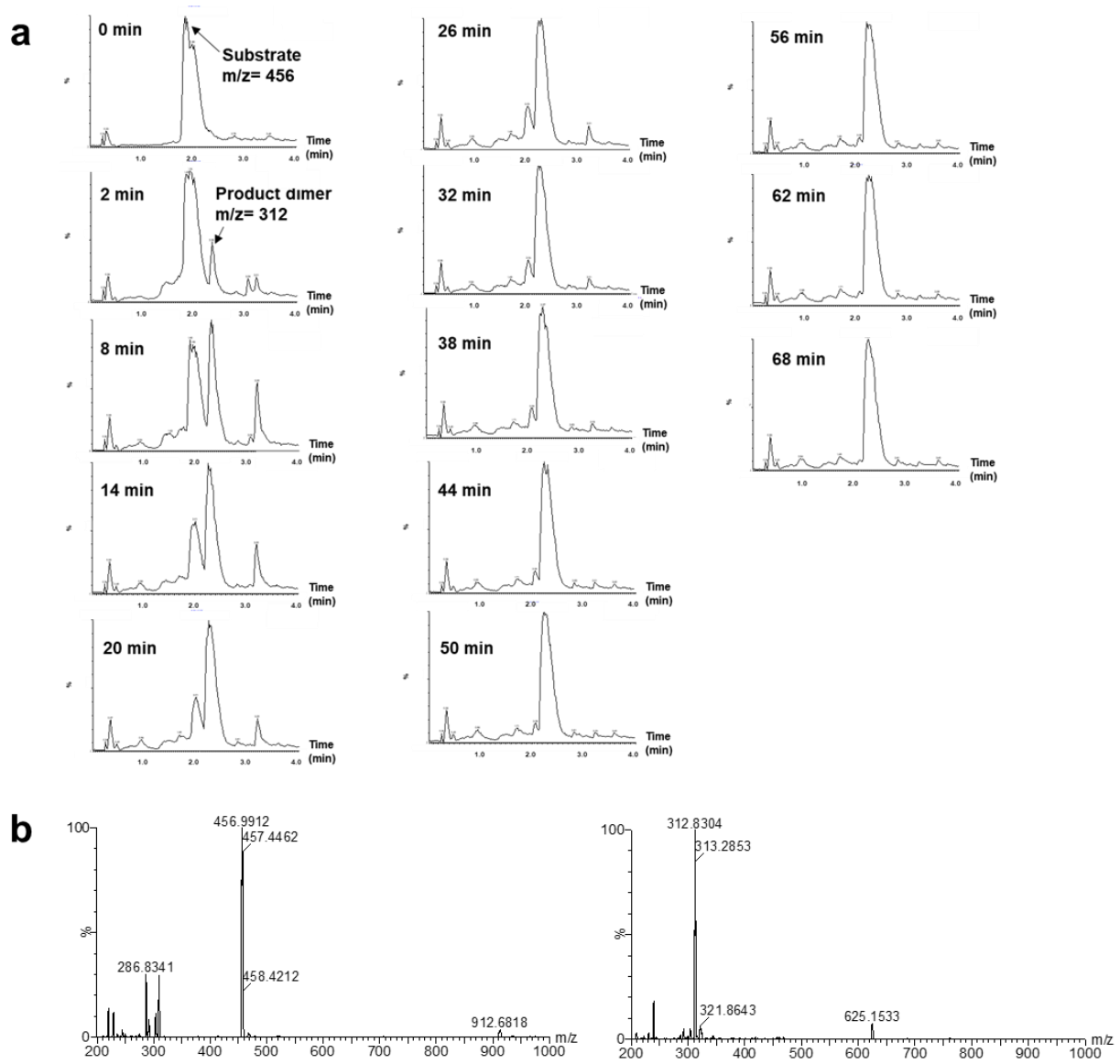

Figure 3.8. LC-MS analysis of substrate cleavage by cathepsin B enzyme a) An example of a Michaelis-Menten kinetics study using LC-MS. Chromatograms were acquired at 0-68 minutes after adding cathepsin B to detect the remaining substrate agent (m/z = 456) and appearance of product (m/z dimer = 312, monomer = 156). b) ESI mass spectra of substrate (left) and product dimer (right). This example used cathepsin B to cleave an initial concentration of 20 mM of substrate agent at pH 6.6.

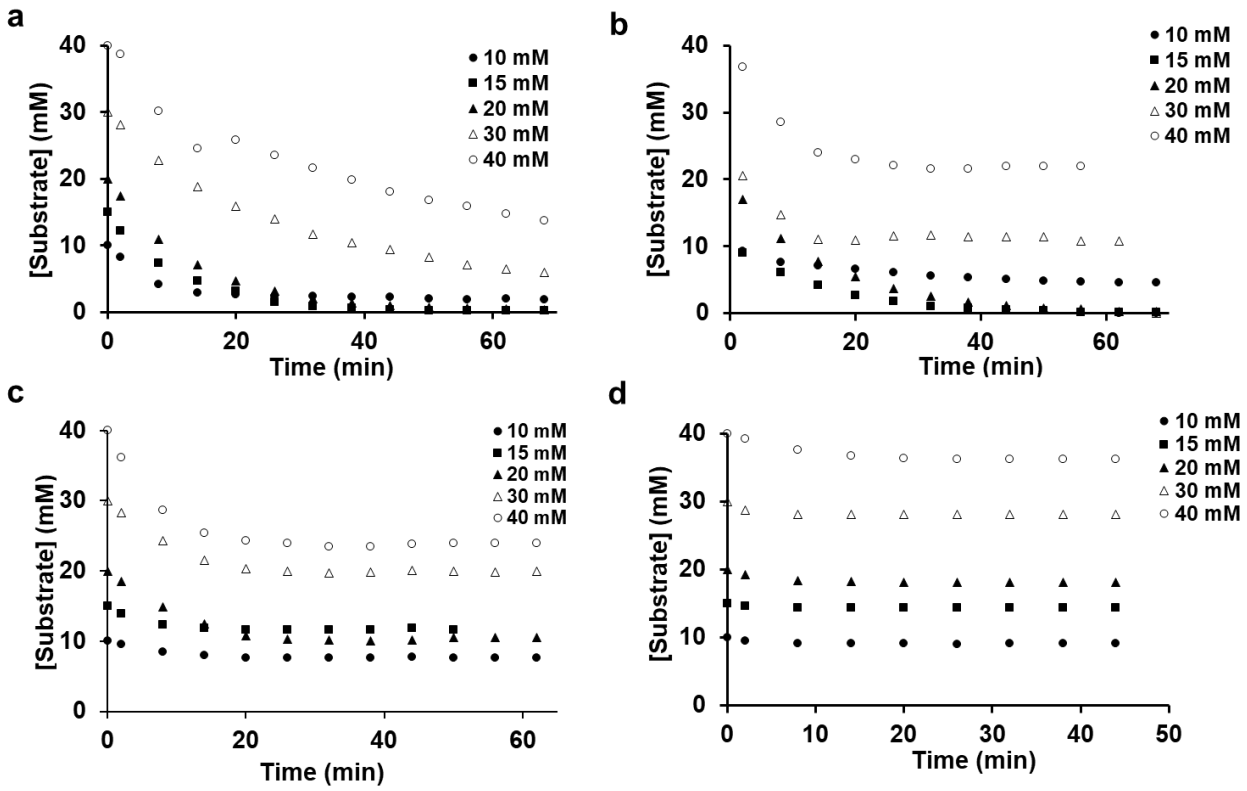

Figure 3.9. Monitoring enzyme cleavage with LC-MS. The area of the substrate peak at different time point correlated with the concentration of the substrate. The area of the substrate peak in LC-MS spectra (Figure 3.8) showed a decrease after adding 131 nM cathepsin B at four different pHs a) 6.6, b) 6.8 c) 7.0 and d) 7.4. The rate was determined by monitoring the change peak area after the addition of cathepsin B enzyme and corelating it to the substrate concentration.

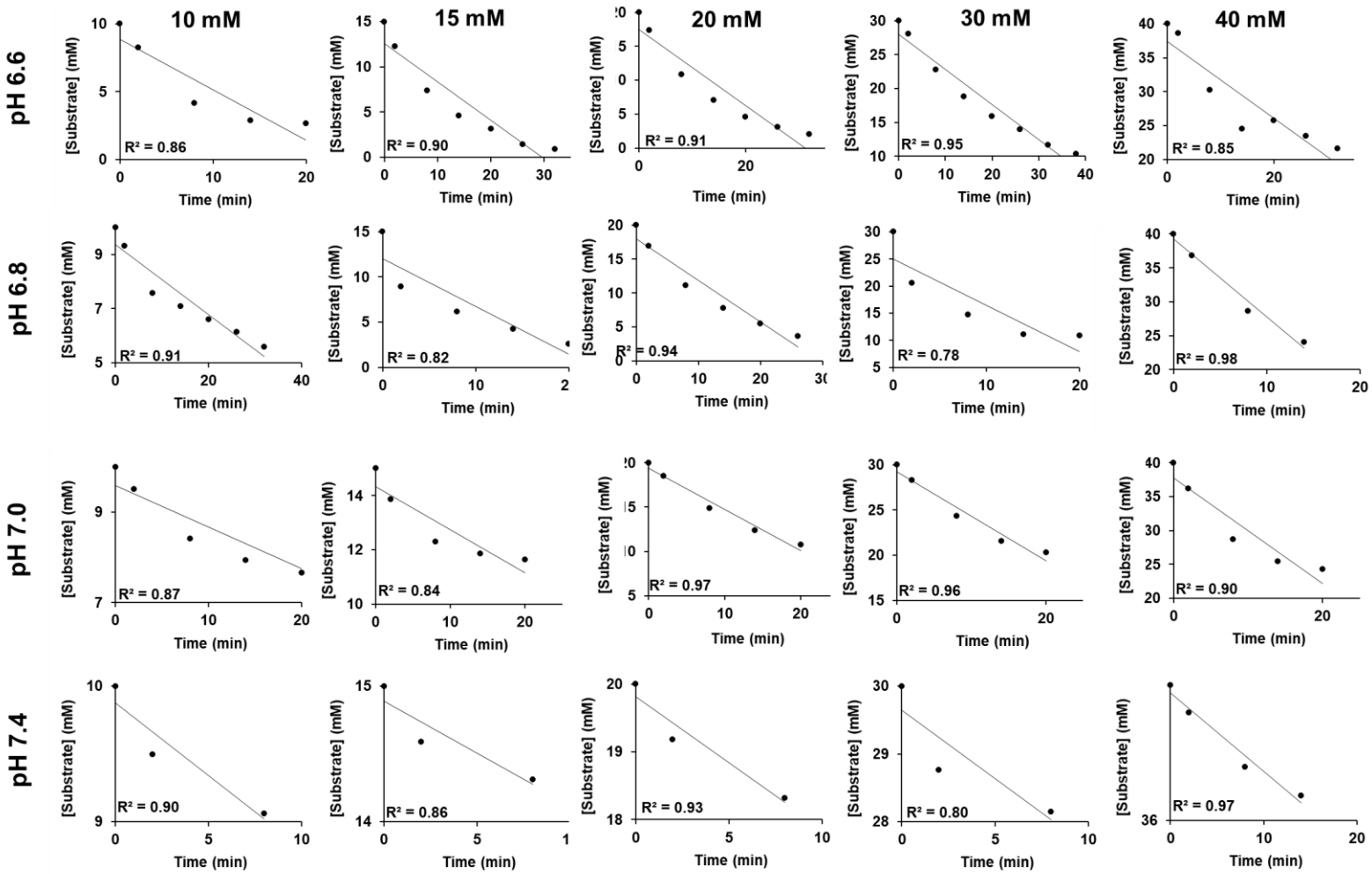

Figure 3.10. Initial velocities of enzyme cleavage as measured with LC-MS. As with Figure 3.9, the substrate agent was treated with cathepsin B at pH 6.6, 6.8, 7.0 and 7.4 using initial substrate concentrations of 10, 15, 20, 30, and 40 mM at 37 °C.

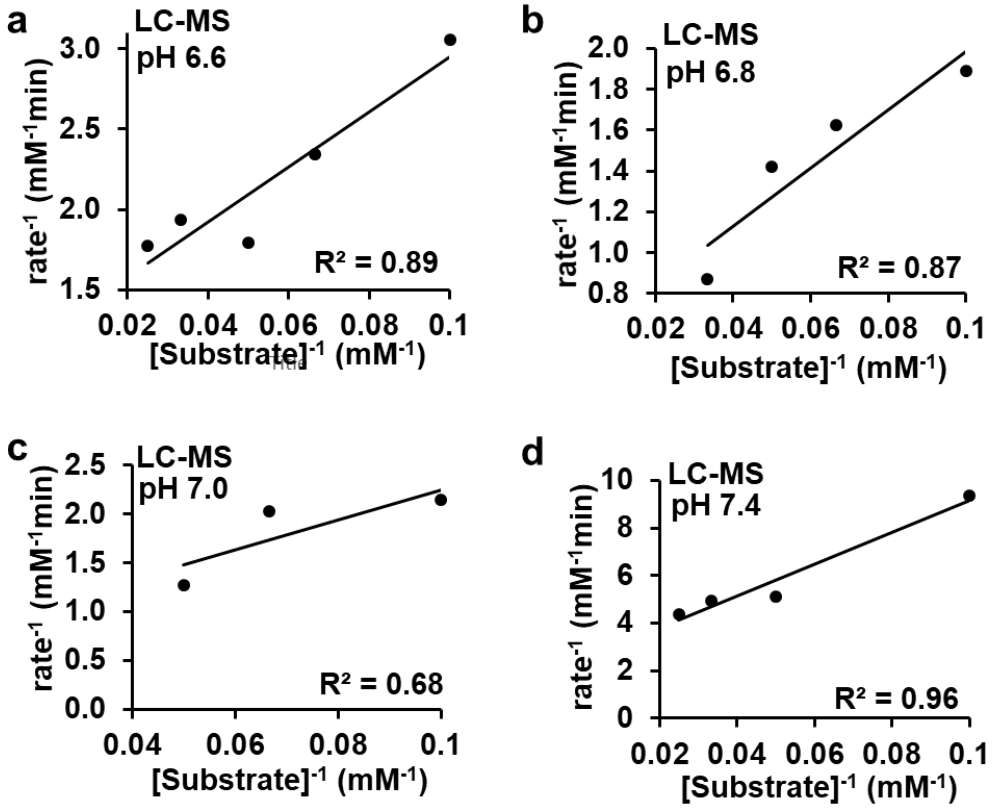

Figure 3.11. Michaelis-Menten kinetics of cathepsin B for cleavage of the substrate agent with LC-MS. Lineweaver–Burke plots were used to determine Michaelis–Menten kinetics parameters (A-D) at (a) pH 6.6, (b) pH 6.8, (c) pH 7.0, and (d) pH 7.4.

Table 3.1 Michaelis-Menten kinetics parameters for cleavage of the substrate agent with cathepsin B, as measured with catalyCEST MRI and LC-MS.

	pH = 6.6		pH = 6.8		pH = 7.0		pH = 7.4	
	CEST MRI	LC-MS	CEST MRI	LC-MS	CEST MRI	LC-MS	CEST MRI	LC-MS
V_{max} (mM min^{-1})	0.540	0.807	0.573	1.776514	0.4755	1.4041	0.341	0.531
K_M (mM)	14.478	13.843	20.521	36.88	22.42	21.49	34.89	32.15
k_{cat} (min^{-1})	4122.48	105670.2	4374	13561.18	3630	10718.32	2605.7	3966.53
k_{cat}/K_M (min^{-1} mM^{-1})	284.74	445.47	213.15	367.69	161.9	498.63	74.67	123.36

The values of the Michaelis constant, K_M, were very similar when measured with catalyCEST MRI and LC-MS, at each pH value. K_M represents a dissociation constant between cathepsin B and the substrate agent, and therefore lower values of K_M indicate higher binding affinity. Our results with catalyCEST MRI and LC-MS both showed that cathepsin B has higher binding affinity at lower pH. The values of the catalytic turnover rate, k_{cat}, were lower when measured with catalyCEST MRI relative to LC-MS, for all pH values. This difference suggests that quantitative evaluations of Michaelis-Menten enzyme kinetics with CEST MRI is subject to more imprecision, as expected because the detection of chemical entities with CEST MRI is an inherently insensitive method relative to LC-MS. Therefore, catalyCEST MRI results should be considered to be semi-quantitative, indicating higher and lower levels of enzyme catalysis. Yet, a semi-quantitative assessment can still provide useful diagnostic results. For example, the results with catalyCEST MRI showed a higher catalytic turnover rate at lower pH, as also shown from the LC-MS studies. The combination of the higher binding affinity and turnover rate at lower pH resulted in a higher k_{cat}/K_M catalytic efficiency measured at lower pH. These studies demonstrated that the quantitative measurement of pH and the semi-quantitative assessment of cathepsin B protease activity are synergistic, as expected.

3.4 DISCUSSION AND CONCLUSIONS

We have successfully developed an agent that can simultaneously measure pH and assess enzyme activity, by combining the designs of previous agents that have been developed for acidoCEST and catalyCEST MRI studies. The CEST signal at 5.0 ppm in the Z-spectrum at 4 μT saturation power can be used to semi-quantitatively monitor the substrate concentration, while the CEST signal at 9.2 ppm in the same Z-spectrum can be used to semi-quantitatively monitor the total concentration of the agent. A low ratio of substrate-to-total concentration indicates high

cathepsin B activity that has converted substrate agent to product, while a high ratio indicates low protease activity that has not appreciably cleaved the substrate agent. The CEST signal at 9.2 ppm in the Z-spectra acquired with 1 and 4 μT saturation power can then be used to measure pH before a significant amount of the agent is cleaved by a protease.

The dual-power acidoCEST MRI approach for measuring pH was previously developed by Longo, Sun, Aime and colleagues when using a contrast agent with one pH-dependent CEST signal [48]. This dual-power approach has been used very effectively for *in vivo* preclinical [48-50] and clinical imaging studies [51,52]. Our approach is similar to their previous approach, although we use a $\log_{10}$ of the CEST-based ratio for comparison with pH (Figure 3.3c,d because pH is a $\log_{10}$ measurement of proton concentration. The $\log_{10}$-based ratio removes some inherent nonlinearity in this CEST-based calibration with pH.

As an alternative method, we and other investigators have developed a dual-signal acidoCEST MRI approach for measuring pH, where two pH-dependent signals on the same CEST agent are used to determine a similar CEST-based ratio [43-47,59-93]. The dual-signal acidoCEST MRI approach requires more complicated chemistry, because this method requires a contrast agent with two CEST signals, where both CEST signals are dependent on pH to different extents. However, the dual-signal acidoCEST MRI approach only requires CEST MRI acquisitions to generate a Z-spectrum at only one saturation power, which reduces total MRI scan time. Furthermore, the CEST signal produced with 1 μT saturation power is low (Figure 3.3a,b), which may compromise the quantitative measurement of the CEST signals at this low power level. For this reason, future studies should consider the development of a more complicated CEST agent that has two pH-dependent CEST signals and a third CEST signal that is dependent on enzyme

activity, so that the faster and more sensitive dual-signal acidoCEST MRI method can be used to simultaneously evaluate pH and protease activity.

A hybrid dual-signal, dual-power acidoCEST MRI approach has also been developed that employs the CEST signal at 5.6 ppm detected with 2 μT saturation power and the CEST signal at 4.2 ppm detected with 1 μT saturation power [94]. This method reduces the direct saturation of water by using low saturation powers, which improves the analysis of the results. Another clever approach, known as a dual-angle acidoCEST MRI method, acquires two sets of CEST images with 180º and 360º flip angles during the CEST saturation period, respectively [95]. The 180º inversion generates more CEST signal than the 360º rotation in a pH-dependent manner. However, both the hybrid dual-signal, dual-power and the dual-angle approach require the acquisition of two CEST MRI datasets, which lengthens total MRI scan time relative to the dual-signal approach, so that these alternative methods are less likely to be translated to clinical practice.

This study demonstrated the challenges of measuring Michaelis-Menten enzyme kinetics parameters with catalyCEST MRI. We carefully performed our studies with a stable 37 ºC temperature because chemical kinetics rates are typically dependent on temperature. We also carefully performed CEST MRI studies with a customized sample holder that minimized B_0 and B_1 in homogeneities, resulting in excellent image quality (Figure 3.2a,b). We also accounted for the non-linear relationship between CEST signal and agent concentration by using the LB-concentration analysis method (Figure 3.5), rather than assuming a (pseudo)linear relationship between CEST signal and concentration. Despite these considerations, our measurements of the k_{cat} catalytic turnover rate were lower with catalyCEST MRI relative to LC-MS analyses.

We have previously used the same catalyCEST MRI methodology to evaluate the kinetics of other enzymes, which resulted in the measurement of k_{cat} rates that were accurate relative to

measurements with other methodologies [20,26,27]. However, the k_{cat} rates of these other enzymes were relatively slow, allowing for slow, multi-hour kinetics studies with catalyCEST MRI. The higher k_{cat} rate of cathepsin B, as measured with LC-MS in our study, only allowed for catalyCEST MRI studies for less than one hour that resulted in a limited number of data points for our Lineweaver-Burke plots (Figure 3.11), which may have led to inaccurate k_{cat} measurements. These results further emphasize that catalyCEST MRI should be used for semi-quantitative assessments of enzyme activities. Semi-quantitative analyses can still provide value, as evidenced by our study that showed that cathepsin B has higher catalytic efficiency at lower pH.

CHAPTER 4

FUTURE DRECTIONS

4.1 SUMMARY OF CURRENT STUDIES WITH CEST MRI

We have developed diaCEST MRI probes to monitor tumor extracellular pH and enzyme activities. Using a polymeric agent, we improved the inherently low sensitivity associated with CEST MRI. We successfully demonstrated that diaCEST MRI can effectively measure tumor extracellular pH and detect enzyme activities. So, we need to explore the other aspects of diaCEST MRI to assess different biomarkers.

4.2 IMPROVEMENTS TO CURRENT STUDIES

4.2.1 pH POLYMER STUDY

Our research has shown that salicylic acid has limitations when measuring pH because the pH measurement is dependent on concentration. Thus, in the future, we need to evaluate the feasibility of concentration-independent pH measurements using polymeric agents that are synthesized from known agents. 5,6-dihydrouracil is a derivative of a nucleic acid base, uracil, and is also a known pH-responsive CEST agent [1]. The amide protons of 5,6-dihydrouracil are inequivalent and generate two CEST signals at 5.0 ppm and 2.67 ppm. These two signals can be used to obtain the concentration-independent ratiometric pH measurements. Thus, I propose to synthesize a 5,6-dihydrouracil-based polymeric agent (Scheme 4.1).

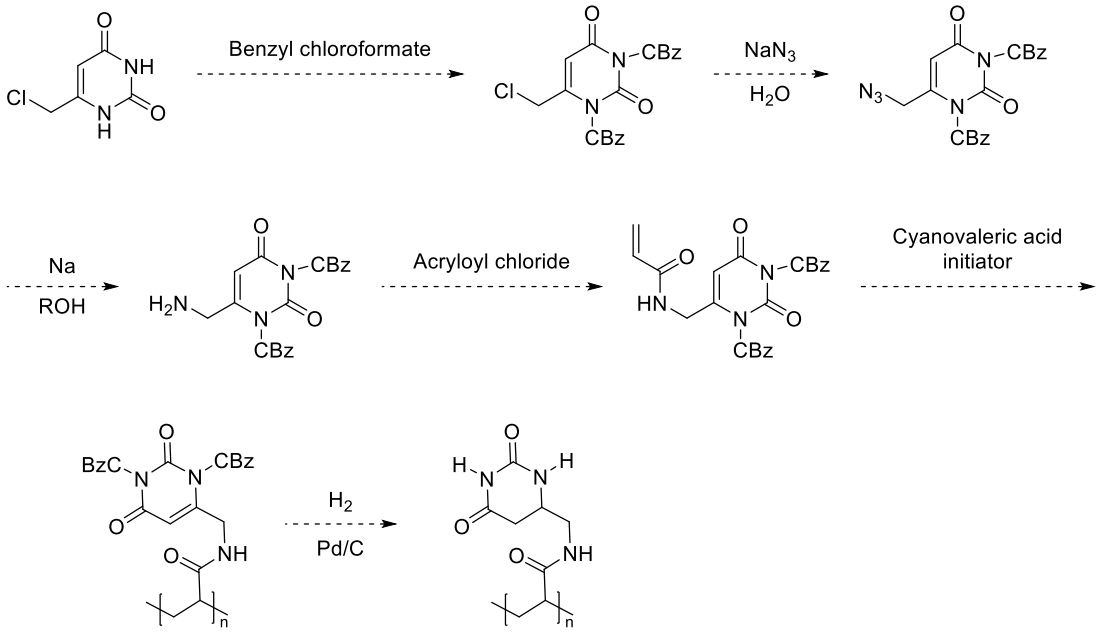

Scheme 4.1. The proposed synthesis of a 5,6-dihydrouracil-based polymeric agent

Moreover, a biopolymer consisting of hyaluronic acid is also a pH-sensitive polymer [2], and its CEST properties have also been reported [3]. The amide proton signals at two power levels could produce independent concentration measurements of pH.

4.2.2 SIMULTANEOUS DETECTION OF pH AND ENZYME ACTIVITY STUDY

The catalyCEST agents that detect enzyme activities can be improved by making these agents more enzyme-specific. If there is a lack of specificity for a particular enzyme, then the substrate will be cleaved by other enzymes, resulting in an overestimation of the activity by the enzyme of interest. We used a Phe-Arg substrate for the detection of cathepsin B enzyme activity. However, a recent study [4] reported cathepsin B specific fluorogenic substrates using unnatural amino acids. Those substrates exhibit higher catalytic efficiency over substrates that contains the Phe-Arg sequence (Table 4.1).

Table 4.1. The catalytic efficiency for some synthetic fluorogenic substrates for the cathepsin B enzyme.

Substrate	k_{cat}/K_M ($M^{-1}S^{-1}$)
Ac-Cha-Leu-hSer(Bzl)-Arg-ACC	4,300,000
Ac-Cha-Leu-Glu(Bzl)-Arg-ACC	3,100,000
Cbz-Arg-Arg-AMC	165,000
Cbz-Phe-Arg-AMC	400,000

4.3 CEST MRI PROBES FOR TARGETED IMAGING OF TUMORS EXPRESSING FOLATE RECEPTORS.

Receptor targeted imaging is mostly conducted using fluorescence and radionuclide-based techniques such as PET [5]. However, radioactive probes exhibit safety concerns, whereas fluorescent probes have poor tissue penetration for clinical imaging. Therefore, it is crucial to investigate a non-radioactive imaging strategy with a higher penetration depth for targeted imaging. MRI has exhibited potential for receptor imaging using paramagnetic probes. However, renal toxicity is associated with metal-containing probes, makes these agents more elusive towards clinical translation [6,7]. Thus, non-metallic, non-toxic imaging probes are likely to become the future in targeted imaging. Recently reported dextran-based [8] and PAMAM-dendrimer based [9] imaging probes proved the feasibility of diaCEST MRI for receptor-targeted imaging.

A common tumor enriched antigen, folate receptor (FR), is often vastly expressed [10]. For instance, the level of FR type α expression could be as high as 2.8 million receptors per cancer cell. Thus, FR shows greater potential for use in CEST MRI. However, folic acid shows very low solubility in aqueous solution and cause problems during *in vivo* administration. This problem can

be avoided by adding a PEG linker between the target warhead and the imaging probe. We propose diaCEST imaging probes that are linked to the PEGylated folic acid. For instance, a well-known diaCEST probe, salicylic acid, may be conjugated to PEGylated folic acid (Figure 4.1). Water-soluble PEGylated (MW-2000) folic acid is either commercially available or can be synthesized from a few steps. The proposed agent could be altered by conjugating other known diaCEST probes such as dextran and hyaluronic acid.

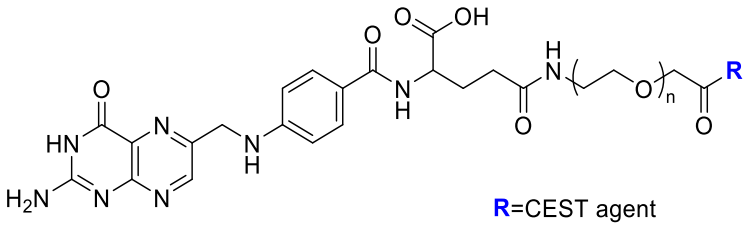

Figure 4.1. The proposed diaCEST MRI probe for tumor targeted imaging.

As mentioned earlier, CEST is an inherently insensitive technique. Thus, a relatively higher number of exchangeable protons in the agent and as well as high receptor density in the cell are key considerations for CEST imaging to be used for targeted imaging. We need to assess the feasibility of folic acid conjugated to different CEST agents to be used as targeted agents. So, we assume a 500×500 μm ×1 mm (1 mm slice thickness) voxel for small animal imaging. The volume of the voxel is 2.5×10^{-4} mL. The diameter of a cell is approximately 3 μm and assuming a cell is spherical, the volume of a cell is 1.4×10^{-11} mL. We assume that 50% of the tumor volume is occupied by the intracellular volume. The estimated number of cells in an MRI voxel is determined as:

1.25×10^{-4} mL half voxel/ 1.4×10^{-11} mL cell volume = 9×10^{6} cells ≈ 1×10^{7} cells.

Assuming all cells express 2.8 million folate receptors per cell, the total number of receptors is 2.8×10^{13} ((1×10^{7} cells)× (2.8×10^{6} receptors/cell)).

The molarity of receptors in the voxel is determined as:

$[(2.8 \times 10^{13}$ receptors) / $(6.022 \times 10^{23}$ molecules/mole)]/2.5×10^{-7} L = 186 μM

The detection threshold for CEST MRI is approximately 10 mM. According to the molarity of receptors in a voxel, an agent with one exchangeable proton is not sufficient to give detectable CEST contrast (Table 4.2-entry 1). To improve the sensitivity of the proposed salicylic acid conjugated agent for targeted imaging, salicylic acid and PEGylated folic acid can be conjugated to a PAMAM dendrimer. The dendrimer conjugated agent can increase the number of exchangeable groups attached to one dendrimer molecule, and thus improve the sensitivity of CEST imaging (Table 4.2-entry2).

A salicylic acid moiety could be conjugated to a PAMAM-NH_2 dendrimer (Scheme 4.2) [9] and then, PEGylated folic acid could be conjugated to remaining amine terminals in the dendrimer (Scheme 4.3) [11].

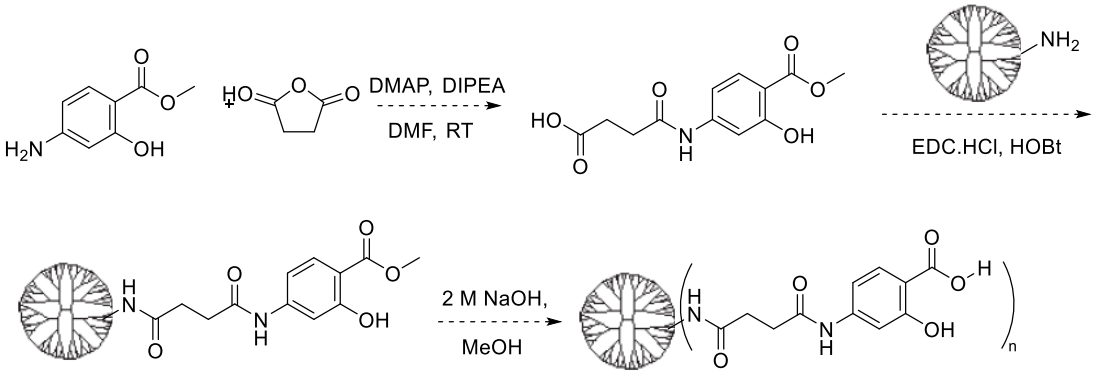

Scheme 4.2. The proposed synthesis for the conjugation of a salicylic acid moiety to a PAMAM-NH_2 dendrimer.

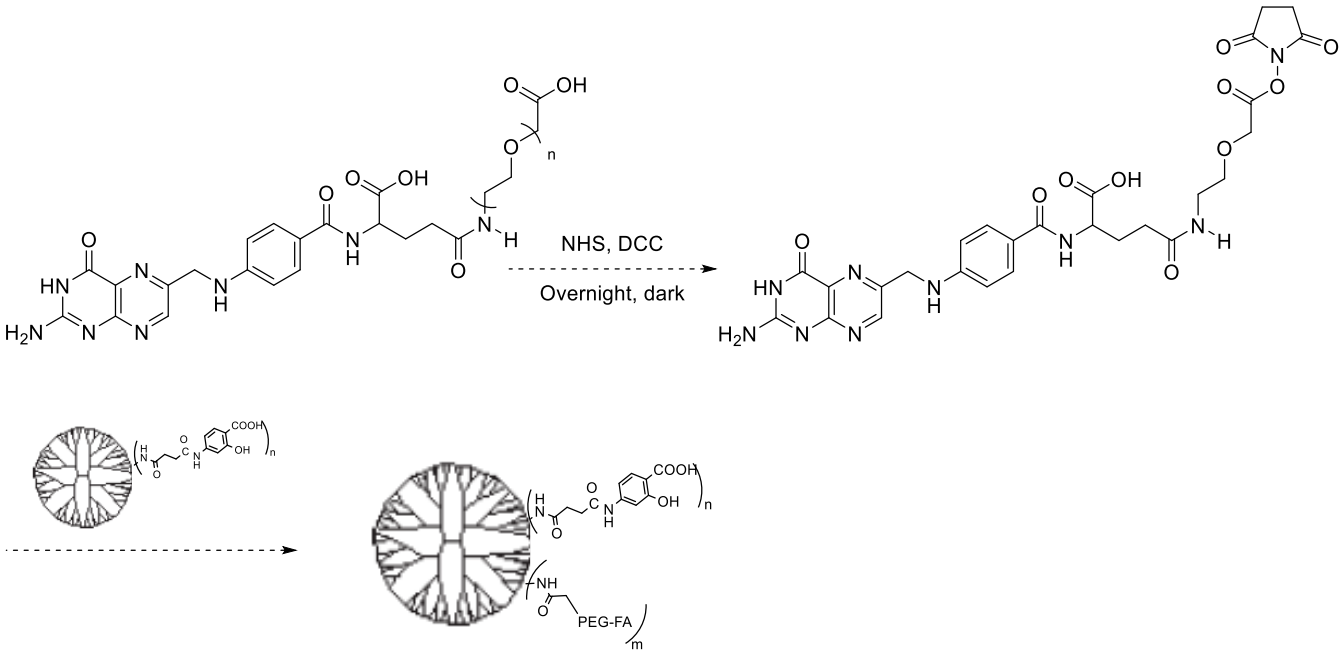

Scheme 4.3. The proposed synthesis for conjugating of PEGylated folic acid to remaining amine terminals in a PAMAM-NH_2 generation 5 dendrimer.

Table 4.2 also shows other proposed folic acid conjugated agents with multiple exchangeable protons and their ability for use in targeted CEST MRI.

Table 4.2 Feasibility of proposed agents for targeted imaging

Agent	Number of exchangeable protons per agent	Exchangeable proton concentration in the voxel
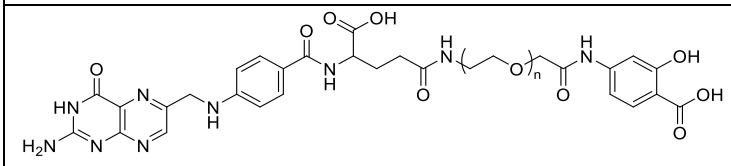	1	1 × 186 μM = 0.186 mM
PAMAM G5-conjugated agent	Available free NH_2 terminals for the conjugation=128 If 50% amines are conjugated with salicylic	63 × 186 μM = 11 mM

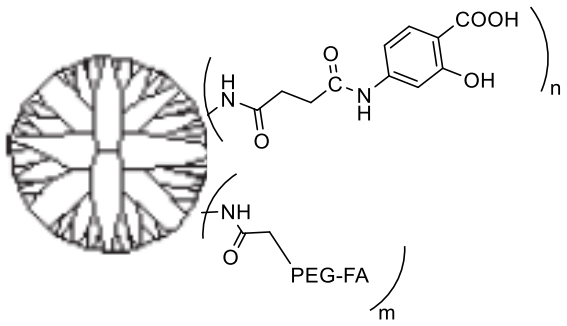	acid, exchangeable protons per agent= 64	
Dextran-10kDa conjugated agent[8] 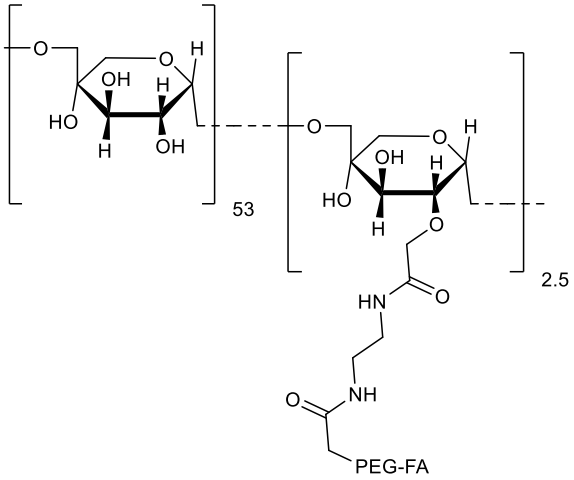	3 hydroxyls in one unit and total 159 exchangeable protons per agent	159 × 186 μM = 30 mM
Hyaluronic acid conjugated agent [12] 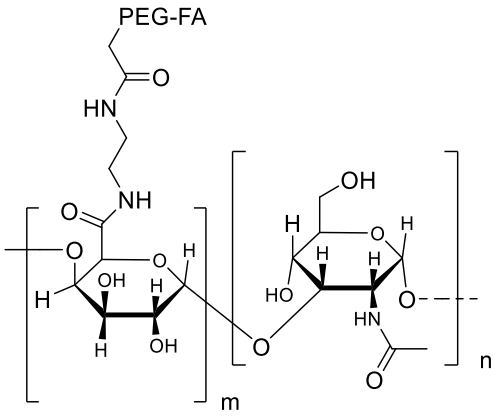	If we start with 30,000-50,000 Da hyaluronic acid, assuming average MW is 40 kDa, total number of exchangeable amide proton is 88.	88 × 186 μM = 16 mM

4.4 DETECTION OF ELEVATED LEVELS OF IRON IONS (Fe^{2+}) IN NEUROLOGICAL DISORDERS USING A RESPONSIVE CEST MRI PROBE.

Responsive CEST MRI probes have been used to detect many biomarkers such as enzyme activity [13], pH [14], metal ions [15], redox state [16], metabolites, and gene expression [17]. Iron plays a crucial role in the human body as the most abundant transition metal. However, iron metabolism irregularities can lead to several disease conditions such as anemia [18], cancer [19], and cardiovascular diseases [20]. Even though the biological function of iron is often involved with protein complexation, water soluble free Fe^{2+} can also be found in a reducing environment of the cell. It is also known that elevated levels of Fe^{2+} are present in neurological disorders such as Alzheimer's disease. Free Fe^{2+} ions play crucial roles in cellular and physiological functions. However, the correlation between elevated iron ion levels with its biological function needs to be clarified more thoroughly. Therefore, it is important to find a tool to monitor the elevated levels of Fe^{2+} to understand the indeterminate biological role. Noninvasive imaging of free Fe^{2+} in the biological system gives a more accurate measurement. So, a responsive diaCEST MRI probe can effectively measure the elevated levels of Fe^{2+} ion the body.

Fe^{2+} mediates the specific cleavage of N-aryl-O-acylhydroxylamine to an amine. I propose to use this specific cleavage strategy that displays a highly selective and sensitive response toward Fe^{2+} over the other biologically available metal ions and species (Figure 4.2) [21].

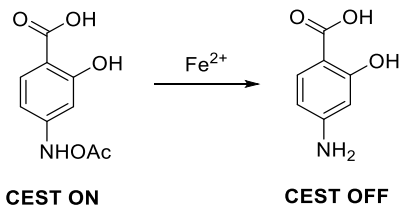

Figure 4.2. The proposed diaCEST responsive CEST MRI probe to detect Fe^{2+}.

In the presence of a Fe^{2+} ion, N-aryl-O-acylhydroxylamine converts to an amine. Aryl-O-acylhydroxylamine is expected to have a slower chemical exchange rate compared with the amine. Therefore, we expect to see a CEST peak for aryl-O-acylhydroxylamine before cleavage, and a CEST peak should disappear after cleavage. The probe can be synthesized from commercially available 4-nitrosalicylic acid in 4 steps (Scheme 4.4).

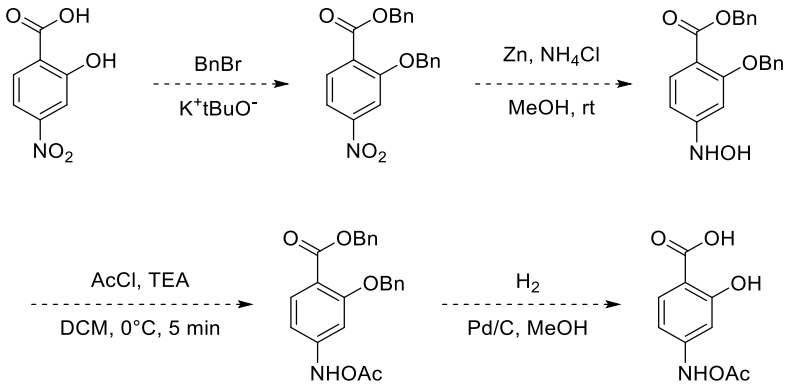

Scheme 4.4. The proposed scheme for synthesis of a CEST probe that can detect Fe^{2+}.

4.5 SALICYLIC ACID FUNCTIONALIZED C-DOTS AS A DIACEST MRI AGENT

The increasing attention of carbon dots for biomedical applications is often associated with their low toxicity, chemical inertness, surface functionalization ability, and good water solubility [22]. The feasibility of using carbon dots as diaCEST agents has been investigated recently using arginine as the source for the exchangeable protons of the CEST agent.[23]. However, the CEST signal of this agent is close to the water signal and overlaps with endogenous CEST contrast, which is problematic for *in vivo* imaging. Thus, carbon dots with exchangeable protons that resonate farther downfield evades the problems associated with the overlap with endogenous CEST contrast and closeness to the water resonance. I propose to functionalize the carbon dots with salicylic acid, which has exchangeable protons that resonate at 9.0 ppm (Scheme 4.5). Carbon dots can be functionalized with salicylic acid either directly or indirectly with acetylsalicylic acid followed by

hydrolysis of the methyl group. Salicylic acid functionalized carbon dots could be synthesized by a one-step microwave-assisted strategy through condensation of salicylic acid and hydrazine carbonization [24]. Considering the known low toxicity and good water solubility of C-dots [22], salicylic acid functionalized C-dots could be used to detect the tumor extracellular pH using the two power ratiometric CEST MRI method [25].

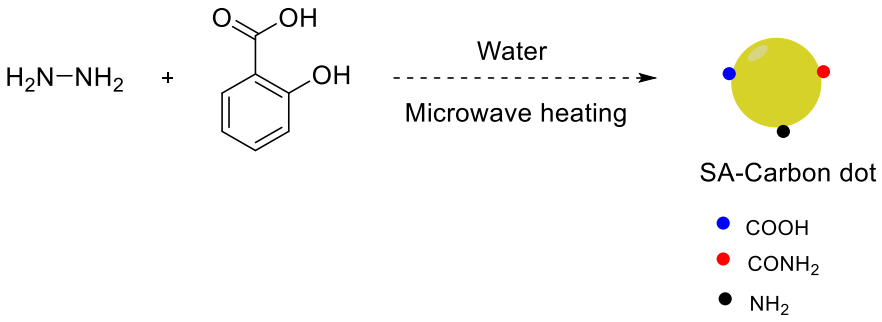

Scheme 4.5. The proposed scheme for synthesis of salicylic acid functionalized carbon dots (SA-Carbon dot).

4.6 POSSIBLE CEST CONTRAST AGENTS AVAILABLE AS PHARMACEUTICAL PRODUCTS

Exogeneous CEST contrast agents are still under investigation for clinical use. So, it is important to explore clinically translatable CEST agents to transform CEST imaging from the bench to the bedside. I propose to explore pharmaceutical products currently available in the market to find possible CEST contrast agents. If we discover CEST agents from FDA approved pharmaceutical products, it is much easier to translate them into the clinic. Also, these compounds can be used as theranostic agents to diagnose and treat diseases at the same time. Njardarson and coworkers have published a poster called “Top 200 SMALL Molecule Drugs by Sales in 2018” [26]. Among the 200 small molecule drugs that are listed on the poster, I propose that the following small molecule drugs in Table 4.3 with exchangeable protons are possible CEST agents. Amide

protons have a relatively slow exchange rate and exhibit good CEST contrast. Though the aliphatic OH signal shows up close to the water signal, it displays good contrast. Depending on the neighboring groups of the OH peak, the MR resonance of the OH signal can be further downfield and can be distinguished from the water signal. Thus, I have suggested molecules that mostly consist of amides and aliphatic alcohols as exchangeable protons. However, the highest therapeutic dose of these drugs needs to be considered to for pre-clinical and clinical applications.

Table 4.3. Possible pharmaceutical drugs that can be used as CEST agents.

Formoterol 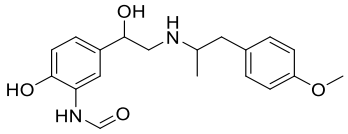	**Cabazitaxel** 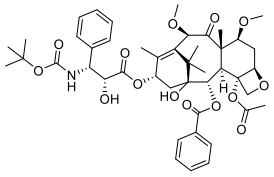	**Acetaminophen** 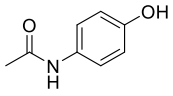	**Ninlaro** 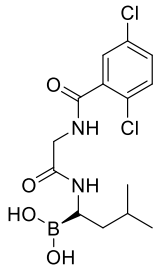
Goserelin 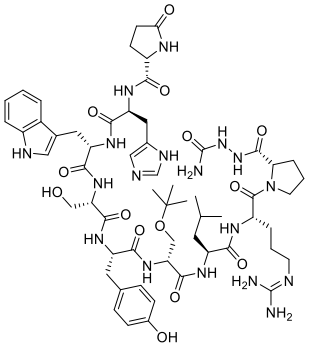	**Bortezomib** 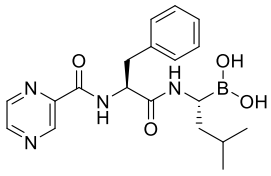	**Ertapenem** 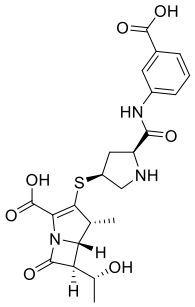	**Ivacaftor** 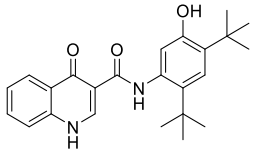
Daptomycin	**Dutasteride** 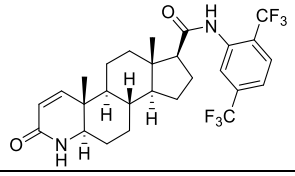	**Acarbose**	**Regorafenib**

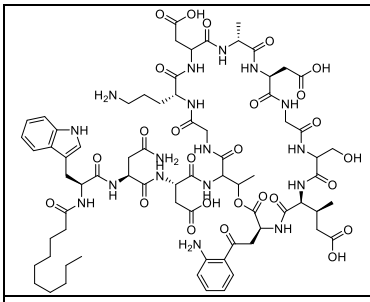		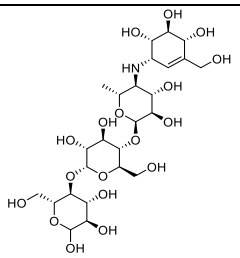	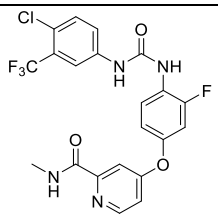
Vasopressin 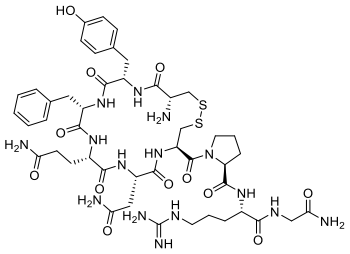	**Cyclosporin A** 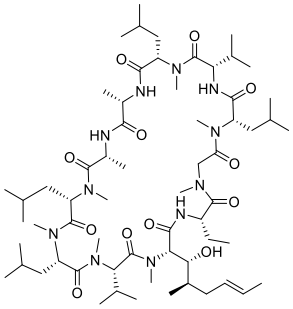	**Capecitabine** 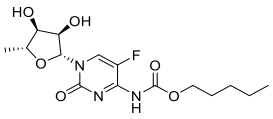	**Sorafenib** 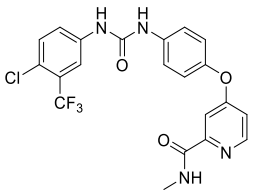
Triptorelin 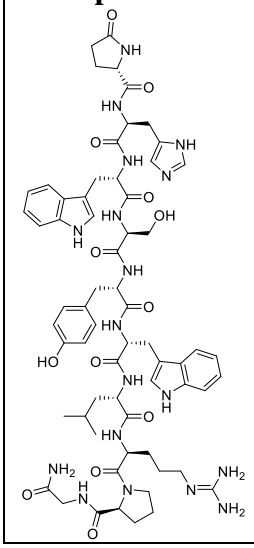	**Amphotericin B** 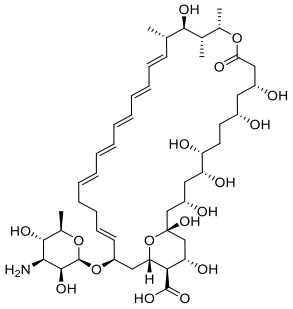	**Carboxymaltose** 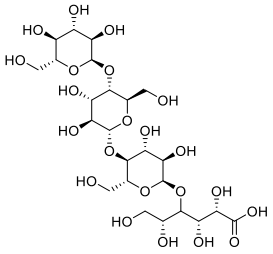	**Atazanavir** 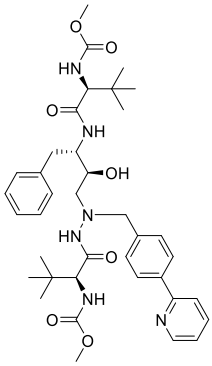

APPENDIX A

SUPPLEMENTARY DATA

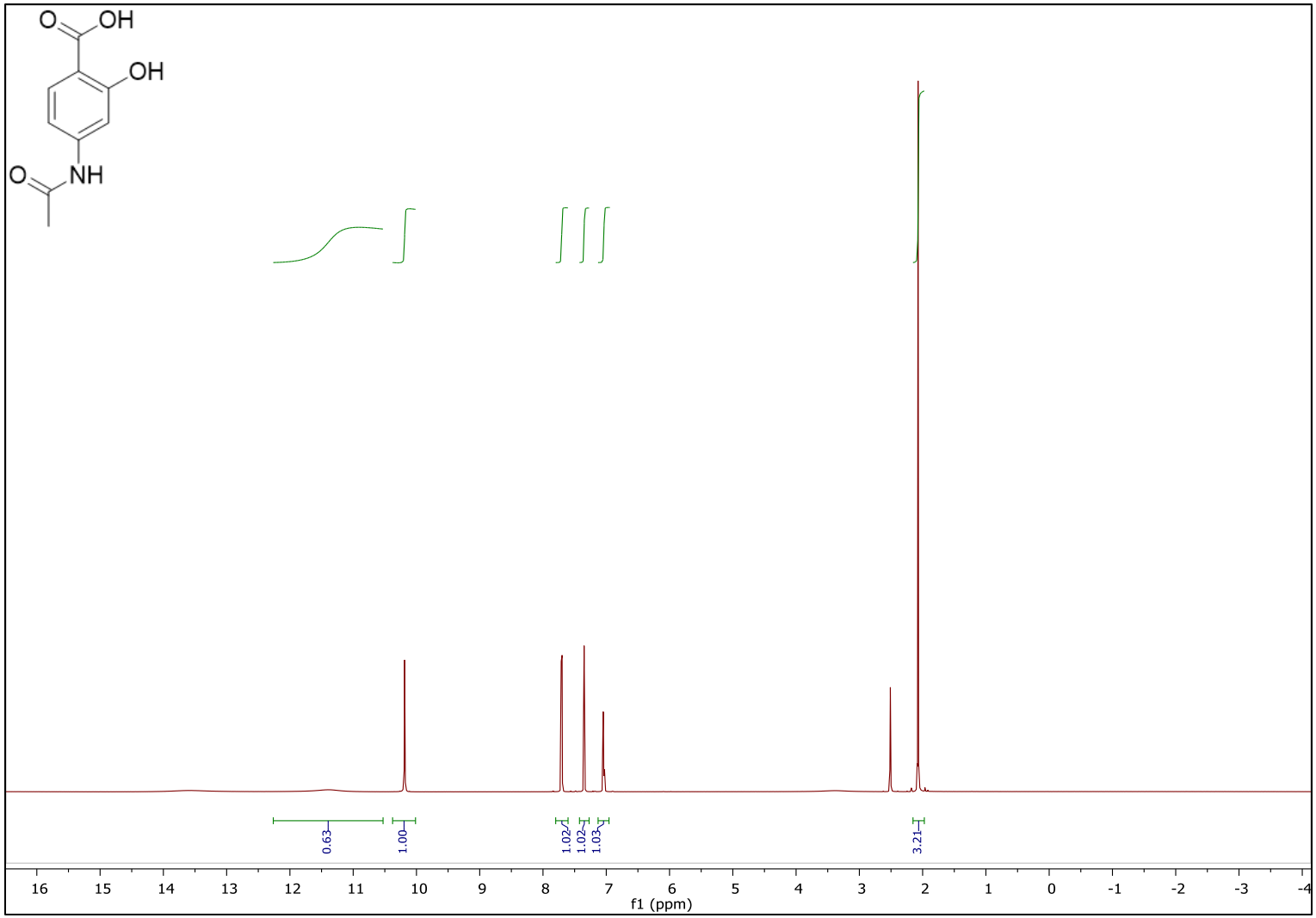

Figure A1. ^{1}H NMR of 4-acetamido-2-hydroxybenzoic acid.

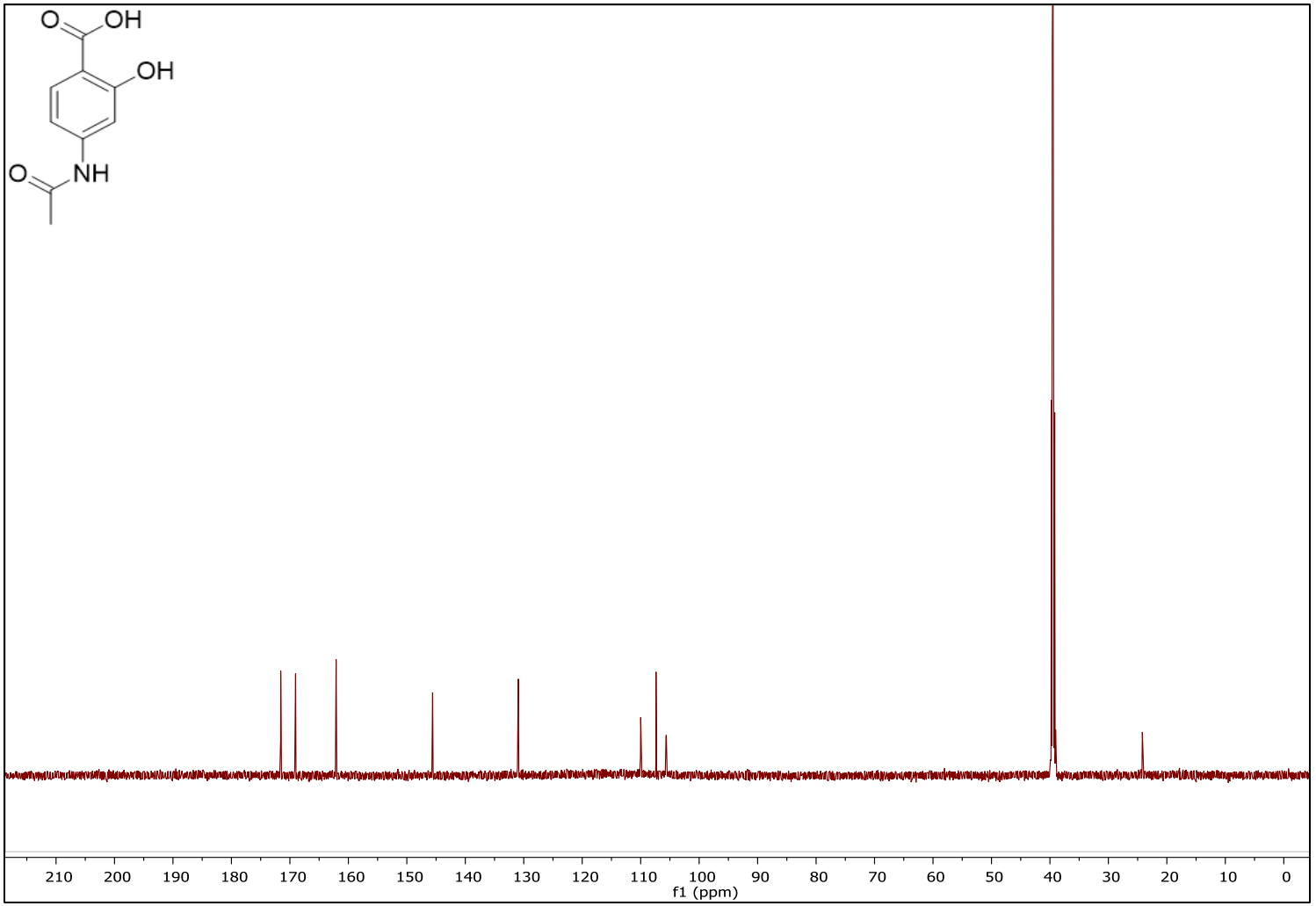

Figure A2. ^{13}C NMR of 4-acetamido-2-hydroxybenzoic acid.

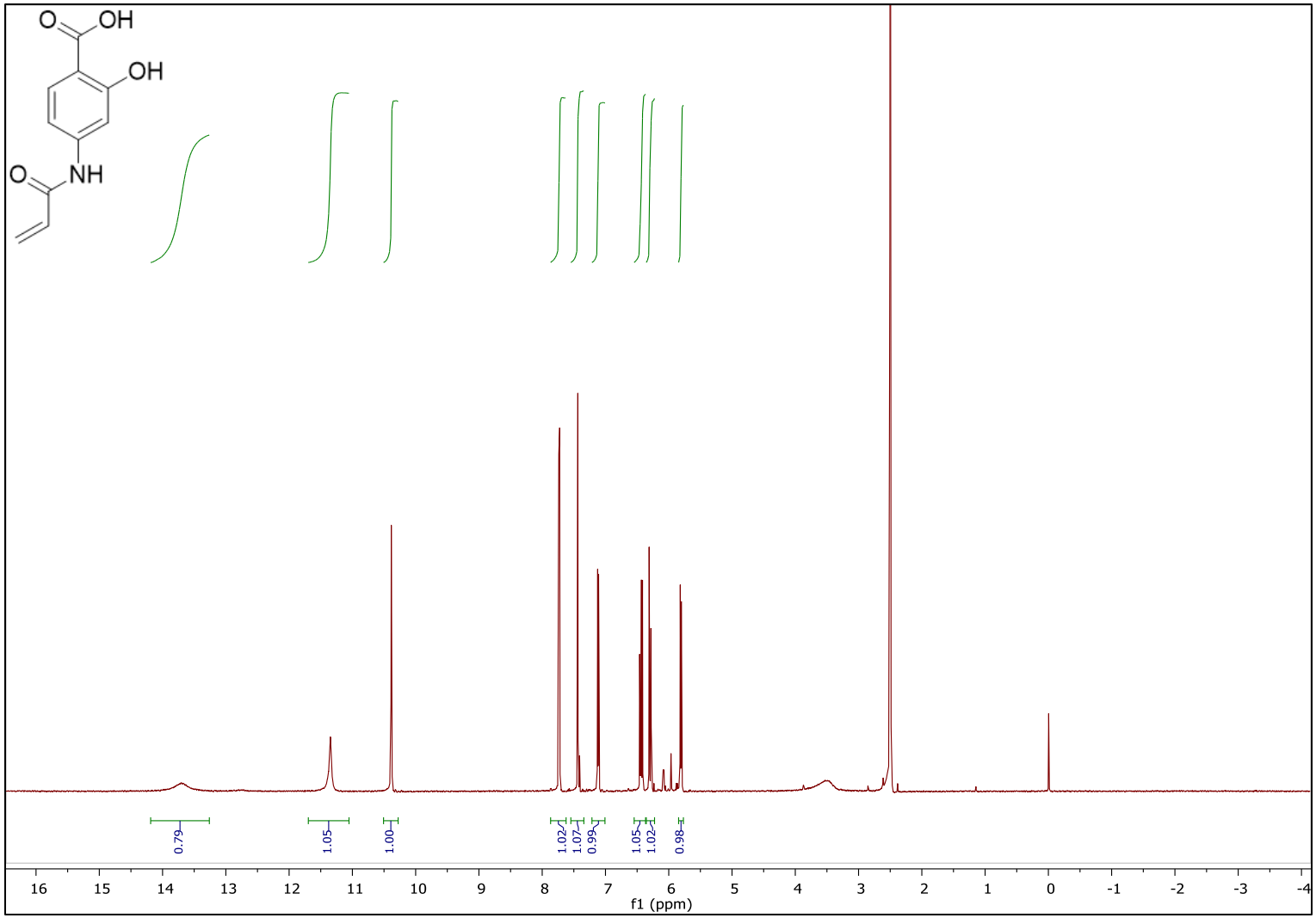

Figure A3. ^{1}H NMR of 4-acrylamidosalicylic acid.

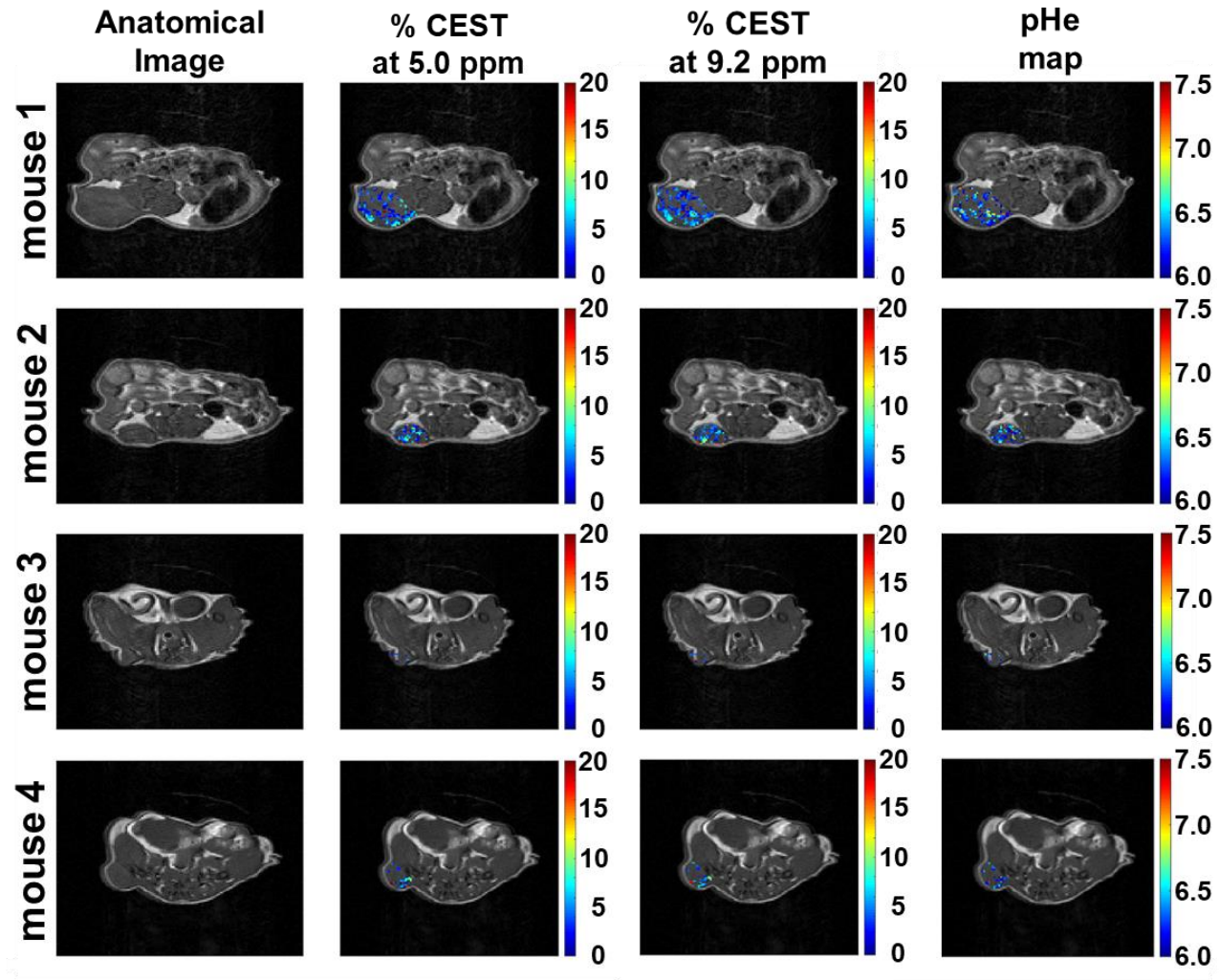

Figure A4. *In vivo* CEST MRI of a MDA-MB-231 tumor model following i.v. injection of iopamidol at a dose of 4.5 g/kg (n = 4). Anatomical images show the location of the tumor (first column). The parametric maps of % CEST signal amplitude at 5.0 ppm (second column) and 9.2 ppm (third column) demonstrate good detection of both CEST effects. The pHe maps (fourth column) show colorful pixels where two significant CEST contrast were measured and converted to pHe values.

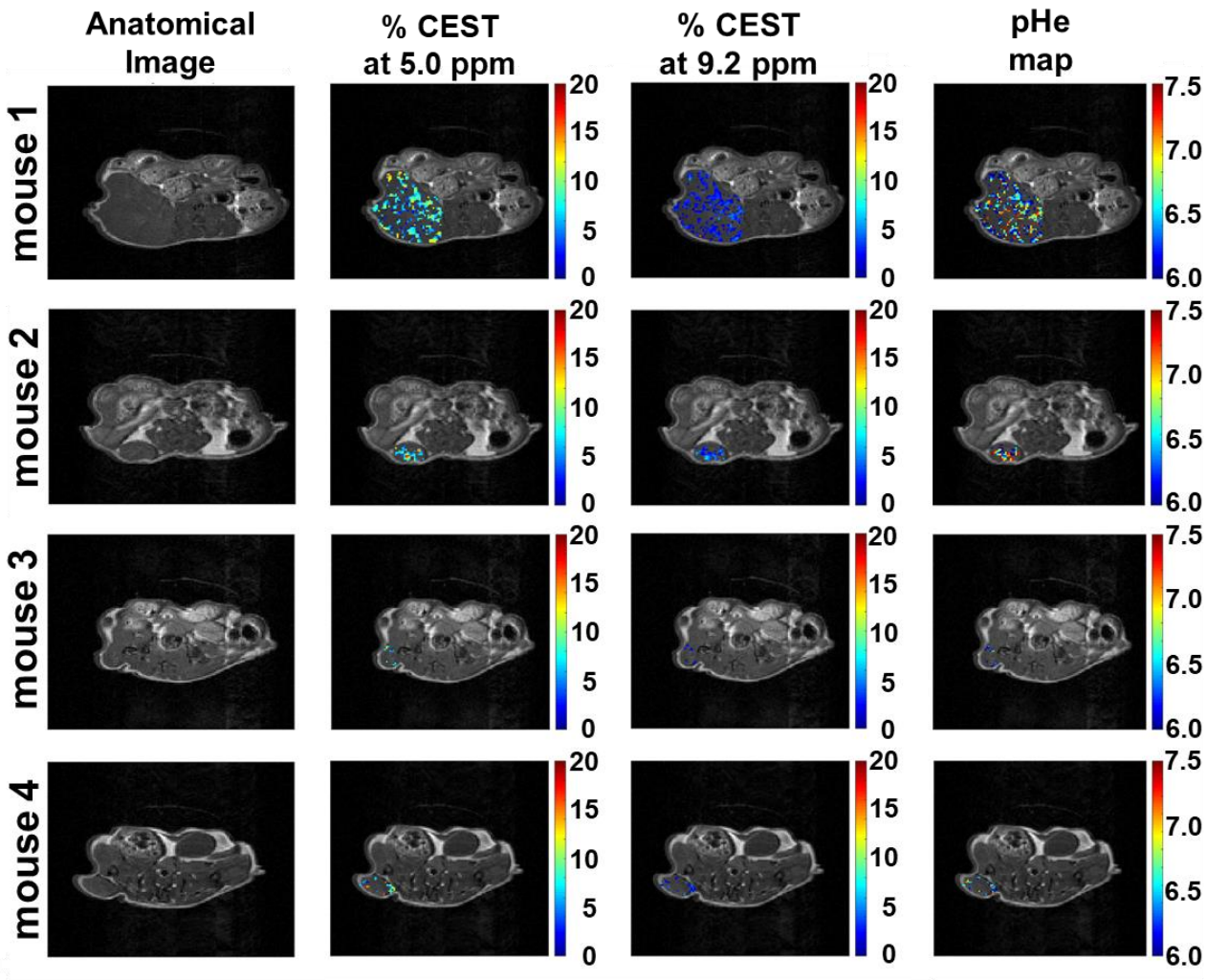

Figure A5. *In vivo* CEST MRI of a MDA-MB-231 tumor model following i.v. injection of monomer agent at a dose of 0.32 g/kg (n = 4). Anatomical images show the location of the tumor (first column). The parametric maps of % CEST signal amplitude at 5.0 ppm (second column) and 9.2 ppm (third column) demonstrate good detection of both CEST effects. The pHe maps (fourth column) show colorful pixels where two significant CEST contrast were measured and converted to pHe values.

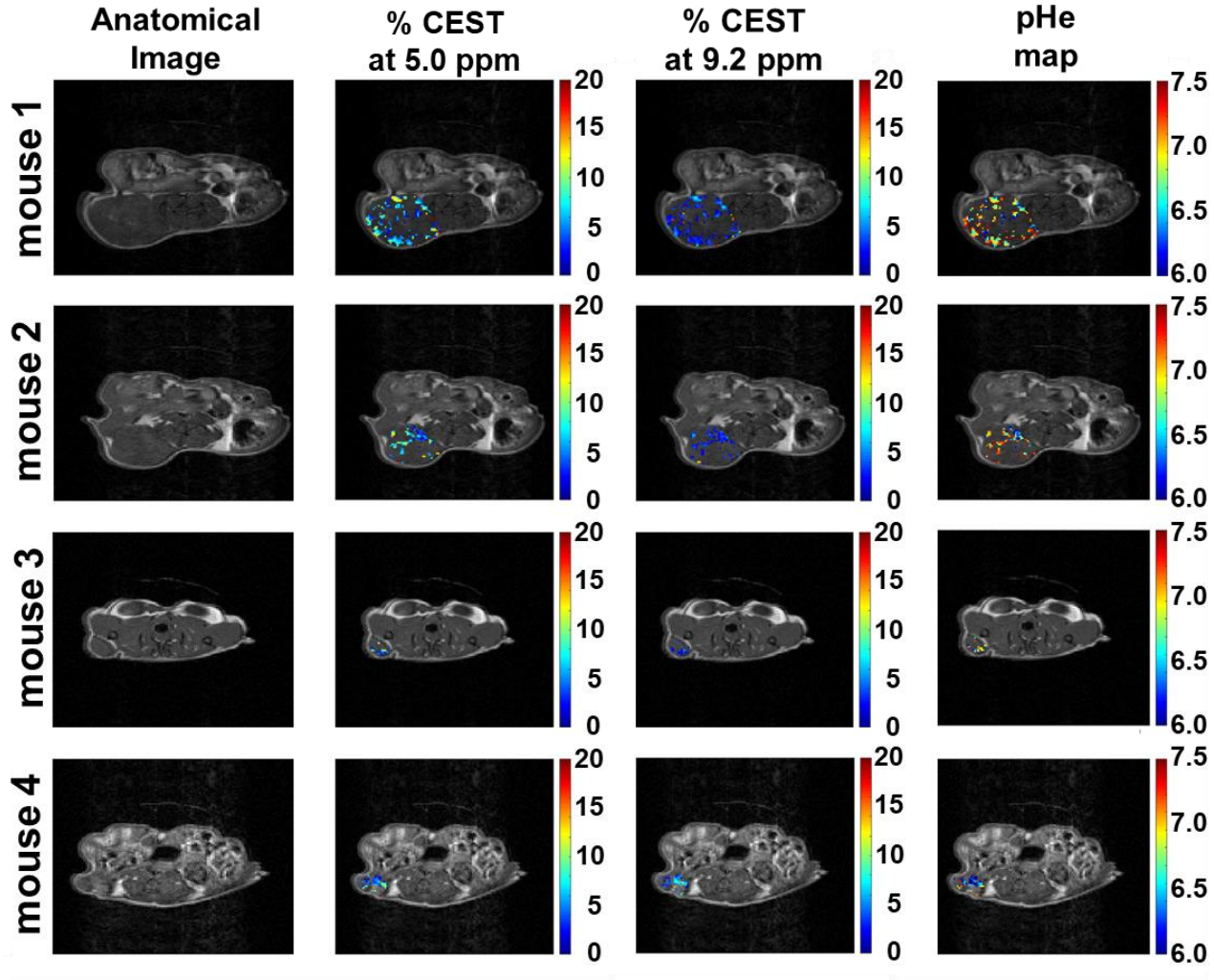

Figure A6. *In vivo* CEST MRI of a MDA-MB-231 tumor model following i.v. injection of polymer agent at a dose of 2.77 mg/kg. Anatomical images show the location of the tumor (first column). The parametric maps of % CEST signal amplitude at 5.0 ppm (second column) and 9.2 ppm (third column) demonstrate good detection of both CEST effects. The pHe maps (fourth column) show colorful pixels where two significant CEST contrast were measured and converted to pHe values.

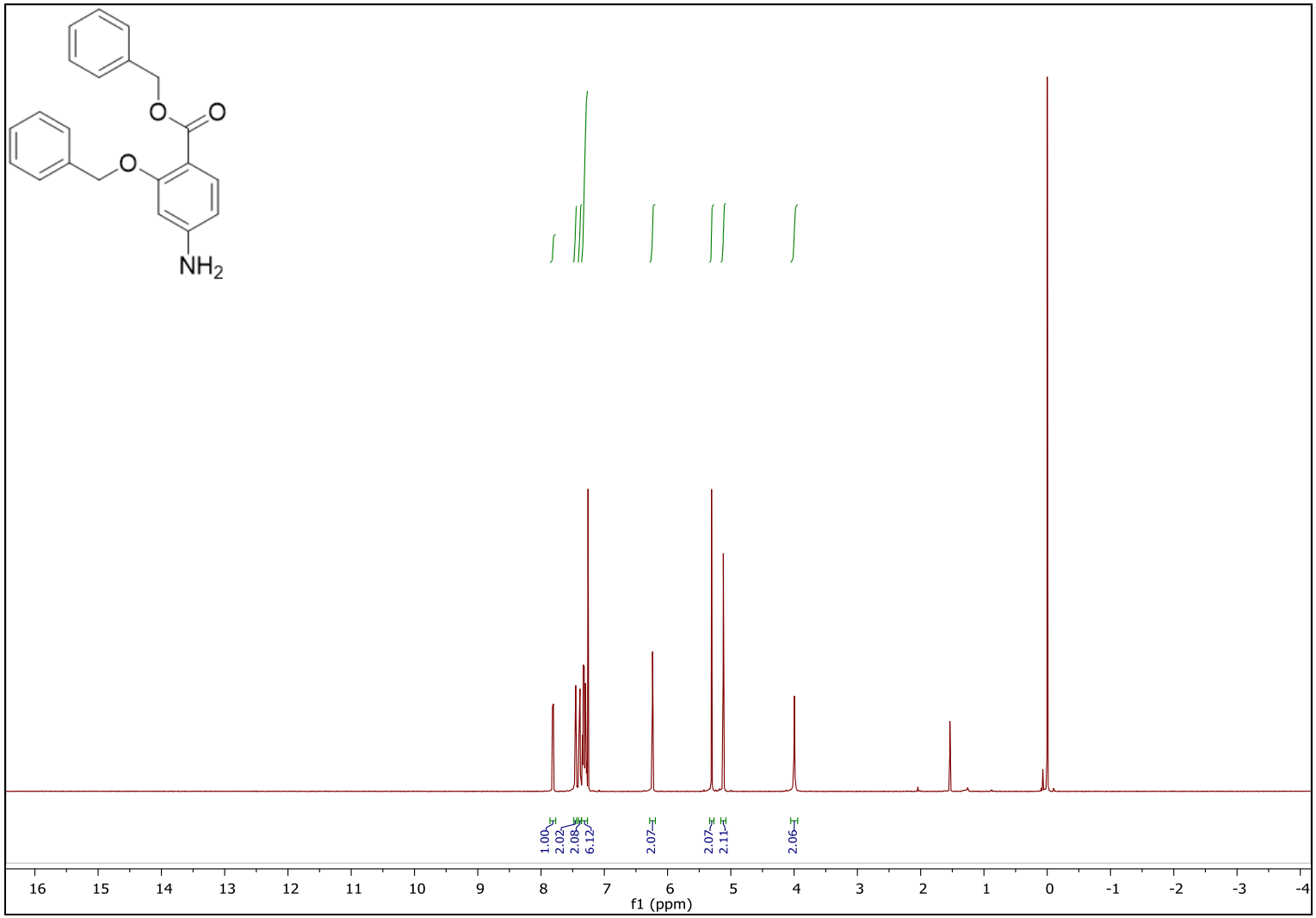

Figure A7. ^{1}H NMR of compound 1.

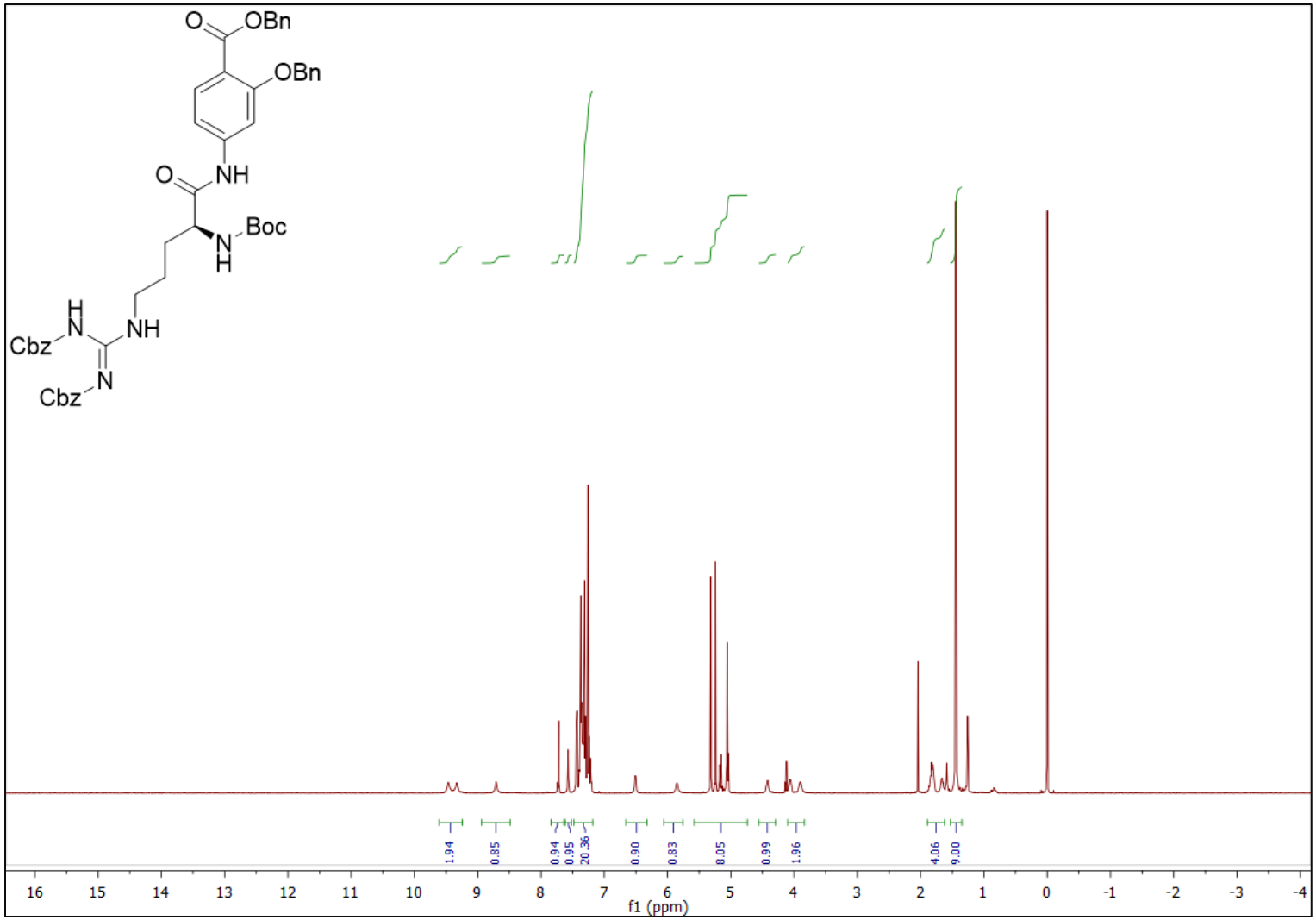

Figure A8. ^{1}H NMR of compound 2.

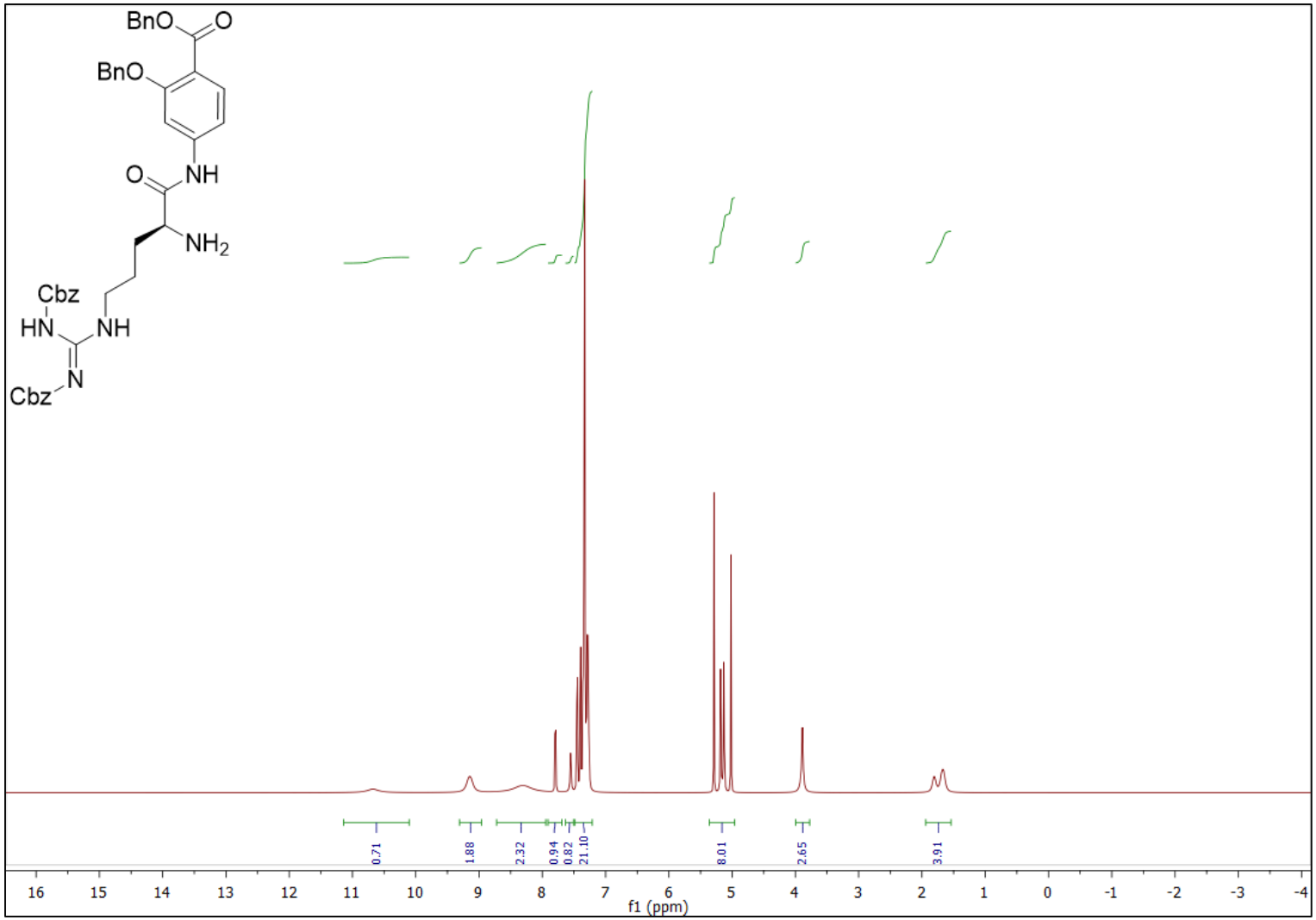

Figure A9. ^{1}H NMR of compound 3.

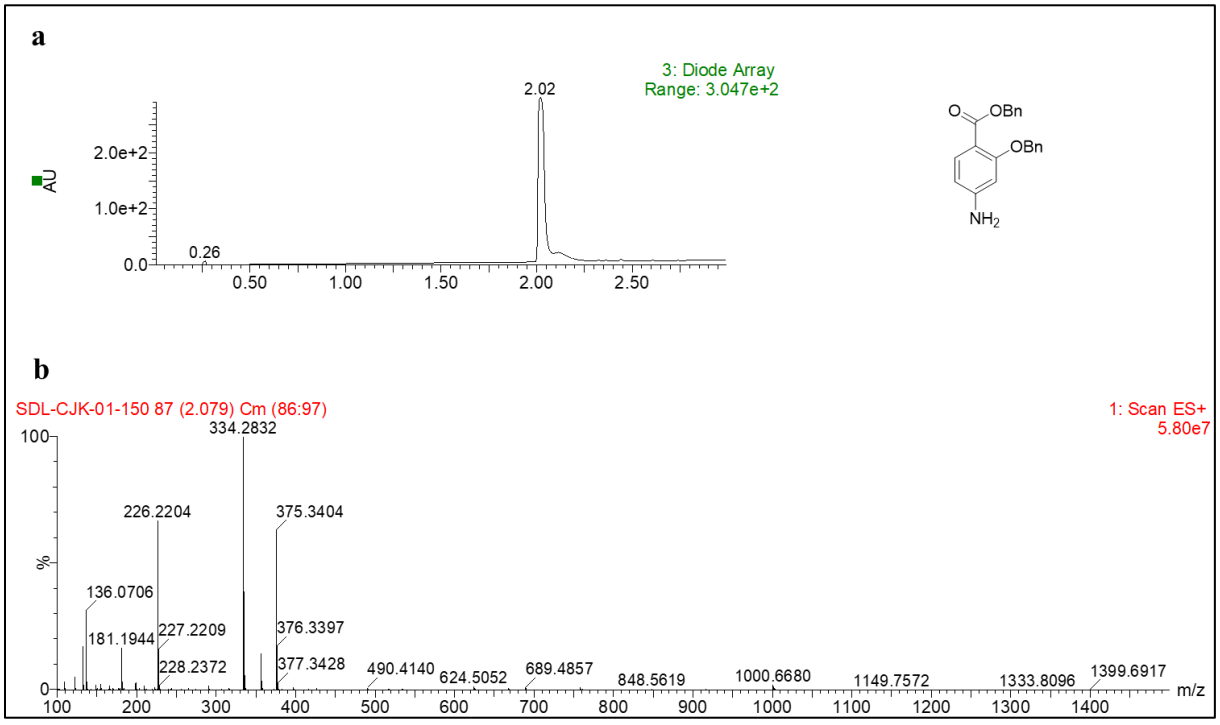

Figure A10. LC-MS analysis of compound 1. a) UPLC trace, b) ESI chromatogram

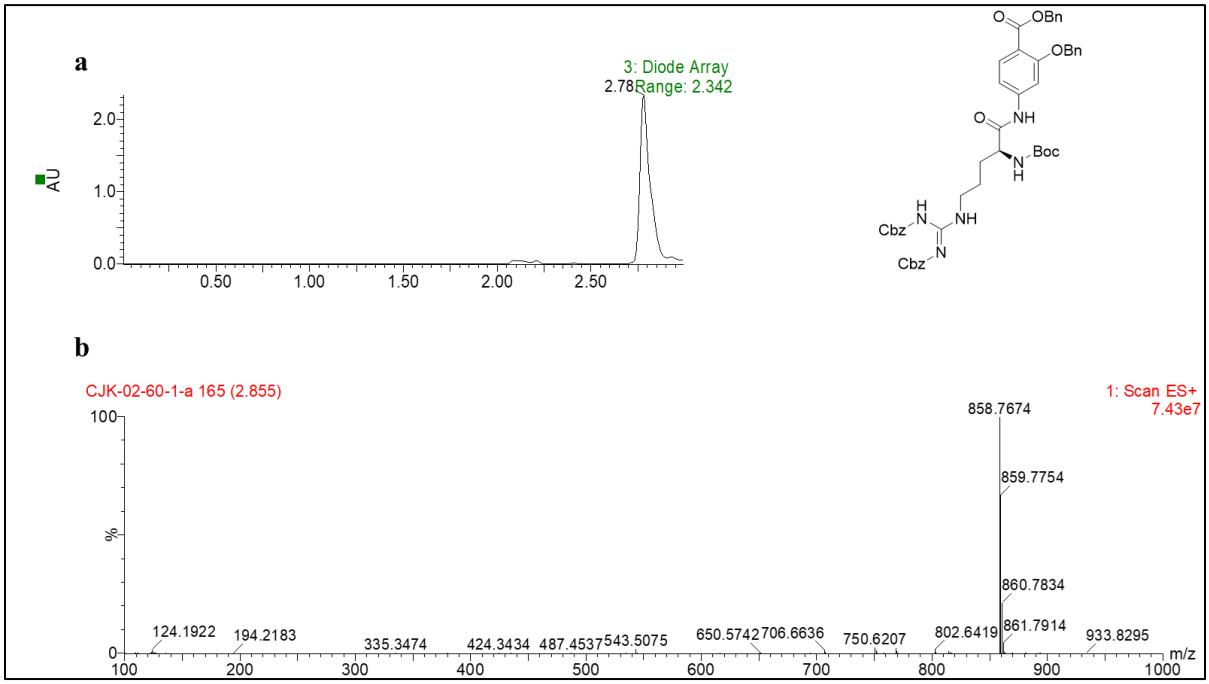

Figure A11. LC-MS analysis of compound 2. a) UPLC trace, b) ESI chromatogram

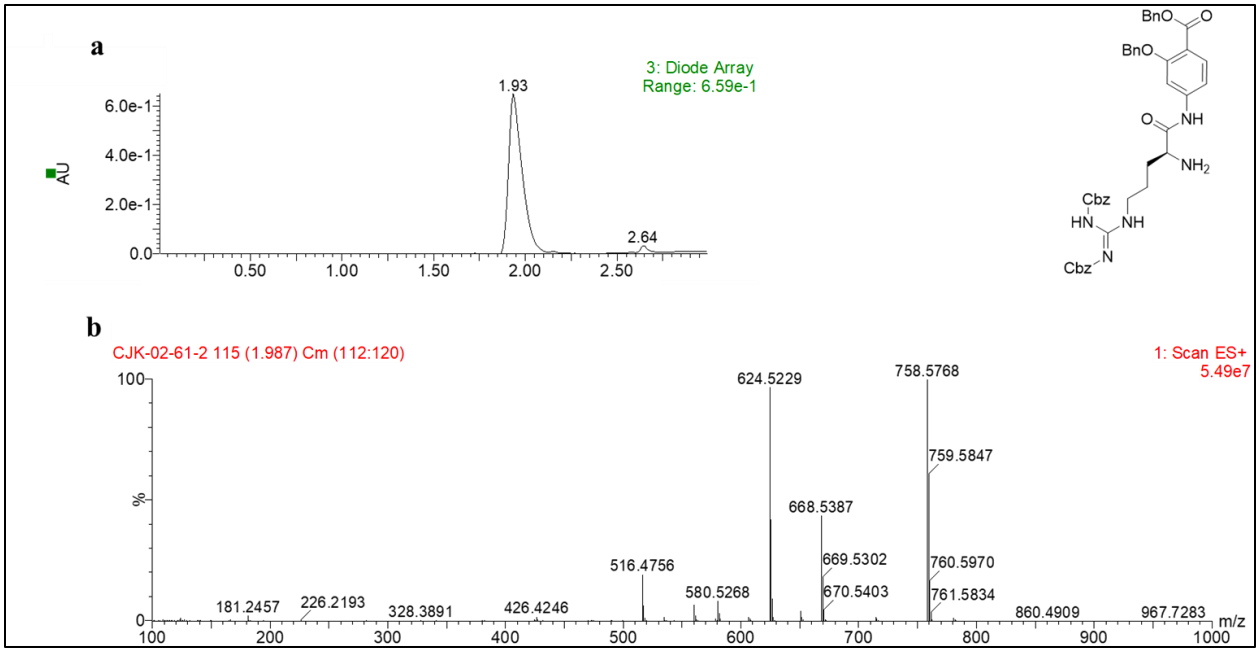

Figure A12. LC-MS analysis of compound 3. a) UPLC trace, b) ESI chromatogram

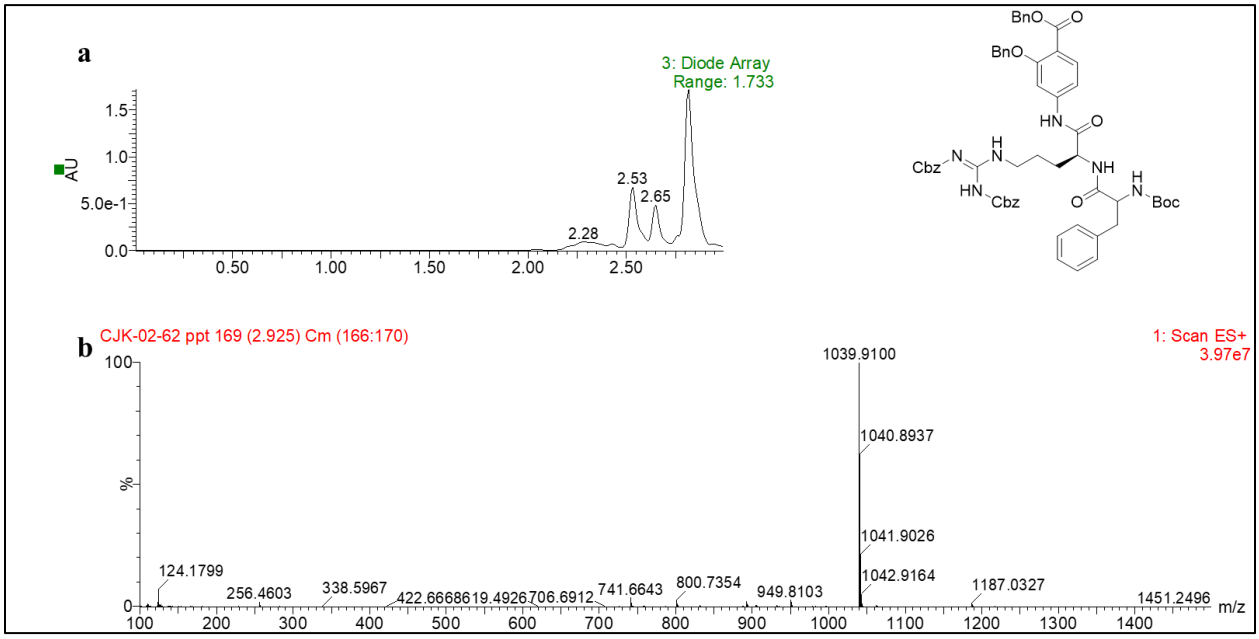

Figure A13. LC-MS analysis of compound 4. a) UPLC trace, b) ESI chromatogram

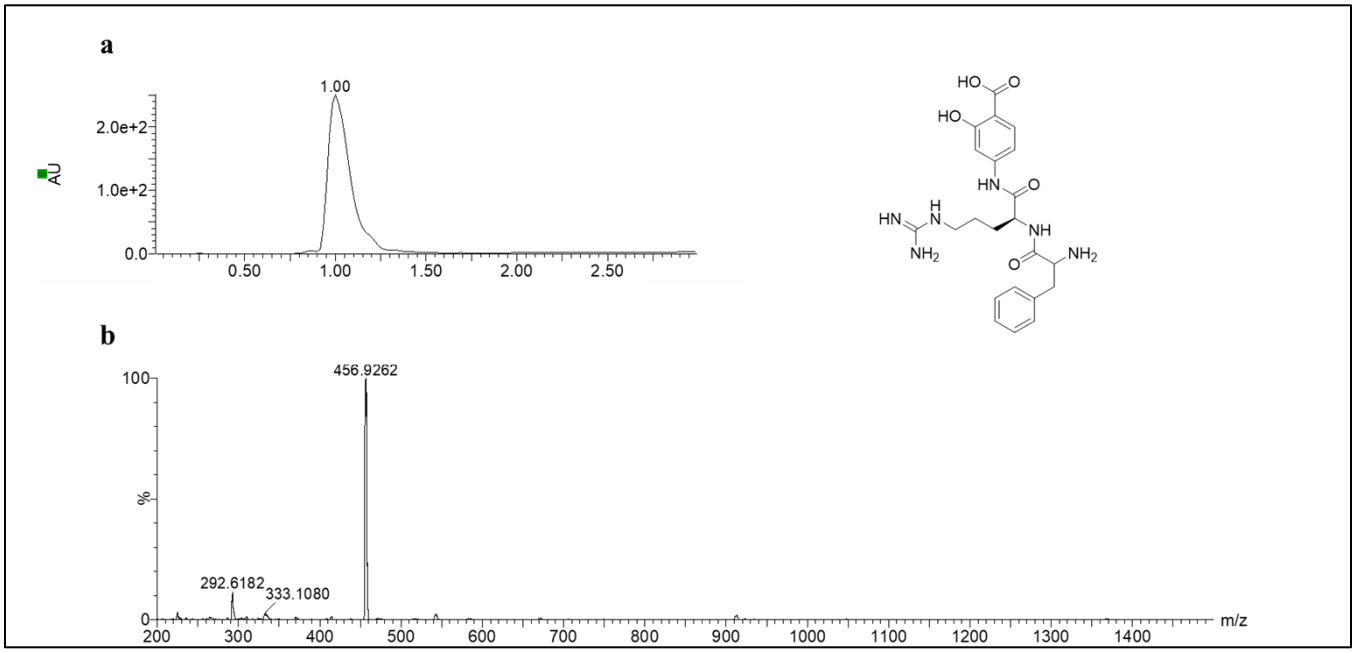

Figure A14. LC-MS analysis of compound 5 (Cathepsin B substrate). a) UPLC trace, b) ESI chromatogram

COMPREHENSIVE LIST OF REFERENCES

CHAPTER 1

1. Ward KM, Aletras AH, Balaban RS. A new class of contrast agents for MRI based on proton chemical exchange dependent saturation transfer (CEST). J Magn Reson 2000;143:79–87.
2. Hingorani DV, Bernstein AS, Pagel MD. A review of responsive MRI contrast agents: 2005–2014. Contrast Media Mol Imaging 2015;10:245–265.
3. Aime S, Caravan P. Biodistribution of gadolinium-based contrast agents, including gadolinium deposition. J Magn Reson Imaging 2009;30:1259–67.
4. Ekladious I, Colson YL, Grinstaff MW. Polymer–drug conjugate therapeutics: advances, insights and prospects. Nat Rev Drug Discov 2019;18:273–294.
5. Torchilin VP. Polymeric contrast agents for medical imaging. Curr Pharm Biotechnol 2000;1:183–215.
6. Matsumura Y, Maeda H. A New concept for macromolecular therapeutics in cancer chemotherapy: Mechanism of tumoritropic accumulation of proteins and the antitumor agent Smancs Cancer Res 1986;46:6387–6392.
7. Au JL-S, Yeung BZ, Wientjes MG, Lu Z, Wientjes MG. Delivery of cancer therapeutics to extracellular and intracellular targets: Determinants, barriers, challenges and opportunities. Adv Drug Deliv Rev 2016;97:280–301.
8. Kou L, Sun J, Zhai Y, He Z. The endocytosis and intracellular fate of nanomedicines: Implication for rational design. Asian J Pharm Sci 2013;8:1–10.
9. Sundaram KM, Zhang Y, Mitra AK, Kouadio JLK, Gwin K, Kossiakoff AA, Roman BB, Lengyel E, Piccirilli JA. Prolactin receptor–mediated internalization of imaging agents detects

epithelial ovarian cancer with enhanced sensitivity and specificity. Cancer Res 2017;77:1684–1696.

10. Kim KS, Park W, Hu J, Bae YH, Na K. A cancer-recognizable MRI contrast agent using pH-responsive polymeric micelle. Biomaterials 2014;35:337–343.
11. Tang H, Zhao W, Yu J, Li Y, Zhao C. Recent development of pH-responsive polymers for cancer nanomedicine. Molecules 2018;24:4.
12. Duncan R. The dawning era of polymer therapeutics. Nat Rev Drug Discov 2003;2:347–360.
13. Zhang X, Lin Y, Gillies RJ. Tumor pH and its measurement. J Nucl Med 2010;51:1167–70.
14. Wang B, Lv P, Cai H, Li Y, Zhu H, Lui S, Gong Q, Luo K. Enzyme-responsive copolymer as a theranostic prodrug for tumor *in vivo* imaging and efficient chemotherapy. J Biomed Nanotechnol 2019;15:1897–1908.
15. Traina CA, Bakus RC, Bazan GC. Design and synthesis of monofunctionalized, water-soluble conjugated polymers for biosensing and imaging applications. J Am Chem Soc 2011;133:12600–12607.
16. Fischer CS, Jenewein C, Mecking S. Conjugated star polymers from multidirectional Suzuki–Miyaura polymerization for live cell imaging. Macromolecules 2015;48:483–491.
17. Cao F, Huang T, Wang Y, Liu F, Chen L, Ling J, Sun J. Novel Lanthanide–polymer complexes for dye-free dual modal probes for MRI and fluorescence imaging. Polym Chem 2015;6:7949–7957.
18. Ray Banerjee S, Xong X, Yang X, Minn I, Liosk A, Chen Y, Bui A, Chatterjee S, Chen J, van Zijl PCM, McMahon MT, Pomper MG. Salicylic acid-based polymeric contrast agents for molecular magnetic resonance imaging of prostate cancer. Chem Euro J 2018;24:7235-7242.

19. Koziolová E, Goel S, Chytil P, Janoušková O, Barnhart TE, Cai W, Etrych TA. A tumor-targeted polymer theranostics platform for positron emission tomography and fluorescence imaging. Nanoscale 2017;9:10906–10918.
20. Wu Y, Zhou Y, Ouari O, Woods M, Zhao P, Soesbe TC, Kiefer GE, Sherry AD. Polymeric PARACEST agents for enhancing MRI contrast sensitivity. J Am Chem Soc 2008;130:13854–13855.
21. Liu G, Banerjee SR, Yang X, Yadav N, Lisok A, Jablonska A, Xu J, Li Y, Pomper MG, van Zijl P. A dextran-based probe for the targeted magnetic resonance imaging of tumours expressing prostate-specific membrane antigen. Nat Biomed Eng 2017;1:977–982.
22. Mehvar R. Dextrans for targeted and sustained delivery of therapeutic and imaging agents. J. Control. Release 2000;69:1–25.
23. Lesniak WG, Oskolkov N, Song X, Lal B, Yang X, Pomper M, Laterra J, Nimmagadda S, McMahon MT. Salicylic acid conjugated dendrimers are a tunable, high performance CEST MRI NanoPlatform. Nano Lett 2016;16:2248–2253.
24. Kim H, Shin M, Han S, Kwon W, Hahn SK. Hyaluronic acid derivatives for translational medicines. Biomacromolecules 2019;20:2889–2903.
25. Miki K, Inoue T, Kobayashi Y, Nakano K, Matsuoka H, Yamauchi F, Yano T, Ohe K. Near-Infrared dye-conjugated amphiphilic hyaluronic acid derivatives as a dual contrast agent for *in vivo* optical and photoacoustic tumor imaging. Biomacromolecules 2015;16:219–227.
26. Payne WM, Hill TK, Svechkarev D, Holmes MB, Sajja BR, Mohs AM. Multimodal imaging nanoparticles derived from hyaluronic acid for integrated preoperative and intraoperative cancer imaging. Contrast Media Mol Imaging 2017;2017:9616791.

27. Grull H, Langereis S, Messager L, Castelli DD, Sanino A, Torres E, Terreno E, Aime S. Block Copolymer vesicles containing paramagnetic lanthanide complexes: a novel class of t1- and CEST MRI contrast agents. Soft Matter 2010;6:4847–4850.
28. Jones KM, Pollard AC, Pagel MD. Clinical applications of chemical exchange saturation transfer (CEST) MRI. J Magn Reson Imaging 2018;47:11-27.
29. Hingorani DV, Montano LA, Randtke EA, Lee YS, Cárdenas-Rodríguez J, Pagel MD. A single diamagnetic catalyCEST MRI contrast agent that detects cathepsin b enzyme activity by using a ratio of two CEST signals. Contrast Media Mol Imaging 2016;11:130–138.
30. Chen LQ, Howison CM, Jeffery JJ, Robey IF, Kuo PH, Pagel MD. Evaluations of extracellular pH within *in vivo* tumors using AcidoCEST MRI. Magn Reson Med 2014;72:1408–1417.
31. Yang X, Song X, Li Y, Liu G, Ray Banerjee S, Pomper MG, McMahon MT. Salicylic acid and analogues as diaCEST MRI contrast agents with highly shifted exchangeable proton frequencies. Angew Chem Int Ed 2013;52:8116–8119.
32. Wu B, Warnock G, Zaiss M, Lin C, Chen M, Zhou Z, Mu L, Nanz D, Tuura R, Delso G. An overview of CEST MRI for non-MR physicists. EJNMMI Phys 2016;3:19.
33. Hancu I, Dixon WT, Woods M, Vinogradov E, Sherry AD, Lenkinski RE. CEST and PARACEST MR contrast agents. Acta Radiol 2010;51:910–23.
34. Kuo PH. Gadolinium-containing MRI contrast agents: Important variations on a theme for NSF. J Am Coll Radiol 2008;5:29–35.
35. Jenkins W, Perone P, Walker K, Bhagavathula N, Aslam MN, DaSilva M, Dame MK, Varani J. Fibroblast response to lanthanoid metal ion stimulation: Potential contribution to fibrotic tissue injury. Biol Trace Elem Res 2011;144:621–35.

36. Wu Y, Evbuomwan M, Melendez M, Opina A, Sherry AD. Advantages of macromolecular to nanosized chemical-exchange saturation transfer agents for MRI applications. Future Med Chem 2010;2:351–66.
37. Burdinski D, Pikkemaat JA, Emrullahoglu M, Costantini F, Verboom W, Langereis S, Grüll H, Huskens J. Targeted lipoCEST contrast agents for magnetic resonance imaging: alignment of aspherical liposomes on a capillary surface. Angew Chem Int Ed 2010;49:2227–2229.
38. Wu Y, Carney CE, Denton M, Hart E, Zhao P, Streblow DN, Sherry AD, Woods M. Polymeric PARACEST MRI contrast agents as potential reporters for gene therapy. Org Biomol Chem 2010;8:5333–5338.
39. Wu Y, Zhao P, Kiefer GE, Sherry AD. Multifunctional polymeric scaffolds for enhancement of PARACEST contrast sensitivity and performance: effects of random copolymer variations. Macromolecules 2010;43:6616–6624.
40. Goffeney N, Bulte JWM, Duyn J, Bryant LH, van Zijl PCM. Sensitive NMR detection of cationic-polymer-based gene delivery systems using saturation transfer via proton exchange. J Am Chem Soc 2001;123:8628–8629.
41. McMahon MT, Gilad AA, DeLiso MA, Cromer Berman SM, Bulte JWM, van Zijl PCM. New "Multicolor" polypeptide diamagnetic chemical exchange saturation transfer (DIACEST) Contrast Agents for MRI. Magn Reson Med 2008;60:803–812.
42. Snoussi K, Bulte JWM, Guéron M, van Zijl PCM. Sensitive CEST agents based on nucleic acid imino proton exchange: detection of poly(rU) and of a dendrimer-poly(rU) model for nucleic acid delivery and pharmacology. Magn Reson Med 2003;49:998–1005.

43. Li Y, Qiao Y, Chen H, Bai R, Staedtke V, Han Z, Xu J, Chan KWY, Yadav N, Bulte JWM, Zhou S, van Zijl PCM, Liu G. Characterization of tumor vascular permeability using natural dextrans and CEST MRI. Magn Reson Med 2017;79:1001-1009.
44. Pikkemaat JA, Wegh RT, Lamerichs R, van de Molengraaf RA, Langereis S, Burdinski D, Raymond AYF, Janssen HM, de Waal BFM, Willard NP, Meijer EW, Grull H. Dendritic PARACEST contrast agents for magnetic resonance imaging. Contrast Media Mol Imaging 2007;2:229–239.
45. Ali MM, Liu G, Shah T, Flask CA, Pagel MD. Using two chemical exchange saturation transfer magnetic resonance imaging contrast agents for molecular imaging studies. Acc Chem Res 2009;42:915–924.
46. Ali MM, Bhuiyan MPI, Janic B, Varma NRS, Mikkelsen T, Weing JR, Knight RA, Pagel MD, Arbab AS. A nano-Sized PARACEST-fluorescence imaging contrast agent facilitates and validates *in vivo* CEST MRI detection of glioma. Nanomedicine 2012;7:1827-1837.
47. Ali MM, Yoo B, Pagel MD. Tracking the relative *in vivo* pharmacokinetics of nanoparticles with PARACEST MRI. Mol Pharm 2009;6:1409–1416.
48. Ali MM, Woods M, Suh EH, Kovacs Z, Tircsó G, Zhao P, Kodibagkar VD, Sherry AD. Albumin-binding paraCEST agents. J Biol Inorg Chem 2007;12:855–865.
49. Evbuomwan OM, Merritt ME, Kiefer GE, Dean Sherry A. Nanoparticle-based PARACEST agents: the quenching effect of silica nanoparticles on the CEST signal from surface-conjugated chelates. Contrast Media Mol Imaging 2012;7:19–25.

CHAPTER 2

1. Warburg O. On the origin of cancer cells. Science 1956;123:309-314.

2. Vander Heiden MG, Cantley LC Thompson CB. Understanding the Warburg effect: the metabolic requirements of cell proliferation. Science 2009;324:1029-1033.
3. Hanahan D, Weinberg RA. Hallmarks of cancer: the next generation. Cell 2011;144:646-674.
4. Chen LQ, Pagel MD. Evaluating pH in the extracellular microenvironment using CEST MRI and other imaging methods. Adv Radiol 2015;206405.
5. Estrella V, Chen T, Lloyd M, Wojtkowiak J, Cornnell HH, Ibrahim-Hashim A, Bailey K, Balagurunathan Y, Rothberg JM, Sloane BL, Johnson J, Gatenby RA, Gillies RJ. Acidity generated by the tumor microenvironment drives local invasion. Cancer Res 2013;73:1524-1535.
6. Akhenblit PJ, Pagel MD. Recent advances in targeting tumor energy metabolism with tumor acidosis as a biomarker of drug efficacy. J Cancer Sci Ther 2016;8:20-29.
7. Ward KM, Aletras AH, Balaban RS. A new class of contrast agents for MRI based on proton chemical exchange dependent saturation transfer (CEST). J Magn Reson 2000;143:79-87.
8. Jones KM, Pollard AC, Pagel MD. Clinical applications of chemical exchange saturation transfer (CEST) MRI. J Magn Reson Imaging 2018;47:11-27.
9. Chen LQ, Howison CM, Jeffery JJ, Robey IF, Kuo PH, Pagel MD. Evaluations of extracellular pH within *in vivo* tumors using acidoCEST MRI. Magn Reson Med 2014;72:1408-1417.
10. Liu G, Li Y, Sheth VR, Pagel MD. Imaging *in vivo* extracellular pH with a single PARACEST MRI contrast agent. Molec Imaging 2012;11:47-57.
11. Sheth VR, Li Y, Chen LQ, Howison CM, Flask CA, Pagel MD. Measuring *in vivo* tumor pHe with CEST-FISP MRI. Magn Reson Med 2012;67:760–768.
12. Sheth VR, Liu G, Li Y, Pagel MD. Improved pH measurements with a single PARACEST MRI contrast agent. Contrast Media Mol Imaging 2012;7:26–34.

13. Chen LQ, Howison CM, Spier C, Stopeck AT, Malm SW, Pagel MD, Baker AF. Assessment of carbonic anhydrase IX expression and extracellular pH in B-cell lymphoma cell line models. Leuk Lymphoma 2015;56:1432-1439.
14. Jones KM, Randtke EA, Howison CM, Cárdenas-Rodríguez J, Sime PJ, Kottmann RM, Pagel MD. Measuring extracellular pH in a lung fibrosis model with acidoCEST MRI. Molec Imaging Biol 2015;17:177-184.
15. Chen LQ, Randtke EA, Jones KM, Moon BF, Howison CM, Pagel MD. Evaluations of tumor acidosis within *in vivo* tumor models using parametric maps generated with acidoCEST MRI. Mol Imaging Biol 2015;17:488-496.
16. Chen Z, Li Y, Airan R, Han Z, Xu J, Chan KWY, Xu Y, Bulte JWM, van Zijl, PCM, McMahon, MT, Zhou S, Liu G. CT and CEST MRI bimodal imaging of the intratumoral distribution of iodinated liposomes. Quant Imaging Med Surg 2019;9:1579-1591
17. Moon BF, Jones KM, Chen LQ, Liu P, Randtke EA, Howison CM, Pagel MD. A comparison of iopromide and iopamidol, two acidoCEST MRI contrast media that measure tumor extracellular pH. Contrast Media Mol Imaging 2015;10:446-455.
18. Jones KM, Randtke EA, Howison CM, Pagel MD. Respiration gating and Bloch fitting improve pH measurements with acidoCEST MRI in an ovarian orthotopic tumor model. Proc SPIE 2016;9788:978815.
19. Akhenblit PJ, Hanke NT, Gill A, Persky DO, Howison CM, Pagel MD, Baker AF. Assessing metabolic changes in response to mTOR inhibition in a Mantle cell lymphoma xenograft model using acidoCEST MRI. Mol Imaging 2016;15:1536012116645439.
20. Randtke EA, Granados JC, Howison CM, Pagel MD, Cárdenas-Rodríguez J. Multislice CEST MRI improves the spatial assessment of tumor pH. Magn Reson Med 2017;78:97-106.

21. Jones KM, Stuehm CA, Hsu CC, Kou PH, Pagel MD, Randke EA. Imaging lung cancer by using chemical exchange saturation transfer MRI with retrospective respiration gating. Tomography 2017;3:201-210.
22. Li X, Shepard HM, Cowell JA, Zhao C, Osgood RJ, Rosengren S, Blouw B, Garrovillo SA, Pagel MD, Whatcott CJ, Han H, Von Hoff DD, Labarre MJ, Maneval DC, Thompson CT. Parallel accumulation of tumor hyaluronan, collagen and smooth muscle actin and the adapting tumor microenvironment. Clin Cancer Res 2018;24:4798-4807.
23. Lindeman LR, Randtke EA, High RA, Jones KM, Howison CM, Pagel MD. A comparison of exogenous and endogenous CEST MRI methods for evaluating *in vivo* pH. Magn Reson Med 2018;79:2766-2772.
24. High RA, Randtke, EA, Jones KM, Lindeman LR, Ma JC, Zhang S, DeRoux LG, Pagel MD. Extracellular acidosis differentiates pancreatitis and pancreatic cancer in mouse models using acidoCEST MRI. Neoplasia 2019;21:1085-1090.
25. Som A, Raiya R, Paranandi K, High RA, Reed N, Beeman SC, Brandenburg M, Sudlow G, Prior JL, Akers W, Mah-Som AY, Habimana-Griffin L, Garbow J, Ippolito JE, Pagel MD, Biswas P, Achilefu S. Calcium carbonate nanoparticles stimulate tumor metabolic reprogramming and modulate tumor metastasis. Nanomedicine 2019;14:169-182.
26. Lindeman LR, Jones KM, High RA, Howison CM, Schubitz LF, Pagel MD. Differentiating lung cancer and infection based on measurements of extracellular pH with acidoCEST MRI. Sci Rep 2019;9:13002.
27. Minhas AS, Sharkey J, Randtke EA, Murray P, Wilm B, Pagel MD, Poptani H. Measuring kidney perfusion and renal clearance consecutively using MRI and multispectral optoacoustic tomography. Mol Imaging Biol 2019, *Epub ahead of print*.

28. Jones KM, Randtke EA, Yoshimaru E, Howison CM, Chalasani P, Klein RR, Chambers SK, Kuo PH, Pagel MD. Clinical translation of tumor acidosis measurements with acidoCEST MRI. Molec Imaging Biol 2017;19:617-625.
29. Aime S, Barge A, Delli Castelli D, Fedeli F, Mortillaro A, Nielsen FU, Terreno E. Paramagnetic lanthanide(III) complexes as pH-sensitive chemical exchange saturation transfer (CEST) contrast agents for MRI applications. Magn Reson Med 2002;47:639–648.
30. Aime S, Delli Castelli D, Terreno E. Novel pH-reporter MRI contrast agents. Angewandte Chemie Int Ed 2002;41:4334–4336.
31. Terreno E, Delli Castelli D, Cravotto G, Milone L, Aime S. Ln(III)-DOTAMGly complexes: A versatile series to assess the determinants of the efficacy of paramagnetic chemical exchange saturation transfer agents for magnetic resonance imaging applications. Invest Radiol 2002;39:235-243.
32. Delli Castelli D, Terreno E, Aime S. Yb(III)-HPDO3A: a dual pH- and temperature-responsive CEST agent. Angewandte Chemie Int Ed 2011:50:1798–1800.
33. Krchova T, Galisova A, Jirak D, Hermann P, Kotek J. Ln(III)-complexes of a DOTA analogue wth an ethylenediamine pendant arm as pH-responsive PARACEST contrast agents. Dalton Trans 2016;45:3486-3496.
34. Thorarinsdottir AE, Du K, Collins JHP, Harris TD. Ratiometric pH imaging with a Co^{II}_2 MRI probe via CEST effects of opposing pH dependencies. J Am Chem Soc 2017;139:15836-15847.
35. Ward KM, Balaban RS. Determination of pH using water protons and chemical exchange dependent saturation transfer (CEST). Magn Reson Med 2000;44:799-802.

36. Longo DL, Dastru W, Digilio G, Keupp J, Langereis S, Lanzardo S, Prestigio S, Steinbach O, Terreno E, Uggeri F, Aime S. Iopamidol as a responsive MRI-chemical exchange saturation transfer contrast agent for pH mapping of kidneys: *In vivo* studies in mice at 7 T. Magn Reson Med 2011;65:202–211.
37. Longo DL, Busato A, Lanzardo S, Antico F, Aime S. Imaging the pH evolution of an acute kidney injury model by means of iopamidol, a MRI-CEST pH-responsive contrast agent. Magn Reson Med 2013;70:859–864.
38. Sun PZ, Longo DL, Hu W, Xiao G, Wu R. Quantification of iopamidol multi-site chemical exchange properties for ratiometric chemical exchange saturation transfer (CEST) imaging of pH. Phys Med Biol 2014;59:4493–4504.
39. Muller-Lutz A, Khalil N, Schmitt B, Jellus V, Pentang G, Oeltzschner G, Antoch G, Lanzman RS, Wittsack HJ. Pilot study of Iopamidol-based quantitative pH imaging on a clinical 3T MR scanner. MAGMA 2014;27:477–485.
40. Delli Castelli D, Ferrauto G, Cutrin JC, Terreno E, Aime S. *In vivo* maps of extracellular pH in murine melanoma by CEST-MRI. Magnetic Reson Med 2014;71;326–332.
41. Longo DL, Bartoli A, Consolino L, Bardini P, Arena F, Schwaiger M, Aime S. *In vivo* imaging of tumor metabolism and acidosis by combining PET and MRI-CEST pH imaging. Cancer Res 2016;76:6463–6470.
42. Yang X, Song X, Ray Banerjee S, Li Y, Byun Y, Liu G, Bhujwalla ZM, Pomper MG, McMahon MT. Developing imidazoles as CEST MRI pH sensors. Contrast Media Mol Imaging 2016;11:304–312.
43. Longo DL, Cutrin JC, Michelotti F, Irrera P, Aime S. Noninvasive evaluation of renal pH homeostasis after ischemia reperfusion injury by CEST-MRI. NMR Biomed 2017;30:e3720

44. Anemone A, Consolino L, Conti L, Reineri F, Cavallo F, Aime S, Longo DL. *In vivo* evaluation of tumour acidosis for assessing the early metabolic response and onset of resistance to dichloroacetate by using magnetic resonance pH imaging. Int J Oncol 2017;51:498–506.

45. Ferrauto G, Di Gregorio E, Auboiroux V, Petit M, Berger F, Aime S. CEST-MRI for glioma pH quantification in mouse model: validation by immunohistochemistry. NMR Biomed 2018;31:e4005.

46. Longo DL, Sun PZ, Consolino L, Michelotti FC, Uggeri F, Aime S. A general MRI-CEST ratiometric approach for pH imaging: demonstration of *in vivo* pH mapping with iobitridol. J Am Chem Soc 2014;136:14333-14336.

47. Chen M, Chen C, Shen Z, Zhang S, Zhang X, Chen Y, Lin F, Ma X, Zhuang C, Mao Y, Gan H, Chen P, Zong X, Wu R. Extracellular pH is a biomarker enabling detection of breast cancer and liver cancer using CEST MRI. Oncotarget 2017;8:45759-45767.

48. Wu R, Longo DL, Aime S, Sun PZ. Quantitative description of radiofrequency (RF) power-based ratiometric chemical exchange saturation transfer (CEST) pH imaging. NMR Biomed 2015;28:555-565.

49. Wu Y, Zhou IY, Igarashi T, Longo DL, Aime S, Sun PZ. A generalized ratiometric chemical exchange saturation transfer (CEST) MRI approach for mapping renal pH using iopamidol. Magn Reson Med 2018;79:1553-1558.

50. Ma YJ, High RA, Tang Q, Wan L, Jerban S, Du J, Change EY. AcidoCEST-UTE MRI for the assessment of extracellular pH of joint tissues at 3 T. Invest Radiol 2019;54:565-571.

51. High RA, Ji Y, Ma YJ, Tang Q, Murphy ME, Du J, Chang EY. *In vivo* assessment of extracellulr pH of joint tissues using acidoCEST-UTE MRI. Quant Imaging Med Surg 2019;9:1664-1673.

52. Aime S, Delli Castelli D, Terreno E. Supramolecular adducts between poly-L-arginine and [TmIIIdotp]: A aoute to sensitivity-enhanced magnetic resonance imaging–chemical exchange saturation transfer agents. Angew Chem Int Ed 2003:42;4527–4529.

53. Ali MM, Woods M, Suh EH, Kovacs Z, Tircsó G, Zhao P, Kodibagkar VD, Sherry AD. Albumin-binding paraCEST agents. J Biol Inorg Chem 2007;12:855–865.

54. Pikkemaat JA, Wegh RT, Lamerichs R, van de Molengraaf RA, Langereis S, Burdinski D, Raymond AYF, Janssen HM, de Waal BFM, Willard NP, Meijer EW, Grull H. Dendritic PARACEST contrast agents for magnetic resonance imaging. Contrast Media Mol Imaging 2007;2:229–239.

55. Vasalatiy O, Gerard D, Zhao P, Sun X, Sherry AD. Labeling of adenovirus particles with paraCEST agents. Bioconjug Chem 2008;19:598–606.

56. Wu Y, Zhou Y, Ouari O, Woods M, Zhao P, Soesbe TC, Kiefer GE, Sherry AD. Polymeric PARACEST agents for enhancing MRI contrast sensitivity. J Am Chem Soc 2008; 130:13854–13855.

57. Ali MM, Liu G, Shah T, Flask CA, Pagel MD. Using two chemical exchange saturation transfer magnetic resonance imaging contrast agents for molecular imaging studies. Acc Chem Res 2009:42;915–924.

58. Ali MM, Yoo B, Pagel MD. Tracking the relative *in vivo* pharmacokinetics of nanoparticles with PARACEST MRI. Mol Pharm 2009;6:1409-1416.

59. Wu Y, Carney CE, Denton M, Hart E, Zhao P, Streblow DN, Sherry AD, Woods M. Polymeric PARACEST MRI contrast agents as potential reporters for gene therapy. Org Biomol Chem 2010;8:5333–5338.

60. Wu Y, Zhao P, Kiefer GE, Sherry AD. Multifunctional polymeric scaffolds for enhancement of PARACEST contrast sensitivity and performance: Effects of random copolymer variations. Macromolecules 2010;43:6616–6624.
61. Ali MM, Bhuiyan MPI, Janic B, Varma NRS, Mikkelsen T, Weing JR, Knight RA, Pagel MD, Arbab AS. A nano-sized PARACEST-fluorescence imaging contrast agent facilitates and validates *in vivo* CEST MRI detection of glioma. Nanomedicine 2012;7:1827-1837.
62. Evbuomwan ON, Merritt EM, Kiefer GE. Nanoparticle-based paraCESTagents: the quenching effect of silica nanoparticles on the CEST signal from surface-conjugated chelates. Contrast Media Mol Imaging 2012;7:19–25.
63. Zhang S, Zhou K, Huang G, Takahashi M, Sherry AD, Gao J. A novel class of polymeric pH-responsive MRI CEST agents. Chem Comm 2013;49:6418-6420.
64. Goffney N, Bulte JW, Dyun J, Bryant LH, van Zijl PC. Sensitive NMR detection of cationic polymer-based gene delivery systems using saturation transfer via proton exchange. J Am Chem Soc 2001;123:8628-8629.
65. Snoussi K, Bulte JWM, Guéron M, Van Zijl PCM. Sensitive CEST agents based on nucleic acid imino proton exchange: detection of poly(rU)and of a dendrimer-poly(rU) model for nucleic acid delivery and pharmacology. Magn Reson Med 2003;49(6):998–1005.
66. McMahon MT, Gilad AA, Zhou JY, Sun PZ, Bulte JWM, van Zijl PCM. Quantifying exchange rates in chemical exchange saturation transfer agents using the saturation time and saturation power dependencies of the magnetization transfer effect on the magnetic resonance imaging signal (QUEST and QUESP): pH calibration for poly-L-lysine and a starburst dendrimer. Magn Reson Med 2006;55:836-847.

67. McMahon MT, Gilad AA, DeLiso MA, Cromer Berman SM, Bulte JWM, van Zijl PCM. New "multicolor" polypeptide diamagnetic chemical exchange saturation transfer (DIACEST) contrast agents for MRI. Magn Reson Med 2008;60:803–812.

68. Choi J, Kim K, Kim T, Liu G, Bar-Shir A, Hyeon T, McMahon MT, Bulte JW, Fisher JP, Gilad AA. Multimodal imaging of sustained drug release from 3-D poly(propylene fumarate) (PPF) scaffolds. J Control Release 2011;156:239-245.

69. Haris M, Singh A, Mohanmmed I, Ittyerah R, Nath K, Nanga RP, Debrosse C, Kogan F, Cai K, Poptani H, Reddy D, Hariharan H, Reddy R. *In vivo* magnetic resonance imaging of tumor protease activity. Sci Rep 2014;4:6081.

70. Lesniak WG, Oskolkov N, Song X, Lal B, Yang X, Pomper M, Laterra J, Nimmagadda S, McMahon MT. Salicylic acid conjugated dendrimers are a tunable, high performance CEST MRI nanoplatform. Nano Lett 2016;16:2248–2253.

71. Li Y, Qiao Y, Chen H, Bai R, Staedtke V, Han Z, Xu J, Chan KWY, Yadav N, Bulte JWM, Zhou S, van Zijl PCM, Liu G. Characterization of tumor vascular permeability using natural dextrans and CEST MRI. Magn Reson Med 2017;79:1001-1009.

72. Liu G, Banerjee SR, Yang X, Yadav N, Lisok A, Jablonska A, Xu J, Li Y, Pomper MG, van Zijl P. A dextran-based probe for the targeted magnetic resonance imaging of tumours expressing prostate-specific membrane antigen. Nat Biomed Eng 2017;1:977–982.

73. Ray Banerjee S, Xong X, Yang X, Minn I, Liosk A, Chen Y, Bui A, Chatterjee S, Chen J, van Zijl PCM, McMahon MT, Pomper MG. Salicylic acid-based polymeric contrast agents for molecular magnetic resonance imaging of prostate cancer. Chem Euro J 2018;24:7235-7242.

74. Kuo PH, Kanal E, Abu-Alfa A, Cowper S. Gadolinium-based MRI contrast agents and Nephrogenic Systemic Fibrosis**.** Radiology 2011;242:647-649.

75. Lee A, Huang W-H, Chu C-H, Chang W-L, Yao C-W, Chen I-L. 4,5-Diamino-3-Halo-2-Hydroxybenzoic Acid Derivatives and Preparations Thereof. US 2012/0101157 A1, 2012.
76. Kennedy JF, Barker SA, Epton J, Kennedy GR. Poly-(4-and 5-acrylamidosalicylic acids). Part I. preparation and properties. J Chem Soc Perkin Trans 1 1973;0:488–490.
77. Yang X, Song X, Li Y, Liu G, Ray Banerjee S, Pomper MG, McMahon MT. Salicylic acid and analogues as diaCEST MRI contrast agents with highly shifted exchangeable proton frequencies. Angew Chemie Int Ed 2013;52:8116-8119.
78. Hingorani DV, Montano LA, Randtke EA, Lee YS, Cárdenas-Rodríguez J, Pagel MD. A single diamagnetic catalyCEST MRI contrast agent that detects cathepsin B enzyme activity by using a ratio of two CEST signals. Contrast Media Mol Imaging 2016;11:130-138.
79. Fernández-Cuervo G, Tucker KA, Malm SW, Jones KM, Pagel MD. Diamagnetic imaging agents with a modular chemical design for quantitative detection of β-galactosidase and β-glucuronidase activities with catalyCEST MRI. Bioconjug Chem 2016, 27:2549-2557.
80. Sinharay S, Randtke EA, Jones KM, Howison CM, Chambers SK, Kobayashi H, Pagel MD. Noninvasive detection of enzyme activity in tumor models of human ovarian cancer using catalyCEST MRI. Magn Reson Med 2017;77:2005-2014.
81. Sinharay S, Howison CM, Baker AF, Pagel MD. Detecting *in vivo* urokinase Plasminogen Activator activity with a catalyCEST MRI contrast agent. NMR Biomed 2017;30:e3721.
82. Sinharay S, Randtke EA, Howison CM, Ignatenko NA, Pagel MD. Detection of enzyme activity and inhibition during studies in solution, *in vitro* and *in vivo* with catalyCEST MRI. Molec Imaging Biol 2018;20:240-248.

83. Randtke EA, Chen LQ, Corrales LR, Pagel MD. The Hanes-Woolf Linear QUESP method improves the measurements of fast chemical exchange rates with CEST MRI. Magn Reson Med 2014;71:1603–1612.
84. Randtke EA, Chen LQ, Pagel MD. The reciprocal linear QUEST analysis method facilitates the measurements of chemical exchange rates with CEST MRI. Contrast Media Mol Imaging 2014;9:252–258.
85. Li Y, Sheth VR, Liu G, Pagel MD. A self-calibrating PARACEST MRI contrast agent that detects esterase enzyme activity. Contrast Media Mol Imaging 2011;6:219-228.
86. Ralford DS, Fisk CL, Becker ED. Calibration of methanol and ethylene glycol nuclear magnetic resonance thermometers. Anal Chem 1979;51:2050-2051.
87. Shah T, Lu L, Dell K, Pagel MD, Griswold M, Flask CA. CEST-FISP: A novel technique for rapid chemical exchange saturation transfer (CEST) MRI at 7T. Magn Reson Med 2011;65:432–437.
88. Liu G, Li Y, Pagel MD. Design and characterization of new irreversible responsive PARACEST MRI contrast agent that detects nitric oxide. Magn Reson Med 2007;58:1249-1256.

CHAPTER 3

1. Warburg O. On the origin of cancer cells. Science 1956;123:309-314.
2. Vander Heiden MG, Cantley LC Thompson CB. Understanding the Warburg effect: the metabolic requirements of cell proliferation. Science 2009;324:1029-1033.
3. Hanahan D, Weinberg RA. Hallmarks of cancer: the next generation. Cell 2011;144:646-674.
4. Estrella V, Chen T, Lloyd M, Wojtkowiak J, Cornnell HH, Ibrahim-Hashim A, Bailey K, Balagurunathan Y, Rothberg JM, Sloane BL, Johnson J, Gatenby RA, Gillies RJ. Acidity

generated by the tumor microenvironment drives local invasion. Cancer Res 2013;73:1524-1535.

5. Chen LQ, Pagel MD. Evaluating pH in the extracellular microenvironment using CEST MRI and other imaging methods. Adv Radiol 2015;206405.
6. Akhenblit PJ, Pagel MD. Recent advances in targeting tumor energy metabolism with tumor acidosis as a biomarker of drug efficacy. J Cancer Sci Ther 2016;8:20-29.
7. Friedl P, Alexander S. Cancer invasion and the microenvironment: Plasticity and reciprocity. Cell 2011;147:992-1009.
8. Plz LH, Strefezzi RF. Proteases as prognostic markers in human and canine cancers. Vet Comp Oncol 2017;15:669-683.
9. Liyange C, Fernando A, Batra J. Differential roles of protease isoforms in the tumor microenvironment. Cancer Met Rev 2019;38:389-415.
10. Buck MR, Carustis DG, Day NA, Honn KV, Sloane BF. Degradation of extracellular-matrix proteins by human cathepsin-B from normal and tumor tissues. Biochemical J 1992;282:273-278.
11. Vidak E, Javorsek U, Vizovisek M, Turk B. Cystine cathepsins and their extracellular roles: Shaping the microenvironment. Cells 2019;8:264.
12. Fonovic M, Turk B. Cystine cathepsins and extracellular matrix degradation. Biochim Biophys Acta – Gen Subj 2014;1840:2560-2570.
13. Sloane BF, Yan SQ, Podgorski I, Linebaugh BE, Cher ML, Mai J, Cavallo-Medved D, Sameni M, Dosescu J, Moin K. Cathepsin B and tumor proteolysis: contribution of the tumor microenvironment. Sem Cancer boil 2005;15:149-157.

14. Jane DT, Morvay L, DaSilva L, Cavallo-Medved D, Sloane BL, Dufresne MJ. Cathepsin B localizes to plasma membrane caveolae of differentiating myoblasts and is secreted in an active form at physiological pH. Boil Chem 2006;387:223-234.
15. Rothberg JM, Baily KM, Wojtkowiak JW, Ben-Nun Y, Bogyo M, Weber E, Moin K, Blum B, Mattingly RR, Gilies RJ, Sloane BF. Acid-mediated tumor proteolysis: contribution of cysteine cathepsins. Neoplasia 2013;15:1125-1137.
16. Ji K, Mayernik L, Moin K, Sloane BF. Acidosis and proteolysis in the tumor microenvironment. Cancer Met Rev 2019;38:103-112.
17. Ward KM, Aletras AH, Balaban RS. A new class of contrast agents for MRI based on proton chemical exchange dependent saturation transfer (CEST). J Magn Reson 2000;143:79-87.
18. Jones KM, Pollard AC, Pagel MD. Clinical applications of chemical exchange saturation transfer (CEST) MRI. J Magn Reson Imaging 2018;47:11-27.
19. Yoo B, Pagel MD. A PARACEST MRI contrast agent to detect enzyme activity. J Am Chem Soc 2006;128:14032-14033.
20. Yoo B, Raam M, Rosenblum R, Pagel MD. Enzyme-responsive PARACEST MRI contrast agents: A new biomedical imaging approach for studies of the proteasome. Contrast Media Mol Imaging 2007;2:189-198.
21. Li Y, Sheth VR, Liu G, Pagel MD. A self-calibrating PARACEST MRI contrast agent that detects esterase enzyme activity. Contrast Media Mol Imaging 2011;6:219-228.
22. Hingorani DV, Randtke EA, Pagel MD. A catalyCEST MRI contrast agent that detects the enzyme- catalyzed creation of a covalent bond. J Am Chem Soc 2013;135:6396–6398.

23. Yoo B, Sheth VR, Howison CM, Douglas MJK, Pineda CT, Maine EA, Baker AF, Pagel MD. Detection of *in vivo* enzyme activity with catalyCEST MRI. Mag Reson Med 2014;71:1221-1230.
24. Hingorani DV, Montano LA, Randtke EA, Lee YS, Cárdenas-Rodríguez J, Pagel MD. A single diamagnetic catalyCEST MRI contrast agent that detects cathepsin B enzyme activity by using a ratio of two CEST signals. Contrast Media Mol Imaging 2016;11:130-138.
25. Sinharay S, Fernández-Cuervo G, Acfalle JP, Pagel MD. Detection of sulfatase enzyme activity with a catalyCEST MRI contrast agent. Chem Euro J 2016;22:6491-6495.
26. Fernández-Cuervo G, Tucker KA, Malm SW, Jones KM, Pagel MD. Diamagnetic imaging agents with a modular chemical design for quantitative detection of β-galactosidase and β-glucuronidase activities with catalyCEST MRI. Bioconjug Chem 2016, 27:2549-2557.
27. Sinharay S, Randtke EA, Jones KM, Howison CM, Chambers SK, Kobayashi H, Pagel MD. Noninvasive detection of enzyme activity in tumor models of human ovarian cancer using catalyCEST MRI. Magn Reson Med 2017;77:2005-2014.
28. Daryaei I, Jones KM, Pagel MD. Detection of DT-diaphorase enzyme with a paraCEST MRI contrast agent. Chem Euro J 2017;23:6514-6517.
29. Sinharay S, Howison CM, Baker AF, Pagel MD. Detecting *in vivo* urokinase Plasminogen Activator activity with a catalyCEST MRI contrast agent. NMR Biomed 2017;30:e3721.
30. Sinharay S, Randtke EA, Howison CM, Ignatenko NA, Pagel MD. Detection of enzyme activity and inhibition during studies in solution, *in vitro* and *in vivo* with catalyCEST MRI. Molec Imaging Biol 2018;20:240-248.
31. Hingorani DV, Yoo B, Bernstein AS, Pagel MD. Detecting enzyme activities with exogenous MRI contrast agents. Chem Euro J 2014;20:9840-9850.

32. Chauvin T, Durand P, Bernier M, Meudal H, Doan BT, Noury F, Badet B, Beloeil JC, Toth E. Detection of enzymatic activity by ParaCEST MRI: A general approach to target a large variety of enzymes. Angew Chem Int Ed 2008;47:4370–4372.
33. Suchy M, Ta R, Li A, Wojciechowski F, Pasternak SH, Bartha R, Hudson RHE. A paramagnetic chemical exchange-based MRI probe metabolized by cathepsin D: design, synthesis and cellular uptake studies. Org Biomol Chem 2010;8:2560 –2566.
34. Airan RD, Bar-Shir A, Liu G, Pelled G, McMahon MT, van Zijl PCM, Bulte JWM, Gilad AA. MRI biosensor for protein kinase A encoded by a single synthetic gene. Magn Reson Med 2012;68:1919–1923.
35. Chauvin T, Torres S, Rosseto R, Kotek J, Badet B, Durand P, Tóth É. Lanthanide (III) Complexes that contain a self-immolative arm: potential enzyme responsive contrast agents for magnetic resonance imaging. Chem Eur J 2012;18:1408–1418.
36. Jamin Y, Eykyn TR, Poon E, Springer C, Robinson SP. Detection of the prodrug-activating enzyme carboxypeptidase G2 activity with chemical exchange saturation transfer magnetic resonance. Molec Imaging Biol 2014;16:152-157.
37. Haris M, Singh A, Mohanmmed I, Ittyerah R, Nath K, Nanga RP, Debrosse C, Kogan F, Cai K, Poptani H, Reddy D, Hariharan H, Reddy R. *In vivo* magnetic resonance imaging of tumor protease activity. Sci Rep 2014;4:6081.
38. Suchy M, Li AX, Lin Y, Feng Q, Bartha R, Hudson RHE. Preliminary evaluation of PARACEST MRI agents for the detection of nitric oxide synthase. Canadian J Chem 2016;94:715-722.

39. Daryaei I, Mohammadebrahim Ghaffari M, Jones KM, Pagel MD. Detection of alkaline phosphatase enzyme activity with a catalyCEST MRI biosensor. ACS Sensors 2016;1:857-861.
40. Fernández-Cuervo G, Sinharay S, Pagel MD. A catalyCEST MRI contrast agent that can simultaneously detect two enzyme activities. ChemBioChem, 2016;17:383-387.
41. Zhang J, Yuan Y, Han Z, Li Y, van Zijl PCM, Yang X, Bulte JWM, Liu G. Detecting acid phosphatase enzymatic activity with phenol as a chemical exchange saturation transfer magnetic resonance imaging contrast agent (PhenolCEST MRI). Biosensors Bioelect 2019;141:111442.
42. Han Z, Li Y, Zhang J, Chen C, vanZijl PCM, Liu G. Molecular imaging of deoxycytidine kinase activity using deoxycytidine-enhanced CEST MRI. Cancer Res 2019;79:2775-2783.
43. Ward KM, Balaban RS. Determination of pH using water protons and chemical exchange dependent saturation transfer (CEST). Magn Reson Med 2000;44:799-802.
44. Aime S, Barge A, Delli Castelli D, Fedeli F, Mortillaro A, Nielsen FU, Terreno E. Paramagnetic lanthanide(III) complexes as pH-sensitive chemical exchange saturation transfer (CEST) contrast agents for MRI applications. Magn Reson Med 2002;47:639–648.
45. Liu G, Li Y, Sheth VR, Pagel MD. Imaging *in vivo* extracellular pH with a single PARACEST MRI contrast agent. Molec Imaging 2012;11:47-57.
46. Longo DL, Dastru W, Digilio G, Keupp J, Langereis S, Lanzardo S, Prestigio S, Steinbach O, Terreno E, Uggeri F, Aime S. Iopamidol as a responsive MRI-chemical exchange saturation transfer contrast agent for pH mapping of kidneys: *In vivo* studies in mice at 7 T. Magn Reson Med 2011;65:202–211.

47. Chen LQ, Howison CM, Jeffery JJ, Robey IF, Kuo PH, Pagel MD. Evaluations of extracellular pH within *in vivo* tumors using acidoCEST MRI. Magn Reson Med 2014;72:1408-1417.
48. Longo DL, Sun PZ, Consolino L, Michelotti FC, Uggeri F, Aime S. A general MRI-CEST ratiometric approach for pH imaging: demonstration of *in vivo* pH mapping with iobitridol. J Am Chem Soc 2014;136:14333-14336.
49. Chen M, Chen C, Shen Z, Zhang S, Zhang X, Chen Y, Lin F, Ma X, Zhuang C, Mao Y, Gan H, Chen P, Zong X, Wu R. Extracellular pH is a biomarker enabling detection of breast cancer and liver cancer using CEST MRI. Oncotarget 2017;8:45759-45767.
50. Wu R, Longo DL, Aime S, Sun PZ. Quantitative description of radiofrquency (RF) power-based ratiometric chemical exchange saturation transfer (CEST) pH imaging. NMR Biomed 2015;28:555-565.
51. Ma YJ, High RA, Tang Q, Wan L, Jerban S, Du J, Change EY. AcidoCEST-UTE MRI for the assessment of extracellular pH of joint tissues at 3 T. Invest Radiol 2019;54:565-571.
52. High RA, Ji Y, Ma YJ, Tang Q, Murphy ME, Du J, Chang EY. *In vivo* assessment of extracellular pH of joint tissues using acidoCEST-UTE MRI. Quant Imaging Med Surg 2019;9:1664-1673.
53. Haftchenary S, Luchman HA, Jouk AO, Veloso AJ, Page BDG, Cheng XR, et al. Potent targeting of the STAT3 protein in brain cancer stem cells: A promising route for treating glioblastoma. ACS Med Chem Lett 2013;4:1102–1107
54. Ralford DS, Fisk CL, Becker ED. Calibration of methanol and ethylene glycol nuclear magnetic resonance thermometers. Anal Chem 1979;51:2050-2051.

55. Shah T, Lu L, Dell K, Pagel MD, Griswold M, Flask CA. CEST-FISP: A novel technique for rapid chemical exchange saturation transfer (CEST) MRI at 7T. Magn Reson Med 2011;65:432–437.

56. Dixon WT, Ren J, Lubag AJ, Ratnakar J, Vinogradov E, Hancu I, Lenkinski RE, Sherry AD. A concentration-independent method to measure exchange rates in PARACEST agents. Magn Reson Med 2010;63:625-632.

57. Ali MM, Liu G, Shah T, Flask CA, Pagel MD. Using two chemical exchange saturation transfer magnetic resonance imaging contrast agents for molecular imaging studies. Acc Chem Res 2009;42:915-924.

58. Liu G, Li Y, Pagel MD. Design and characterization of new irreversible responsive PARACEST MRI contrast agent that detects nitric oxide. Magn Reson Med 2007;58:1249-1256.

59. Aime S, Delli Castelli D, Terreno E. Novel pH-reporter MRI contrast agents. Angewandte Chemie Int Ed 2002;41:4334–4336.

60. Terreno E, Delli Castelli D, Cravotto G, Milone L, Aime S. Ln(III)-DOTAMGly complexes: A versatile series to assess the determinants of the efficacy of paramagnetic chemical exchange saturation transfer agents for magnetic resonance imaging applications. Invest Radiol 2002;39:235-243.

61. Delli Castelli D, Terreno E, Aime S. Yb(III)-HPDO3A: a dual pH- and temperature-responsive CEST agent. Angewandte Chemie Int Ed 2011:50:1798–1800.

62. Sheth VR, Li Y, Chen LQ, Howison CM, Flask CA, Pagel MD. Measuring *in vivo* tumor pHe with CEST-FISP MRI. Magn Reson Med 2012;67:760–768.

63. Sheth VR, Liu G, Li Y, Pagel MD. Improved pH measurements with a single PARACEST MRI contrast agent. Contrast Media Mol Imaging 2012;7:26–34.
64. Longo DL, Busato A, Lanzardo S, Antico F, Aime S. Imaging the pH evolution of an acute kidney injury model by means of iopamidol, a MRI-CEST pH-responsive contrast agent. Magn Reson Med 2013;70:859–864.
65. Sun PZ, Longo DL, Hu W, Xiao G, Wu R. Quantification of iopamidol multi-site chemical exchange properties for ratiometric chemical exchange saturation transfer (CEST) imaging of pH. Phys Med Biol 2014;59:4493–4504.
66. Muller-Lutz A, Khalil N, Schmitt B, Jellus V, Pentang G, Oeltzschner G, Antoch G, Lanzman RS, Wittsack HJ. Pilot study of Iopamidol-based quantitative pH imaging on a clinical 3T MR scanner. MAGMA 2014;27:477–485.
67. Delli Castelli D, Ferrauto G, Cutrin JC, Terreno E, Aime S. *In vivo* maps of extracellular pH in murine melanoma by CEST-MRI. Magn Reson Med 2014;71:326–332.
68. Chen LQ, Howison CM, Spier C, Stopeck AT, Malm SW, Pagel MD, Baker AF. Assessment of carbonic anhydrase IX expression and extracellular pH in B-cell lymphoma cell line models. Leuk Lymphoma 2015;56:1432-1439.
69. Jones KM, Randtke EA, Howison CM, Cárdenas-Rodríguez J, Sime PJ, Kottmann RM, Pagel MD. Measuring extracellular pH in a lung fibrosis model with acidoCEST MRI. Molec Imaging Biol 2015;17:177-184.
70. Chen LQ, Randtke EA, Jones KM, Moon BF, Howison CM, Pagel MD. Evaluations of tumor acidosis within *in vivo* tumor models using parametric maps generated with acidoCEST MRI. Mol Imaging Biol 2015;17:488-496.

71. Bond CJ, Cineus R, Nazarenko AY, Spernyak JA, Morrow JR. Isomeric Co(ii) paraCEST agents as pH responsive MRI probes. Dalt Trans 2020;49:279–84

72. Moon BF, Jones KM, Chen LQ, Liu P, Randtke EA, Howison CM, Pagel MD. A comparison of iopromide and iopamidol, two acidoCEST MRI contrast media that measure tumor extracellular pH. Contrast Media Mol Imaging 2015;10:446-455.

73. Jones KM, Randtke EA, Howison CM, Pagel MD. Respiration gating and Bloch fitting improve pH measurements with acidoCEST MRI in an ovarian orthotopic tumor model. Proc SPIE 2016;9788:978815.

74. Akhenblit PJ, Hanke NT, Gill A, Persky DO, Howison CM, Pagel MD, Baker AF. Assessing metabolic changes in response to mTOR inhibition in a Mantle cell lymphoma xenograft model using acidoCEST MRI. Mol Imaging 2016;15: 1536012116645439.

75. Longo DL, Bartoli A, Consolino L, Bardini P, Arena F, Schwaiger M, Aime S. *In vivo* imaging of tumor metabolism and acidosis by combining PET and MRI-CEST pH imaging. Cancer Res 2016;76:6463–6470.

76. Yang X, Song X, Ray Banerjee S, Li Y, Byun Y, Liu G, Bhujwalla ZM, Pomper MG, McMahon MT. Developing imidazoles as CEST MRI pH sensors. Contrast Media Mol Imaging 2016;11:304–312.

77. Pavuluri K, Manoli I, Pass A, Li Y, Vernon HJ, Venditti CP, McMahon MT. Noninvasive monitoring of chronic kidney disease using pH and perfusion imaging. Sci Adv 2019;5:eaaw8357.

78. Rancan G, Delli Castelli D, Aime S. MRICEST at 1T with large $\mu_{eff}Ln^{3+}$ complexes Tm^{3+}-HPDO3A: An efficient MRI reporter. Magn Reson Med 2016;75:329-336.

79. Krchova T, Galisova A, Jirak D, Hermann P, Kotek J. Ln(III)-complexes of a DOTA analogue with an ethylenediamine pendant arm as pH-responsive PARACEST contrast agents. Dalton Trans 2016;45:3486-3496.

80. Randtke EA, Granados JC, Howison CM, Pagel MD, Cárdenas-Rodríguez J. Multislice CEST MRI improves the spatial assessment of tumor pH. Magn Reson Med 2017;78:97-106.

81. Jones KM, Randtke EA, Yoshimaru E, Howison CM, Chalasani P, Klein RR, Chambers SK, Kuo PH, Pagel MD. Clinical translation of tumor acidosis measurements with acidoCEST MRI. Molec Biol Imaging 2017;19:617-625.

82. Jones KM, Stuehm CA, Hsu CC, Kou PH, Pagel MD, Randke EA. Imaging lung cancer by using chemical exchange saturation transfer MRI with retrospective respiration gating. Tomography 2017;3:201-210.

83. Longo DL, Cutrin JC, Michelotti F, Irrera P, Aime S. Noninvasive evaluation of renal pH homeostasis after ischemia reperfusion injury by CEST-MRI. NMR Biomed 2017;30:e3720

84. Anemone A, Consolino L, Conti L, Reineri F, Cavallo F, Aime S, Longo DL. *In vivo* evaluation of tumour acidosis for assessing the early metabolic response and onset of resistance to dichloroacetate by using magnetic resonance pH imaging. Int J Oncol 2017;51:498–506.

85. Thorarinsdottir AE, Du K, Collins JHP, Harris TD. Ratiometric pH imaging with a Co^{II}_2 MRI probe via CEST effects of opposing pH dependencies. J Am Chem Soc 2017;139:15836-15847.

86. Longo DL, Michelotti F, Consolino L, Bardini P, Digilio G, Xiao G, Sun PZ, Aime S.. In vitro and *in vivo* assessment of nonionic iodinated radiographic molecules as chemical exchange saturation transfer magnetic resonance imaging tumor perfusion agents. Invest Radiol 2016;51:155–162.

87. Lindeman LR, Randtke EA, High RA, Jones KM, Howison CM, Pagel MD. A comparison of exogenous and endogenous CEST MRI methods for evaluating *in vivo* pH. Magn Reson Med 2018;79:2766-2772.

88. Li X, Shepard HM, Cowell JA, Zhao C, Osgood RJ, Rosengren S, Blouw B, Garrovillo SA, Pagel MD, Whatcott CJ, Han H, Von Hoff DD, Labarre MJ, Maneval DC, Thompson CT. Parallel accumulation of tumor hyaluronan, collagen and smooth muscle actin and the adapting tumor microenvironment. Clin Cancer Res 2018;24:4798-4807.

89. Ferrauto G, Di Gregorio E, Auboiroux V, Petit M, Berger F, Aime S. CEST-MRI for glioma pH quantification in mouse model: validation by immunohistochemistry. NMR in Biomed 2018;31:e4005.

90. Som A, Raiya R, Paranandi K, High RA, Reed N, Beeman SC, Brandenburg M, Sudlow G, Prior JL, Akers W, Mah-Som AY, Habimana-Griffin L, Garbow J, Ippolito JE, Pagel MD, Biswas P, Achilefu S. Calcium carbonate nanoparticles stimulate tumor metabolic reprogramming and modulate tumor metastasis. Nanomedicine 2019;14:169-182.

91. Lindeman LR, Jones KM, High RA, Howison CM, Schubitz LF, Pagel MD. Differentiating lung cancer and infection based on measurements of extracellular pH with acidoCEST MRI. Sci Rep 2019;9:13002.

92. Minhas AS, Sharkey J, Randtke EA, Murray P, Wilm B, Pagel MD, Poptani H. Measuring kidney perfusion and renal clearance consecutively using MRI and multispectral optoacoustic tomography. Mol Imaging Biol 2019, *Epub ahead of print*.

93. High RA, Randtke, EA, Jones KM, Lindeman LR, Ma JC, Zhang S, DeRoux LG, Pagel MD. Extracellular acidosis differentiates pancreatitis and pancreatic cancer in mouse models using acidoCEST MRI. Neoplasia 2019;21:1085-1090.

94. Wu Y, Zhou IY, Igarashi T, Longo DL, Aime S, Sun PZ. A generalized ratiometric chemical exchange saturation transfer (CEST) MRI approach for mapping renal pH using iopamidol. Magn Reson Med 2018;79:1553-1558.
95. Arena F, Irrera P, Consolino L, Colombo Serra S, Zaiss M, Longo D L. Flip-angle based ratiometric approach for pulsed CEST-MRI pH imaging. J Magn Reson 2018;287:1–9.

CHAPTER 4

1. Ward KM, Aletras AH, Balaban RS. A new class of contrast agents for MRI based on proton chemical exchange dependent saturation transfer (CEST). J Magn Reson 2000;143:79–87.
2. Kocak G, Tuncer C, Bütün V. pH-Responsive polymers. Polym Chem 2017;8:144–176.
3. Rivlin M, Navon G. Glucosamine and N-acetyl glucosamine as new CEST MRI agents for molecular imaging of tumors. Sci Rep 2016;6:32648.
4. Poreba M, Groborz K, Vizovisek M, Maruggi M, Turk D, Turk B, Powis G, Drag M, Salvesen GS. Fluorescent probes towards selective cathepsin B detection and visualization in cancer cells and patient samples. Chem Sci 2019;10:8461–8477.
5. Mahajan A, Goh V, Basu S, Vaish R, Weeks AJ, Thakur MH, Cook GJ. Bench to bedside molecular functional imaging in translational cancer medicine: to image or to imagine? Clin Radiol 2015;70:1060–1082.
6. Rogosnitzky M, Branch S. Gadolinium-based contrast agent toxicity: a review of known and proposed mechanisms. BioMetals 2016;29:365–376.
7. Garcia J, Liu SZ, Louie AY. Biological effects of MRI contrast agents: gadolinium retention, potential mechanisms and a role for phosphorus. Philos Trans R Soc A Math Phys Eng Sci 2017;375:20170180.

8. Liu G, Banerjee SR, Yang X, Yadav N, Lisok A, Jablonska A, Xu J, Li Y, Pomper MG, van Zijl P. A dextran-based probe for the targeted magnetic resonance imaging of tumors expressing prostate-specific membrane antigen. Nat Biomed Eng 2017;1:977–982.
9. Lesniak WG, Oskolkov N, Song X, Lal B, Yang X, Pomper M, Laterra J, Nimmagadda S, McMahon MT. Salicylic acid conjugated dendrimers are a tunable, high performance CEST MRI nanoplatform. Nano Lett 2016;16:2248–2253.
10. Srinivasarao M, Galliford C V, Low PS. Principles in the design of ligand-targeted cancer therapeutics and imaging agents. Nat Rev Drug Discov 2015;14:203–219.
11. Singh P, Gupta U, Asthana A, Jain NK. Folate and Folate−PEG−PAMAM dendrimers: synthesis, characterization, and targeted anticancer drug delivery potential in tumor bearing mice. Bioconjug Chem 2008;19:2239–2252.
12. Kim H, Shin M, Han S, Kwon W, Hahn SK. Hyaluronic acid derivatives for translational medicines. Biomacromolecules 2019;20:2889–2903.
13. Hingorani DV, Montano LA, Randtke EA, Lee YS, Cárdenas-Rodríguez J, Pagel MD. A single diamagnetic catalyCEST MRI contrast agent that detects cathepsin B enzyme activity by using a ratio of two CEST signals. Contrast Media Mol Imaging 2016;11:130–138.
14. Chen LQ, Howison CM, Jeffery JJ, Robey IF, Kuo PH, Pagel MD. Evaluations of extracellular pH within *in vivo* tumors using acidoCEST MRI. Magn Reson Med 2014;72:1408–1417.
15. Esqueda AC, López JA, Andreu-de-Riquer G, Alvarado-Monzón JC, Ratnakar J, Lubag AJM, Sherry AD, De León-Rodríguez LM. A new gadolinium-based MRI zinc sensor. J Am Chem Soc 2009;131:11387–11391.
16. Do QN, Ratnakar JS, Kovács Z, Sherry AD. redox- and hypoxia-responsive MRI contrast agents. Chem Med Chem 2014;9:1116–1129.

17. Hingorani DV, Bernstein AS, Pagel MD. A review of responsive MRI contrast agents: 2005–2014. Contrast Media Mol Imaging 2015;10:245–265.
18. Lee TW, Kolber MR, Fedorak RN, van Zanten SV. Iron replacement therapy in inflammatory bowel disease patients with iron deficiency anemia: A systematic review and meta-analysis☆. J. Crohn's Colitis 2012;6:267–275.
19. Huang X. Iron overload and its association with cancer risk in humans: evidence for iron as a carcinogenic metal. Mutat Res Mol Mech Mutagen 2003;533:153–171.
20. Rajapurkar MM, Shah S V, Lele SS, Hegde UN, Lensing SY, Gohel K, Mukhopadhyay B, Gang S, Eigenbrodt ML. Association of catalytic iron with cardiovascular disease. Am J Cardiol 2012;109:438–442.
21. Xuan W, Pan R, Wei Y, Cao Y, Li H, Liang F-S, Liu K-J, Wang W. Reaction-based "Off–On" fluorescent probe enabling detection of endogenous labile Fe^{2+} and imaging of Zn^{2+}-induced Fe^{2+} flux in living cells and elevated Fe^{2+} in ischemic stroke. Bioconjug Chem 2016;27:302–308.
22. Liu ML, Chen BB, Li CM, Huang CZ. Carbon dots: synthesis, formation mechanism, fluorescence origin and sensing applications. Green Chem 2019;21:449–471.
23. Zhang J, Yuan Y, Gao M, Han Z, Chu C, Li Y. Carbon dots as a new class of diamagnetic chemical exchange saturation transfer (diaCEST) mri contrast agents. Angew Chem Int Ed 2019;58:9871–9875.
24. Xu X, Zhang K, Zhao L, Li C, Bu W, Shen Y, Gu Z, Chang B, Zheng C, Lin C. Aspirin-based carbon dots, a good biocompatibility of material applied for bioimaging and anti-inflammation. ACS Appl Mater Interfaces 2016;8:32706–32716.

25. Longo DL, Sun PZ, Consolino L, Michelotti FC, Uggeri F, Aime S. A General MRI-CEST ratiometric approach for pH imaging: Demonstration of *in vivo* pH mapping with iobitridol. J Am Chem Soc 2014;136:14333–14336.
26. McGrath NA, Brichacek M, Njardarson JT. A Graphical journey of innovative organic architectures that have improved our lives. J Chem Educ 2010;87:1348–1349.